

UCSF

UC San Francisco Electronic Theses and Dissertations

Title

Systematic Investigation of Host-Pathogen Interactions Identifies Novel Pan-Viral Gene and Drug Targets for Influenza A Viruses and SARS-CoV-2

Permalink

<https://escholarship.org/uc/item/30h6v8mm>

Author

Haas, Kelsey

Publication Date

2022

Supplemental Material

<https://escholarship.org/uc/item/30h6v8mm#supplemental>

Peer reviewed|Thesis/dissertation

Systematic Investigation of Host-Pathogen Interactions Identifies Novel Pan-Viral Gene and Drug Targets for Influenza A Viruses and SARS-CoV-2

by
Kelsey Haas

DISSERTATION

Submitted in partial satisfaction of the requirements for degree of
DOCTOR OF PHILOSOPHY

in

Biochemistry and Molecular Biology

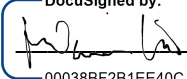
in the

GRADUATE DIVISION

of the

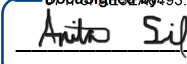
UNIVERSITY OF CALIFORNIA, SAN FRANCISCO

Approved:

DocuSigned by:

00038BF2B1EE40C... Melanie Ott
Chair

DocuSigned by:

Nevan Krogan

DocuSigned by:

9BCB4DFEE8384D2... Anita Sil

Committee Members

Copyright 2022

by

Kelsey Haas

ACKNOWLEDGEMENTS

Thank you to my advisor, Nevan Krogan, for creating opportunities that put me as well as the rest of the lab at the forefront of exciting new ventures and new directions for systems biology. You encouraged me to think outside the box, push the boundaries of what is possible, chase new connections, and question why we can't do all the things (because most of the time we could, and did). I have had incredible experiences and training as a graduate student, and it is because of your unique vision and philosophy for approaching science and structuring your lab.

Thank you to the entire Krogan lab. You are all incredibly talented professionals from diverse specialties. I have valued opportunities to learn from you and work with you. It was a joy to be a part of the dynamic, respectful, hardworking, supportive culture that the lab as a whole has built.

Thank you to my mentors, Robyn Kaake and Judd Hultquist. You have significantly shaped my thinking, my growth and my career as a scientist. You set strong examples of the kind of scientific leaders that I am working to become. To Robyn, thank you for your steadfast mentorship, your pearls of wisdom, and your advice that helped me navigate through many different, sometimes difficult, aspects of science and project management. I am grateful for your patience in teaching me different strategies for doing science (and highlighting the best strategy), and for your encouragement to chase after my ideas. I appreciate your strong advocacy for students and your team, your scientific creativity and your passion for making science accessible to all. Joining you to pursue new avenues of science communication and education outreach are highlights of my graduate experience. To Judd, I was lucky when I first joined the lab to get assigned the bench right next to you, and that you enthusiastically took me on as a student and part of your team. I always appreciated your inclusivity, patience, positivity and input on the many questions I asked you. I am assigned to your old bench now, and when student interns sit at my old bench and ask me the same types of questions I used to ask you, it

makes me smile and makes my heart happy that it comes full circle. Thank you for the time you spent on my training, for sharing your expertise, and for valuing, recognizing and celebrating my (and others') ideas and contributions to your team.

Thank you to Michael McGregor. I am fortunate that you included me as part of your and Judd's team when I first joined the lab. I have enjoyed and benefited from working with you and learning from you. Thank you for sharing your expertise, and for the care you put into helping those around you (including me). You are a gem of a scientist, colleague, and friend, more than you give yourself credit for. Thank you for believing in me, recognizing and valuing my input and ideas, being a sounding board for me as I navigated the PhD, and fostering a safe space for discussion about science and life. I am grateful for your collegiality, camaraderie and friendship.

Thank you to Manon Eckhardt for advocating for me and for your advice that helped steer me through the last (and hardest) stretch of graduate school. Thank you to Lorena Zuliani-Alvarez for sharing your expertise and feedback to elevate the science in our story. Thank you to Mehdi Bouhaddou for your encouragement, support and thoughtfulness in teaching students (including me). Thank you to Danielle Swaney. I admire your ability to pack maximal punch into minimal, concise wording, and I appreciate your perspective, advice and advocacy. Thank you also for mentoring me when I was an undergraduate student at University of Washington and you were a postdoc, and for training me in the field of proteomics. It shaped my path towards graduate school. Thank you to Ernst Pulido, Maya Modak, Manisha Ummadi, Ajda Rojc, Monita Muralidharan and Zeynep Cakir. You are all wonderful, supportive, empathetic and talented teammates and friends. I have appreciated our chats, game nights and fun dinners exploring new spots in the city. Thank you to the students I had the privilege of mentoring, Heba Morsy and Phoebe Lawwill, for your curiosity, excitement and energy. It was a joy to work with you, teach you, watch you succeed and see you develop a spark and connection with science.

Thank you to the Krogan lab graduate students: Joe Hiatt, Snow Naing, Reuben Hogan and Paige Haas, who are talented scientists, great friends and an incredibly supportive community. I value our candid discussions, peer mentorship, mutual respect and encouragement.

Thank you to the UCSF and J. David Gladstone community that shaped my graduate experience. Thank you to my thesis committee, Melanie Ott and Anita Sil, for your advice, perspectives and advocacy as I completed this degree. You helped shape my scientific growth and my personal growth as a leader. Thank you to Toni Hurley and the Tetrad faculty advisors of the Graduate Curriculum Committee (GCC) for your student advocacy. Your advice when the road took uncertain twists and turns helped me come up with a plan forward.

Thank you to Krystal Fontaine, and all the members of J. David Gladstone's BioFulcrum team. I am immensely grateful for the collaborative experience bridging the gap between academia and industry. It was formative for my future career path. Krystal, you are a kind, generous, brilliant and thoughtful scientist, leader and mentor. You look out for those around you, and I am thankful for our discussions, your advocacy for me and my future career, and your mentorship. I look up to you for the example of a scientific leader you set, and work towards that example.

To the Tetrad Class of 2014, I am so grateful to know each and every one of you, and to have had the chance to do this PhD with you. You are all accomplished scientists, compassionate humans and wonderful friends. You inspire me. Special thanks to Ben Barsi-Rhyne and Karen Cheng (the original roomies) for your friendship, coffee talks and peer mentorship. Our home life brought peace, a supportive space to process and decompress together, and fun neighborhood explorations finding new restaurants and catching Pokémon. To Nairi Hartooni, Valentina Garcia and Allison Cohen (the brain trust), thank you for your friendship, walk & talks and peer mentorship. Our friendship brought joy, a safe space to navigate tough road blocks, memorable

Bay Area hiking adventures and next-level picnics. To each member of the Tetrad 2014 cohort, I am honored to be your peer as we move into the next chapter of our careers.

To the *Biologists Being Basic (B3)* team, thank you for fostering a fun, creative outlet. I immensely enjoyed adventuring into the podcast realm with you all, and practicing scientific communication with accomplished labmates and friends. To Gina Nguyen and Alexa Rocourt, thank you for sharing your artistic and media expertise that elevated each episode.

Thank you to the NIH NIAID U19 FluOMICS team for your collegiality and collaboration on many projects throughout my dissertation. Thank you to Leah Shriver for your advice and camaraderie while we stuck through these datasets and pushed them to the finish line. Thank you to Eun-Young Kim for looking out for me, and for your support on the dissertation. Thank you to Megan Shaw and Adolfo García-Sastre, who provided space and training support through the Embed program for me to work at Mount Sinai for a one-month immersive research experience centered on learning IAV virology. It was a unique part of my graduate training that I treasure.

Thank you to my undergraduate advisor, Judit Villén, for your mentorship and fostering the spark for proteomics that drives my career path. Your determination in advocating for what is fair for your students in collaborations and publishing stays with me today. You encouraged me to apply to graduate school at UCSF (I thought I would not get in) because you thought I would enjoy working in the Krogan lab. Without your guidance, I would not be here.

To my community outside of UCSF and Gladstone, endless thank yous for your support during this journey. To Emily Seubert, thank you for your humor and silliness, life chats and lifelong friendship. Thank you to the Seubert family (Alex Marquez, Nina Kooroshfar, John Seubert, Sara Seubert and Ron Seubert) for your continuous support. To Martha Watson, thank you for

your optimism, positivity and encouragement, and for our Bay Area adventures that brought balance to graduate school. To Laura Gladson and Katie Walton, thank you for your support, strength, life chats and lifelong friendships. Laura, I am rooting for you as you work towards completing your PhD, just as you did for me. To Allison Hall, thank you for your fierceness, your advocacy, your never-ending encouragement and all of our San Francisco adventures. To Sean Minor, who held down the fort especially as Paige and I finished our PhDs, you are a brother to me. Thank you for your grounding perspective and encouragement, always being down for a board game, and an endless supply of clever puns and random Reddit facts.

To my parents, Ann and Randy Haas, thank you for being a strong guiding force in this world, for providing a safe harbor through storms and for always supporting me. Thank you to my grandmothers, Rita Dunn and Dolores Haas, for being strong role models. Thank you to my extended Cerny, Wielochowski, Haas and Martin families for rooting for me to get this PhD, and for tuning in to my remote dissertation talk to join the pandemic-mindful celebration.

Thank you to my sister, Paige Haas. It has been so special to navigate through this chapter with you, as we worked alongside each other in the Krogan lab, pursued our PhDs at UCSF together, lived together and adventured around San Francisco and California's national parks together. Thank you for grounding me through the tough times in graduate school, providing a safe space to process my thoughts, and gently reminding me not to be so hard on myself. In your dissertation acknowledgements, you said I helped you see what you are capable of. You helped me see what I am capable of as well. Love you forever, my sister chromatid.

In closing out the many thank yous, I would like to emphasize that each person I have met along my scientific journey has enriched my life and scientific career, and I am all the better because of it. Here's to the new, future chapters to come.

CONTRIBUTIONS

This dissertation presents work from a highly collaborative research endeavor between members of the National Institutes of Health (NIH) National Institute of Allergy and Infectious Diseases (NIAID) U19 FluOMICS and UCSF Quantitative Biosciences Institute (QBI) Coronavirus Research Group (QCRG). Contributing individuals include members of the Krogan lab (UCSF, QBI, J. David Gladstone Institutes), the García-Sastre lab (Icahn School of Medicine at Mount Sinai), the Wolinsky lab (Northwestern University), the Shaw lab (University of the Western Cape), the Chanda lab (Sanford Burnham Prebys), the Shoichet lab (UCSF), the Shokat lab (UCSF), the Vignuzzi lab (Institut Pasteur), and the Basler lab (Georgia State University, Icahn School of Medicine at Mount Sinai).

The content in this dissertation is reformatted from a manuscript in preparation:

Kelsey M. Haas, Michael J. McGregor, Mehdi Bouhaddou, Benjamin J. Polacco, Tom Nguyen, Billy Newton, Matthew Urbanowski, Eun-Young Kim, Heejin Kim, Michael Williams, Veronica V. Rezelj, Alexandra Hardy, Erica Stevenson, Ellie Walker, Tiffany Kim, Sudhir Penugonda, Hannes Braberg, Yuan Zhou, Bhavya Harjai, Tia A. Tummino, James E. Melnyk, Margaret Soucheray, Jyoti Batra, Lars Pache, Laura Martin-Sancho, Jared Carlson-Stevermer, Alexander S. Jureka, Christopher F. Basler, Kevan M. Shokat, Brian K. Shoichet, Jeffrey R. Johnson, Megan Shaw, Lorena Zuliani-Alvarez, Sumit Chanda, Marco Vignuzzi, Danielle L. Swaney, Manon Eckhardt, Steven M. Wolinsky, Kris M. White, Judd F. Hultquist*, Robyn M. Kaake*, Adolfo García-Sastre*, Nevan J. Krogan*. Systematic Proteomic Analyses of Influenza A Viruses Identify Pan-Viral Targets. 2022. *Manuscript in preparation.*

*co-corresponding authors

Kelsey M. Haas is supported by the National Science Foundation Graduate Research Fellowship Program (1650113).

Chapter 2 presents work conducted in the Krogan lab by Kelsey M. Haas, Michael J. McGregor, Judd F. Hultquist, Robyn M. Kaake and Danielle L. Swaney (data collection, data analysis, data visualization); Tom Nguyen, Bhavya Harjai, Mehdi Bouhaddou, Manon Eckhardt and Yuan Zhou (data analysis, data visualization). Figures were generated by Kelsey M. Haas, Judd F. Hultquist, Michael J. McGregor and Manon Eckhardt. Dataset repositories were managed by Lars Pache and Sumit Chanda. Text was written by Kelsey M. Haas, with edits by Robyn M. Kaake, Manon Eckhardt and Lorena Zuliani-Alvarez. Tables were generated by Kelsey M. Haas using data analysis from contributing members.

Chapter 3 presents work conducted in the García-Sastre, Shaw and Krogan labs. Contributing members include: Adolfo García-Sastre, Megan Shaw, Matthew Urbanowski, Billy Newton, Erica Stevenson and Jeffrey R. Johnson (data collection); Tom Nguyen, Danielle L. Swaney, Benjamin J. Polacco, Mehdi Bouhaddou, Judd F. Hultquist, Robyn M. Kaake, Manon Eckhardt and Kelsey M. Haas (data analysis, data visualization). Dataset repositories were managed by Lars Pache and Sumit Chanda. Figures were generated by Kelsey M. Haas, Mehdi Bouhaddou, Manon Eckhardt and Robyn M. Kaake. Text was written by Kelsey M. Haas, with edits by Robyn M. Kaake, Manon Eckhardt and Lorena Zuliani-Alvarez. Tables were generated by Kelsey M. Haas using data analysis from contributing members.

Chapter 4 presents work conducted in the Wolinsky lab by Eun-Young Kim, Heejin Kim, Ellie Walker, Tiffany Kim and Sudhir Penugonda (data collection, data analysis, data visualization), and in the Krogan lab by Mehdi Bouhaddou (data analysis, data visualization). This chapter also presents patient data collected by the eMERGE group at five eMERGE study sites (Cincinnati Children's Hospital Medical Center, Marshfield, Mount Sinai, Northwestern University and Vanderbilt) and at the St. Jude Children's Hospital. Figures were generated by Kelsey M. Haas, with edits by Robyn M. Kaake and Eun-Young Kim. Text was written by Kelsey M. Haas

and Eun-Young Kim, with edits by Mehdi Bouhaddou, Robyn M. Kaake and Lorena Zuliani-Alvarez. Tables were generated by Kelsey M. Haas and Eun-Young Kim using data analysis from contributing members.

Chapter 5 presents work conducted in the Krogan lab by Kelsey M. Haas (data collection, data analysis, data visualization) and Hannes Braberg (data analysis), and in the Vignuzzi lab by Veronica V. Rezelj and Alexandra Hardy (data collection). Additional investigatory work was performed by Laura Martin-Sancho, Jared Carlson-Stevermer, Alexander S. Jureka and Christopher F. Basler (data not included or shown). Figures were generated by Kelsey M. Haas. Text was written by Kelsey M. Haas, with edits by Robyn M. Kaake, Manon Eckhardt and Lorena Zuliani-Alvarez. Tables were generated by Kelsey M. Haas using data analysis from contributing members.

Chapter 6 presents work conducted in the García-Sastre lab by Kris M. White and Michael Williams (data collection, data analysis) and in the Krogan lab by Kelsey M. Haas (data visualization). Advice and reagents for data collection were provided by Tia A. Tummino, Brian K. Shoichet, James E. Melnyk and Kevan M. Shokat. Figures were generated by Kelsey M. Haas. Text was written by Kelsey M. Haas, with edits by Robyn M. Kaake, Manon Eckhardt, Lorena Zuliani-Alvarez, Michael Williams and Kris M. White. Tables were generated by Kelsey M. Haas using data analysis from contributing members.

Systematic Investigation of Host-Pathogen Interactions Identifies Novel Pan-Viral Gene and Drug Targets for Influenza A Viruses and SARS-CoV-2

Kelsey Haas

ABSTRACT

Influenza A Virus (IAV) is a recurring infectious respiratory virus that causes seasonal infections and global pandemics. With increasing antiviral drug resistance and limited yearly vaccine efficacy, there is a need for new therapeutic treatments. Host-directed therapies offer an alternative treatment strategy, however development of these therapies requires identifying host proteins and signaling pathways that are targeted and rewired by IAV and that are essential for infection. Here, we employed quantitative proteomics, functional genomics and pharmacological screening to systematically identify host factors for three clinical IAV strains (pH1N1, H3N2, H5N1) in three cell types relevant to infection (A549, NHBE, THP-1). We identified 332 IAV-human protein-protein interactions (PPIs) between 214 human proteins and 12 IAV proteins, and 13 IAV-modulated kinase pathways including PRKDC and MAPK signaling. Exome sequencing data of patients with benign or severe influenza disease revealed that predicted loss-of-function genes associated with severe influenza disease are significantly changing in protein abundance (15 proteins) and phosphorylation status (25 proteins and 54 phosphorylation sites) during IAV infection, and include variants mapping back to five PPI factors. This analysis highlighted interferon alpha/beta signaling and TLR signaling as potential molecular drivers of disease severity. Functional genomic screening of our identified PPI and signaling targets uncovered 54 human genes that regulate IAV infection. Given that IAV co-circulates seasonally with severe acute respiratory coronavirus 2 (SARS-CoV-2), the causative agent of the COVID-19 pandemic, we screened these 54 genes against SARS-CoV-2 infection and identified two human genes (COPB1, AHNAK) that act as pro-viral factors for both IAV and SARS-CoV-2 infection. To discover pan-IAV and pan-respiratory virus host-directed therapies,

we screened a total of 37 pre-clinical or FDA-approved compounds against pH1N1, H3N2 and H5N1 IAV infection. 16 compounds suppressed replication of at least one IAV strain, with seven compounds showing pan-IAV antiviral activity. Five compounds (Dinaciclib, MAPK13-IN-1, Gilteritinib, Pictilisib, MK-2206) targeting five kinase pathways (CDK2, MAPK13 (p38 δ), FLT3/AXL, PI3KCA/PI3KCD, pan-AKT) showed antiviral activity against infection by multiple strains of IAV and SARS-CoV-2. These represent putative targets for pan-respiratory virus host-directed therapies.

TABLE OF CONTENTS

Chapter 1: Introduction	1
Chapter 2: Generating a Multi-Dimensional IAV-Human Interactome	9
AP-MS Identifies pH1N1, H3N2, and H5N1 IAV-Human PPIs.....	10
IAV PPI Networks from Three Cell Types Identify Strain-Specific and Pan-IAV- Human Interactions.....	14
Methods.....	18
Chapter 3: Global Proteomic Profiling Highlights Modulated Kinases in IAV Infection	39
Methods.....	44
Chapter 4: Patient Exome Sequencing Identifies Gene Variants Encoding Proteins that are Regulated in Abundance and Phosphorylation during IAV Infection	56
Methods.....	61
Chapter 5: siRNA Knockdown Identifies Pro-viral and Antiviral Factors of IAV and SARS-CoV-2 Infection	68
Methods.....	73
Chapter 6: Host-Directed Compounds Targeting IAV and SARS-CoV-2 Factors Identify Inhibitors of pH1N1, H3N2 and H5N1 IAV Infection	82
Methods.....	87
Chapter 7: Discussion	94
References	107

LIST OF FIGURES

Figure 1.1 A systems biology platform functionally characterizes pan-IAV-human protein interactions and signaling networks.....	8
Figure 2.1 AP-MS identifies pH1N1, H3N2 and H5N1 IAV-human PPIs.....	29
Figure 2.2 IAV PPI networks from three cell types identify strain-specific and pan-IAV-human interactions.....	31
Figure S2.1 Summary of IAV AP-MS data, Related to Figure 2.1.....	32
Figure S2.2 IAV protein expression, Related to Figures 2.1 and 2.2.....	34
Figure S2.3 PPI networks specific to each cell type, Related to Figure 2.2.....	36
Figure 3.1 Global proteomic profiling highlights modulated kinases in IAV infection.....	52
Figure S3.1 Strain-specific and shared phosphorylation sites, phosphorylation GO enrichments and AB and PH dataset correlation, Related to Figure 3.1.....	54
Figure 4.1 Patient exome sequencing identifies gene variants encoding proteins that are regulated in abundance and phosphorylation during IAV infection.....	65
Figure 5.1 siRNA knockdown identifies pro-viral and antiviral factors of IAV infection.....	78
Figure S5.1 Probing IAV targets against SARS-CoV-2 infection identifies factors that regulate both IAV and SARS-CoV-2, Related to Figure 5.1.....	80
Figure 6.1 Host-directed compounds targeting IAV and SARS-CoV-2 factors identify inhibitors of pH1N1, H3N2 and H5N1 IAV infection.....	89
Figure S6.1 Host-directed compound dose-response curves for pH1N1, H3N2 and H5N1 IAV and cell viability, Related to Figure 6.1.....	91

LIST OF TABLES

Table S2.1 AP-MS IAV protein sequences, scored IAV-human PPIs and PPI enrichments, Related to Figures 2.1, 2.2, S2.1, S2.2 and S2.3.....	38
Table S2.2 PPI liquid chromatography (LC) and mass spectrometry (MS) acquisition parameters, Related to Methods.....	38
Table S3.1 Global protein abundance and phosphorylation data, phosphorylation GO enrichments and predicted kinase activities, Related to Figures 3.1 and S3.1.....	55
Table S3.2 AB and PH liquid chromatography (LC) and mass spectrometry (MS) acquisition parameters, Related to Methods.....	55
Table S4.1 Identification of rare gene variants in patients with severe influenza disease and permutation tests with global proteomic profiling data, Related to Figure 4.1.....	67
Table S5.1 siRNA targets and log ₂ FC against IAV and SARS-CoV-2 infection, Related to Figures 5.1 and S5.1.....	81
Table S6.1 Compound screening against IAV infection, Related to Figures 6.1 and S6.1.....	93

LIST OF ABBREVIATIONS

A549	Adenocarcinomic human alveolar basal epithelial cells
AB	Global protein abundance
AP-MS	Affinity purification-mass spectrometry
CC10	Concentration at which fit hill function crosses 10% for cell viability
CC50	Concentration at which fit hill function crosses 50% for cell viability
cm	Centimeter
COVID-19	Coronavirus disease 2019
dsRNA	Double-stranded RNA
g	Gram
GFP	Green fluorescent protein
GO	Gene ontology
H3N2	Influenza A virus strain A/Wyoming/03/2003(H3N2)
H5N1	Influenza A virus strain A/Vietnam/1203/2004(H5N1)
HA	Hemagglutinin
HDT	Host-directed therapy
IAV	Influenza A virus
IC50	Concentration at which fit hill function crosses 50% for viral inhibition
IC90	Concentration at which fit hill function crosses 90% for viral inhibition
LC	Liquid chromatography
LC-MS/MS	Liquid chromatography tandem mass spectrometry
M	Molar
M1	Matrix protein 1
M2	Matrix protein 2
MF	Molecular function
MiST	Mass spectrometry interaction statistics

mL	Milliliter
mM	Millimolar
MS	Mass spectrometry
N40	PB1 alternate translation protein
NA	Neuraminidase
NEP	Nuclear export protein
ng	Nanogram
NHBE	Primary normal human bronchial epithelial cells
nM	Nanomolar
NP	Nucleoprotein
NS1	Non-structural protein 1
PA	Polymerase acidic protein
PA-X	PA frameshift protein
PB1	Polymerase basic protein 1
PB1-F2	PB1 frameshift protein
PB2	Polymerase basic protein 2
PH	Global protein phosphorylation
pH1N1	Influenza A virus strain A/California/04/2009(H1N1)
pLOF	Predicted loss of function
PMA	Phorbol-12-myristate-13-acetate
PPIs	Protein-protein interactions
RNA	Ribonucleic acid
rpm	Revolutions per minute
SARS-CoV	Severe acute respiratory syndrome coronavirus
SARS-CoV-2	Severe acute respiratory syndrome coronavirus 2
siRNA	Small interfering RNA

THP-1	Acute monocytic leukemic human monocyte cells
vRNA	Viral RNA
vRNP	Viral ribonucleoprotein

LIST OF SYMBOLS

°C	Degrees Celsius
μg	Microgram
μL	Microliter
μm	Micrometer
x g	Times gravity (centrifugal force)

CHAPTER 1

Introduction

Influenza A Virus (IAV) is an enveloped, negative-sense single-stranded RNA virus that causes mild to severe respiratory disease colloquially called “the flu”. While mild to moderate symptoms of IAV infection commonly include cough, runny nose, fatigue and fever, severe disease can result in hospitalization and death. IAV circulates as yearly seasonal infections, and is one of a number of pathogens with pandemic potential. Notable past flu pandemics include the 1918 Spanish flu pandemic and the 2009 swine flu pandemic. These pandemic IAV strains infected on average >10% of the world population during circulation and resulted in mortality rates ranging 0.01% - 3% (Dawood et al., 2012; Johnson and Mueller, 2002; Kelly et al., 2011; Taubenberger and Morens, 2006). While generally associated with lower mortality rates, seasonal IAV strains still substantially impact the economy and public health. In the U.S., the economic burden from seasonal IAV is estimated at an average annual total of \$11.2 billion (Putri et al., 2018), with 3-11% of the U.S. population experiencing flu symptoms each season depending on the circulating strains (Tokars et al., 2018). The annual burden and potential for future global pandemics highlight a continued need for developing new therapeutics that are effective against multiple IAV strains.

IAV strains are subtyped based on two surface proteins embedded in the virus envelope that are also the primary antigens for immune recognition: hemagglutinin (HA) and neuraminidase (NA). Currently, 18 different HA subtypes (H1-H18) and 11 different NA subtypes (N1-N11) have been characterized, leading to diverse subtype combinations (Centers for Disease Control and Prevention, National Center for Immunization and Respiratory Diseases (NCIRD), 2021a). This diversity can be explained in part by antigenic drift due to IAV’s high basal mutation rate that leads to small genetic changes, and antigenic shift that leads to major genetic changes (Taubenberger and Kash, 2010). Antigenic shift is facilitated by IAV’s segmented genome that allows for the swapping of whole gene segments during co-infection, and IAV’s ability to infect multiple host reservoirs including humans, birds, waterfowl and pigs (Medina and García-Sastre,

2011; Taubenberger and Kash, 2010). Due to antigenic drift and shift and zoonotic transmission, distinct strains of IAV novel to the human population regularly emerge that have altered transmissibility, pathogenicity and pandemic potential (Medina and García-Sastre, 2011).

Given the genetic diversity of IAV, we focused our study on three different clinical IAV isolates that directly impact human health: Influenza A/California/04/2009 H1N1 (pH1N1); Influenza A/Wyoming/03/2003 H3N2 (H3N2); and Influenza A/Vietnam/1203/2004 H5N1 (H5N1). pH1N1 is a pandemic swine-origin strain that is the causative agent of the 2009 swine flu pandemic. Although pH1N1 is highly transmissible, it has a low mortality rate. In the first year of pH1N1 circulation, it is estimated that 11-21% of the world's population was infected (Kelly et al., 2011) and over 200,000 deaths resulted world-wide (Dawood et al., 2012). H3N2 is a seasonal-circulating, human-adapted strain from the 2003-2004 flu season that caused increased disease severity and has average transmissibility and mortality compared to previous flu seasons (Centers for Disease Control and Prevention (CDC), 2004). Together, pH1N1 and H3N2 subtypes are the predominant IAV strains that circulate each flu season and cause hundreds of thousands of yearly infections, illnesses, hospitalizations and deaths. pH1N1 and H3N2 subtypes are also targeted each year by vaccine. In comparison, H5N1 is an avian strain that predominantly infects poultry and infrequently infects humans (Tiensin et al., 2005). The largest known H5N1 outbreak in humans occurred during the 2003-2004 flu season among individuals with prolonged direct contact with infected birds (Webster et al., 2005). While human-to-human transmission of H5N1 is rare, H5N1 infection is associated with severe respiratory disease and a >50% mortality rate (Webster et al., 2005). Previous studies showed a handful of mutations in H5N1 impart airborne transmissibility in ferrets (Herfst et al., 2012; Imai et al., 2012), suggesting H5N1 could mutate to gain transmissibility between mammals and represent a future risk for pandemic influenza among humans. Accordingly, H5N1 is considered a potential pandemic

strain by the World Health Organization (WHO) global influenza pandemic preparedness plan. Collectively, these three IAV strains represent diverse virological properties of IAV, including different subtypes (i.e. H1N1, H3N2, and H5N1), recurrence (i.e. pandemic and seasonal), origin species (i.e. swine and avian), transmissibility and pathogenicity.

The inherent genetic diversity in IAV also poses significant challenges to preventative care and antiviral treatments. Vaccines are developed and administered each year, but have limited and variable effectiveness (Centers for Disease Control and Prevention, National Center for Immunization and Respiratory Diseases (NCIRD), 2021b). Currently, there are three classes of approved antiviral therapeutics that target three IAV proteins: NA, ion channel matrix protein M2 and polymerase subunit PA. However, increasing levels of drug resistant viral populations limit their efficacy, restricting use of M2-targeting and NA-targeting drug classes in antiviral treatment (Hussain et al., 2017). This is particularly observed for 2009 pH1N1 and pH1N1-like seasonal strains (Hussain et al., 2017). Recently developed PA-targeting drugs offer promising efficacy as next-generation antiviral treatments, however resistant viral populations are emerging and continued surveillance for changes in drug susceptibility will be required to determine long-term effectiveness (Goldhill et al., 2018; Gubareva et al., 2019; Omoto et al., 2018; Takashita et al., 2019). Host-directed therapies (HDT) offer an alternative approach by targeting host factors essential to virus replication rather than directly engaging viral-encoded factors. Thus, HDT largely side-steps the challenge of developed drug resistance and has the potential for pan-viral efficacy, as many diverse viruses utilize the same host pathways (Kaufmann et al., 2018; Kumar et al., 2020; Zumla et al., 2016). Proteomic approaches that identify virus-host protein-protein interactions (PPIs) and virus-induced changes in host signaling pathways can pinpoint key protein linchpins essential to virus propagation (Batra et al., 2018; Bouhaddou et al., 2020; Diep et al., 2019; Eckhardt et al., 2020; Gordon et al., 2020a, 2020b; Heaton et al., 2016; Li et al., 2019; Lin et al., 2013; Lum and Cristea, 2016; Ramage et al., 2015; Shah et al., 2018; Simon et

al., 2015; Tripathi et al., 2015; Wang et al., 2017; Watanabe et al., 2014). Global IAV-human PPI networks previously generated with lab-adapted IAV strains in immortalized cell lines and in yeast offer good foundations for identifying essential linchpins for IAV infection (Heaton et al., 2016; Shapira et al., 2009; Tripathi et al., 2015; Wang et al., 2017; Watanabe et al., 2014), however, the overlap between these studies is limited, and most studies do not use physiological target cell types of IAV infection. In addition, combining proteomic approaches with other systems approaches such as functional genomics and chemoinformatics can yield actionable HDT targets (Eckhardt et al., 2020; Law et al., 2013). We and others have demonstrated the utility of a cross-discipline integrative approach for generating comprehensive models of host reprogramming by a variety of other viral pathogens, and have used these models to identify promising drug candidates (Batra et al., 2018; Bojkova et al., 2020; Bouhaddou et al., 2020; Diep et al., 2019; Gordon et al., 2020a, 2020b; Hekman et al., 2020).

IAV co-circulates with other respiratory viruses, including severe acute respiratory coronavirus 2 (SARS-CoV-2), the causative agent of the COVID-19 pandemic. At the time of this report, the COVID-19 pandemic continues to be a global human health emergency. Global vaccination against SARS-CoV-2 is lagging in a majority of countries, notably in but not exclusive to those that have fewer resources and infrastructure to obtain and deliver vaccines (Commissioners of the Lancet COVID-19 Commission., 2021; Mathieu et al., 2021). In addition, an increasing number of more pathogenic and transmissible SARS-CoV-2 variants of concern are becoming dominant and continue to surge (Cele et al., 2021; Davies et al., 2021; Mlcochova et al., 2021; Resende et al., 2021; Tegally et al., 2021). It is predicted that SARS-CoV-2 will be endemic, similar to IAV (Phillips, 2021). Yearly co-circulation of IAV with SARS-CoV-2 may present significant future healthcare challenges, as IAV and SARS-CoV-2 present similar respiratory disease symptoms. Currently, infection by either virus is treated separately by pharmacological or antibody-based antiviral therapeutics approved for clinical use against either SARS-CoV-2 or

IAV. Identifying and targeting human proteins essential for infection by both viruses could provide pan-respiratory virus host-directed treatments.

Here, we employed a first-in-class integrative systems biology approach to identify human proteins essential for replication by two respiratory viruses: IAV and SARS-CoV-2 (**Figure 1.1**). We leveraged two orthogonal proteomics approaches, affinity purification-mass spectrometry (AP-MS) (**Chapter 2**) and global protein abundance and phosphorylation profiling (**Chapter 3**), to catalog IAV-human protein-protein interaction and signaling networks. We systematically identified 214 IAV-human PPIs of three clinical IAV strains in three cell types that represent primary and secondary targets of infection (**Chapter 2**). We also profiled 13 human kinases that are predicted to be modulated in activity during IAV infection (**Chapter 3**). Exome sequencing data of IAV-infected patients identified a number of gene variants in TRIF(TICAM1)-mediated TLR4, interferon alpha/beta, and ERK/MAPK signaling associated with severe influenza disease (**Chapter 4**). The intersection between severe influenza disease gene variants and our proteomics data revealed five PPIs with predicted loss-of-function variants correlated with severe influenza disease, and identified a statistically enriched set of host proteins that are downregulated in protein abundance and differentially regulated by phosphorylation during IAV infection. The combination of patient data with *ex vivo* proteomic data provided insight into potential genetic and molecular drivers of influenza disease severity. In addition, we performed functional genomic screening of the host targets identified in our proteomic data and identified 54 human genes that regulate IAV infection in A549 cells (**Chapter 5**). These functionally important host factors were then tested against SARS-CoV-2 infection to identify human proteins that can disrupt infection by both respiratory viruses. We found two human genes, ANAHK and COPB1, that were essential for infection by both IAV and SARS-CoV-2. Lastly, we endeavored to identify host-directed therapies that could be repurposed for treatment against IAV and SARS-CoV-2 (**Chapter 6**). We identified unique compounds that target IAV proteomic

nodes and leveraged previously published SARS-CoV-2 phosphorylation data (Bouhaddou et al., 2020) to identify drugs with potential dual activity against both respiratory viruses. In total, 37 unique compounds were screened against pH1N1, H3N2 and H5N1 IAV. Sixteen compounds suppressed replication of at least one strain of IAV, with seven compounds suppressing replication of all three strains. Five of these compounds show antiviral activity against multiple strains of IAV and SARS-CoV-2. Collectively, these represent potential gene targets and compounds for pan-respiratory virus HDT.

FIGURE AND LEGEND

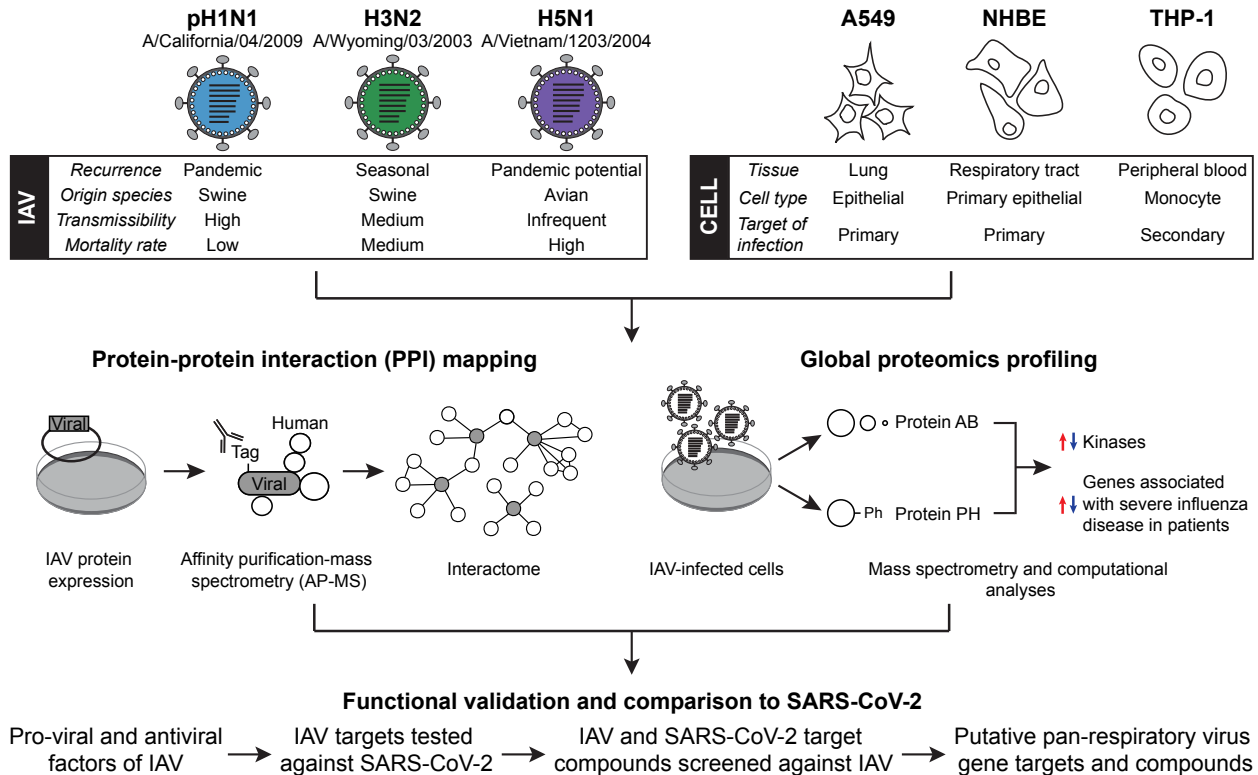


Figure 1.1 A systems biology platform functionally characterizes pan-IAV-human protein interactions and signaling networks. Using three clinical IAV strains with differing recurrence, origin species, transmissibility and mortality rate, and three human cell types from different tissues targeted during IAV infection, we employed a two-pronged global proteomics approach to characterize IAV-human interactions. First, in protein-protein interaction (PPI) mapping, affinity-tagged IAV proteins were expressed in human cells and subjected to affinity purification-mass spectrometry (AP-MS) to generate an IAV-human interactome. Second, in global proteomics profiling, changes in global protein abundance (AB) and phosphorylation (PH) were quantified by mass spectrometry. Computational analyses identified human kinases with predicted increased or decreased activity during IAV infection. Exome sequencing data of patients with benign or severe influenza disease revealed predicted loss-of-function genes associated with severe influenza disease that significantly change in PPI, AB and PH data as potential molecular drivers of disease severity. Human proteins from PPI and PH approaches were functionally validated by siRNA knockdown to identify pro-viral and antiviral factors of IAV infection. These factors were then tested against SARS-CoV-2 infection to identify genes that regulate both IAV and SARS-CoV-2. Finally, pre-clinical, clinical and FDA-approved compounds were selected to target functional IAV PPI and PH factors, and screened against IAV infection. We also mined orthologous SARS-CoV-2 PH data to identify compounds that have antiviral activity against SARS-CoV-2 (Bouhaddou et al., 2020) and target pathways identified in IAV PH data (this study). These compounds were screened against IAV infection. Gene knockdowns and compounds that suppress both IAV and SARS-CoV-2 infection represent putative pan-respiratory virus gene targets and compounds.

CHAPTER 2

Generating a Multi-Dimensional IAV-Human Interactome

AP-MS Identifies pH1N1, H3N2, and H5N1 IAV-Human PPIs

We employed a two-pronged, unbiased, proteomics-based systems biology approach to characterize pan-IAV-human PPIs and identify putative targets for functional genetic and pharmacological testing (**Figure 1.1**). First, we mapped PPI networks for pH1N1, H3N2 and H5N1, whereby affinity-tagged IAV proteins were expressed in human cells and subjected to unbiased affinity purification-mass spectrometry (AP-MS) to generate a high-confidence IAV-human interactome. It is known that PPIs can be context-specific and dependent on the cellular environment (Swaney et al., 2021). To capture these cell-type specific interactions, we performed AP-MS in A549 lung epithelial cells and primary normal human bronchial epithelial (NHBE) cells which are primary targets of IAV infection, and THP-1 human monocyte cells differentiated into a macrophage-like state (Chanput et al., 2014; Daigneault et al., 2010) which are a secondary target of IAV infection (**Figure 1.1**).

We codon optimized, cloned and Strep-tagged 13 virus proteins from the eight RNA segments of the IAV genome (**Figure 2.1A**). Collectively, these 13 proteins make up the consensus IAV proteome, and include: virus surface proteins (HA, NA) and a membrane-embedded ion channel (M2) involved in virus fusion and entry (HA, M2) and virus budding and release (M2, NA); an RNA-binding protein involved in viral genome trafficking (NP); proteins involved in viral genome transcription and replication (trimeric RNA-dependent RNA polymerase subunits PA, PB1 and PB2); proteins that facilitate viral RNA export from the nucleus (NEP, M1) and encapsidation of viral RNA during virus assembly (M1); proteins that modulate host immune response, host shutoff, virus pathogenicity and virulence (NS1, PA-X, PB1-F2); and a protein needed for efficient replication but whose cellular function is not well-characterized (N40) (Dou et al., 2018; Klemm et al., 2018; Wise et al., 2009). Nine of these 13 proteins are structural and packaged into virus particles, while the remaining four are predominantly involved in modulating host response (**Figure S2.1A**). All 13 proteins are expressed by all three IAV strains (i.e. pH1N1,

H3N2, and H5N1), except PB1-F2 which is not expressed by pH1N1 as it contains a premature stop codon in the pH1N1 viral genome (Garten et al., 2009; Wang and Palese, 2009). All strain-specific IAV proteins were cloned into a doxycycline-inducible mammalian expression vector that contains a 2xStrep-tag fused to either the C-terminus or N-terminus, except for HA which contains an internal 2xStrep-tag (**Figure 2.1A, Table S2.1**). C-terminal 2xStrep-tagged GFP and empty vector constructs were cloned and included as experiment controls.

Stable cell lines individually expressing Strep-tagged IAV proteins and controls were generated by lentiviral transduction in A549, NHBE and THP-1 cells (**Figure 2.1B, Methods**). THP-1 cells were subsequently treated with Phorbol-12-myristate-13-acetate (PMA) to induce differentiation into a macrophage-like state (Daigneault et al., 2010) (**Methods**). Following doxycycline-induced expression of Strep-tagged IAV proteins and controls, cells were lysed, Strep-tagged proteins were affinity purified and digested, and the resulting peptides separated and analyzed by LC-MS/MS to identify co-purified human proteins (**Figure 2.1B**). Nine IAV proteins from all three strains were successfully expressed in all three cell types, and all 13 proteins were expressed for at least one strain in at least one cell type, totaling 677 AP-MS samples collected across three IAV strains from three cell types (**Figure S2.1B, Figure S2.2**). Raw files were searched with MaxQuant (Cox and Mann, 2008), and IAV-human PPIs were scored by the Mass Spectrometry Interaction Statistics (MiST) algorithm (Jäger et al., 2011) that assigns quantitative interaction confidence scores based on specificity, abundance and reproducibility (**Table S2.1**). Using stringent MiST scoring and replicate cutoffs (**Methods**), we identified 332 total high-confidence PPIs across all strains and human cell types that mapped to 214 human prey proteins (**Table S2.1**). In comparison to previous studies that characterized IAV-human PPI networks (Heaton et al., 2016; Shapira et al., 2009; Tripathi et al., 2015; Wang et al., 2017; Watanabe et al., 2014), we observed higher similarity by odds ratio to studies that used AP-MS with exogenously expressed IAV proteins compared to yeast two-hybrid (**Figure S2.1C**). In

addition, this analysis indicates that there is a moderate degree of overlap between our dataset and others. For example, our study has the highest odds ratio with the Tripathi et al PPI network (**Figure S2.1C**), and 33 prey proteins are captured in both networks. In total, there are 44 human prey proteins identified in our study that were not found by any of the previous studies. These previous studies characterized one IAV strain (e.g. WSN H1N1 or PR8 H1N1) in one workhorse cell line (e.g. HEK293 or A549) permissive to IAV infection. Our study uniquely presents a stringently scored, high-confidence dataset that provides strain-specific and pan-IAV PPIs from three clinical isolate strains in three cell types relevant for IAV infection.

Collapsing across virus strains to identify unique PPIs by cell type, we observed that using multiple cell types substantially expanded the number of PPIs captured to give a comprehensive snapshot of IAV-human interactions (**Figure 2.1C**). 29/257 PPIs are shared in at least two of the three cell types. Collapsing across cell types to identify unique PPIs by virus strain, we identified 77 PPIs with pH1N1 among 8 baits, 77 PPIs with H3N2 among 10 baits and 142 PPIs with H5N1 among 11 baits (**Figure 2.1D**). For all three virus strains, NA was expressed at low levels (**Figure S2.2**), and therefore has no protein interactions that passed the scoring thresholds.

Comparing shared PPIs (expressed as Jaccard Index) against protein sequence similarity, we found a positive correlation (**Figure 2.1E**). We observed that homologous baits and some non-homologous baits with high sequence similarity share PPIs, highlighting protein sequence as a driving factor in determining these interactions (**Figure S2.1D-E**). This trend was also observed when comparing homologous proteins of related coronavirus species (Gordon et al., 2020a). For example, among non-homologous IAV baits, PB1 and N40 have high sequence similarity and share four unique PPIs (36.4% of total unique PB1 PPIs and 50% of total unique N40 PPIs). N40 is a N-terminal truncation product alternatively translated from the RNA segment encoding PB1, missing only 39 amino acids of PB1 (Wise et al., 2009). The functional

significance of overlapping PPIs with PB1 is unknown as N40's function is less understood. Among homologous baits, IAV NP has the highest number of shared PPIs between the three strains (**Figure S2.1F**). pH1N1 NP shares 18 PPIs (85.7% of its total PPIs), H3N2 shares 19 PPIs (95% of its total PPIs), and H5N1 shares 17 PPIs (56.6% of its total PPIs), potentially due to high sequence conservation of NP and NP's conserved role across strains in viral RNA binding, transcription, trafficking and packaging (Kukol and Hughes, 2014; Xu et al., 2011). Interestingly, overlap between both homologous and non-homologous baits is increased when comparing biological pathways among the PPIs for each bait (**Figure S2.1G**). This suggests that while baits of the different virus strains may target different specific human proteins, they co-opt similar processes or pathways. To expand on this, we performed gene ontology (GO) enrichment analysis to identify enriched molecular functions among human protein interactors for each bait across all strains and cell types (**Figure 2.1F, Table S2.1**). PPI enrichments include terms consistent with known biology of IAV proteins. For example, NS1 interactors are enriched for double-stranded RNA (dsRNA) binding proteins, consistent with reports that NS1 abrogates cellular dsRNA sensor signaling pathways through its ability to bind dsRNA (Lu et al., 1995; Min and Krug, 2006). NEP interactors are enriched for actin filament binding, which may expand on NEP's known role in nuclear export of viral RNA (O'Neill et al., 1998) and could indicate a novel function for NEP in post-export association with and trafficking of viral RNA along cytoskeleton filaments (Amorim et al., 2011). Enrichment terms also characterize IAV proteins of unknown function, such as heat shock protein binding and chaperone binding for N40, which may indicate a novel role for N40 in protein translation and/or stability. PB2 and HA have no significant enrichments that passed our thresholds, due to the small number of PPIs (**Figure 2.1D, Table S2.1**). However, M1, which also has a small number of PPIs, shows significant enrichment in PPIs with translational elongation factor activity. This is unexpected for M1, whose known functions include facilitating nuclear export and trafficking of viral RNA

(Huang et al., 2001; Martin and Helenius, 1991). It is unclear if these PPIs are involved in this activity or indicate an independent, novel activity of M1.

IAV PPI Networks from Three Cell Types Identify Strain-Specific and Pan-IAV-Human Interactions

In total, we identify 332 high-confidence PPIs across the three IAV strains in the three cell types collectively. These include PPIs between: 108 human proteins and nine IAV proteins in A549 cells; 88 human proteins and eight IAV proteins in NHBE cells; and 56 human proteins and eight IAV proteins in THP-1 cells (**Figure S2.3**). A number of these interactions are shared across at least two cell types. These include members of the cleavage and polyadenylation factor (CPSF) complex that interact with IAV NS1 in all three cell types, spliceosome components that interact with NP in NHBE and THP-1 cells, and mitochondrial ribosome subunits that interact with NP in NHBE, THP-1 cells (**Figure S2.3**). These complexes are known to be involved in processes supporting IAV infection, most notably RNA export and processing. For example, NS1 is known to interact with the CPSF complex to post-transcriptionally dampen host mRNA expression and innate immune response (Nemeroff et al., 1998; Noah et al., 2003). While the majority of the IAV-human PPIs are cell type-specific, it should be noted that several viral protein baits did not express well in all cell types (**Figure S2.1B**, **Figure S2.2**), and a number of the high confidence PPIs identified in one cell type were also identified in other cell types but below our stringent scoring thresholds (**Table S2.1**). Noting the small overlap shared between cell types (**Figure 2.1C**), we reasoned the three cell types collectively provide a snapshot of IAV-human interactions. Therefore, we collapsed PPIs across all cell types into one interactome to focus on visualizing strain-specific and pan-IAV interactions. This identified a total of 214 human proteins that interact with 12 IAV proteins (**Figure 2.2**). Every high-confidence interacting protein that passes our scoring thresholds in at least one cell type for at least one IAV strain is represented as a circular three-way pie chart in the network. The color intensity of each pie chart section is

proportional to the highest MiST score for each strain (**Figure 2.2**), which enables visualization of both high-confidence interactions that scored above our thresholds and interactions with additional IAV strain(s) detected in our AP-MS data that fell below our MiST score thresholds. We additionally mapped human-human PPIs reported in CORUM (Giurgiu et al., 2019) to identify human protein complexes and expanded upon the PPI molecular function enrichments (**Figure 2.1F**) to highlight biological processes identified across the PPIs (**Figure 2.2**).

The interactome highlights PPIs shared across all three viruses and strain-specific PPIs. Examples of interactions shared across all three strains include proteins and protein complexes involved in: RNA processing and translation, including the spliceosome (NP, 11 interactors), CDC5L complex (M2, 3 interactors), mitochondrial ribosome (NP, 17 interactors) and 60S ribosome (PA, 3 interactors); nuclear transport (M2, 10 interactors); macroautophagy (M2 and PB1-F2, 2 interactors); and fatty acid metabolism (M2, 10 interactors) (**Figure 2.2**). Identifying these PPIs across all three strains indicates these specific proteins may be highly important for IAV infection. The biological processes of these interactors are consistent with known roles of the corresponding virus proteins in viral genome replication and translation (NP, PA) and viral assembly or budding (M2). The interactome also highlights strain-specific PPIs, which are most noticeable among protein interactions of NS1, PA-X and PB1-F2 (**Figure 2.2**). These viral proteins are largely involved in modulating host response, and may represent unique co-opting of host protein complexes by each strain. For example, PB1-F2 H3N2 interactions are largely involved in protein chaperone activity, while H5N1 interactions are part of the S100A10-Annexin 2 protein complex that has roles in membrane trafficking, connecting cytoskeletal components to the cell membrane, and cell adhesion (Liu et al., 2015) (**Figure 2.2**). PB1-F2 has been described as a proapoptotic factor, modulator of innate immune response, and virulence factor that contributes to IAV pathogenicity (Chen et al., 2001; Varga et al., 2011; Vidy et al., 2016). It is unknown if the PB1-F2 interactions identified in our network contribute to its known activities,

or identify potential novel cellular roles for PB1-F2. It is also noticeable that H5N1 has a higher number of total interactions compared to pH1N1 and H3N2, especially among IAV proteins PA-X, M2, M1 and NEP. This may reflect true biological differences between the strains, or reflect differences in protein expression or stability of H5N1 proteins. This, for example, is evidenced by higher H5N1 PA-X protein expression in A549 cells (**Figure S2.2**).

The interactome also includes PPIs that are shared between two IAV bait proteins. In those cases, the maximum MiST score from either bait is reported in the network for each IAV strain. For example, SQSTM1 interacts with PB1-F2 and M2. PB1-F2 interacts with SQSTM1 scored above thresholds only with H3N2, and scored below thresholds with H5N1 (**Table S2.1**). SQSTM1 interaction with M2 is identified above scoring thresholds with H5N1, and below scoring thresholds with pH1N1 and H3N2 (**Table S2.1**). Network shading thus represents darker shading for H3N2 and H5N1 (high-confidence interactions with PB1-F2 and M2, respectively) and lighter shading for pH1N1 (M2 interaction that fell below scoring thresholds), representative of the MiST confidence scores as described above (**Figure 2.2**).

Some PPIs and their corresponding protein complexes or biological processes in our network have been previously reported (**Figure S2.1C**), which lends confidence to our network. For example, NS1 interacts with four PI3K signaling components (**Figure 2.2**). NS1 has been previously shown to activate PI3K signaling during infection to modulate host apoptotic response (Ehrhardt et al., 2007; Shin et al., 2007). In addition, NS1 interactions are predominantly identified with pH1N1 and H3N2, largely in part due to low expression of H5N1 NS1 in A549 cells (**Figure S2.2**), and therefore interactions for this bait did not pass stringent scoring thresholds (**Table S2.1**). Only one H5N1 NS1 interaction with PIK3R2 passed scoring thresholds (**Figure 2.2**). However, the network also identifies PPIs that we consider novel interactions not described by previous PPI studies (Heaton et al., 2016; Shapira et al., 2009;

Tripathi et al., 2015; Wang et al., 2017; Watanabe et al., 2014). For example, while HA is reported to interact with CANX for proper HA folding and processing at the ER (Daniels et al., 2003; Heaton et al., 2016), the additional three HA PPIs with ER protein quality control machinery are novel and may identify additional human proteins involved in HA folding and processing. These three additional PPIs (ERLEC1, SEL1L, P4HB) were identified only in A549 cells and only with H3N2 HA (**Figure S2.3, Table S2.1**). HA from all three strains did not express in NHBE or THP-1 cells, and pH1N1 HA did not express in any cell type (**Figure S2.2**). To our knowledge, N40 is an under-characterized protein, with limited studies identifying human PPIs or a cellular mechanism of action. Here, we identify seven high-confidence human protein interactors of N40, including six that are involved in protein quality control machinery, thus indicating a potential cellular role for N40 in modulating human and/or viral protein expression. Collectively, the interactome highlights the rich biology of human proteins and pathways targeted by three strains of IAV.

Methods

IAV strep-tagged plasmid and lentivirus construction. The coding sequences of 12 virus proteins for A/California/04/2009 H1N1 (does not express PB1-F2 (Garten et al., 2009; Wang and Palese, 2009)), 13 virus proteins for A/Wyoming/03/2003 H3N2 and 13 virus proteins for A/Vietnam/1203/2004 H5N1 were cloned into a pcDNA4/TO backbone vector, previously described in (Jäger et al., 2011). IAV proteins were cloned with either an N-terminal 2X-Strep tag (PB1-F2, NA, M1, M2, NS1, NEP), C-terminal 2X-Strep tag (PB2, PB1, N40, PA, PA-X, NP) or internal 2X-Strep tag (HA). Tag locations were selected as a best guess to maximize exposure of the tag epitope and minimize impact on protein structure (data not shown). DNA and amino acid sequences for all Strep-tagged IAV proteins, and Strep-tagged eGFP and empty-vector control proteins are reported in **Table S2.1**.

Tagged gene sequences of all IAV proteins were first cloned from the pcDNA4/TO vector into a pLVX-TetOne-Puro doxycycline inducible backbone vector (Takara, 631847) via Gibson Assembly. Gene inserts derived from PCR amplifications of pcDNA4/TO clones were designed with 15-30 base pairs of overlap with the backbone vector. Seven IAV proteins (PB1, PB1-F2, N40, NA, NS1, NEP, HA) had insufficient expression for AP-MS by this method. To improve protein expression, for these seven IAV proteins from all three strains, gene blocks of tagged constructs were instead codon-optimized using an online codon-optimization tool (Integrated DNA Technologies [IDT]) and synthesized (IDT), and subsequently cloned via Gibson Assembly into the pLVX-TetOne-Puro backbone vector. Gibson Assembly was performed as previously described (Gibson et al., 2009). Briefly, a 5X ISO Buffer was prepared with 3mL 1M Tris-HCl pH 7.5, 150µL 2M MgCl₂, 240µL 100mM dNTP mix (25mM each of dGTP, dCTP, dATP, dTTP), 300µL 1M DTT, 1.5g PEG-8000, 600µL 50mM NAD 3x (NEB, 9007S), and dH₂O to 6mL final volume. 5X ISO Buffer was stored at -20°C in 320µL aliquots. A Gibson Assembly master mix was prepared by combining 320µL of 5X ISO Buffer with 0.64µL 10U/µL T5 Exonuclease (NEB,

M0363S), 20µL 2U/µL Phusion Polymerase (NEB, M0530S), 160µL 40U/µL Taq DNA ligase (NEB, M0208L), and water to 1.2mL final volume. Gibson Assembly mastermix was stored at -20°C in 15µL aliquots. The pLVX-TetOne-Puro backbone was linearized with restriction enzymes BamHI-HF (NEB, R3136S) and EcoRI-HF (NEB, R3101S) in accordance with the manufacturer's recommendations. Gibson Assembly reactions were then performed by combining 20ng of linearized backbone with the insert gene of interest in a 1:2 molar ratio in 15µL of Gibson master mix plus water to a final volume of 20µL. Reaction mixtures were then incubated for 30 minutes at 50°C.

pLVX-TetOne-Puro PA-X-encoding constructs were additionally cloned to include a D108A point mutation in the catalytic RNA endonuclease domain of PA-X. Catalytic IAV PA-X caused cell toxicity; therefore, we cloned a D108A substitution previously shown to inactivate endonuclease activity (Hara et al., 2006; Jagger et al., 2012). Briefly, D108A mutagenesis was performed by QuikChange site-directed mutagenesis (Agilent, 200518) on pLVX-TetOne-Puro PA-X constructs following manufacturer's protocol adapted with Velocity enzyme (BioLine, BIO-21099) under the following conditions in a Bio-Rad C1000 Touch Thermal Cycler: 98°C for 30 seconds - 2 minutes, 18 cycles of 98°C for 30 seconds followed by 55°C for 1 minute and 72°C for 5-10 minutes, and final extension at 72°C for 3 minutes. pLVX pH1N1 PA-X D108A 2X-Strep and pLVX H5N1 PA-X D108A 2X-Strep were generated by QuikChange mutagenesis alone. H3N2 PA-X D108A 2X-Strep was subjected to mutagenesis as described above, amplified by PCR with Phusion enzyme (NEB, M0530L), and cloned into empty pLVX-TetOne-Puro vector by InFusion cloning (Takara, 638911) following manufacturer recommendations.

Stable IAV protein-expressing cell line generation and culture. A549 (ATCC, CCL-185) cells were cultured in T175 flasks (Fisher, 12-556-011) at 37°C and 5% CO₂ in DMEM with L-glutamine without sodium pyruvate (Fisher, MT 10-017-CV), 10% FBS (Life Technologies,

A3160502) and 1X Penicillin/Streptomycin (Pen/Strep) (Fisher, MT 30-002-CI). NHBE (Lonza, CC-2541) cells were cultured in collagen I-coated T175 flasks (Fisher, 356487) at 37°C and 5% CO₂ in Bronchial Epithelial Basal Medium (BEBM) (Lonza, CC-3171) with nine supplemental singlequots from the Bronchial Epithelial Cell Growth Medium (BEGM) kit (Lonza, CC-4175). THP-1 (ATCC, TIB-202) cells were cultured in T175 flasks at 37°C and 5% CO₂ in RPMI-1640 with L-glutamine (Fisher, MT10040CV) supplemented with 10% FBS, 10mM HEPES (Fisher, SH3023701), 1mM sodium pyruvate (Fisher, MT 25-000-CI) and 1X Penicillin/Streptomycin (Pen/Strep).

For transduction of A549 and NHBE, cells were seeded in appropriate growth media at 5×10^5 cells per T75 flask (A549) or approximately 2 million cells per collagen I-coated T175 flask (NHBE), transduced with 250-500 μ L lentivirus containing the IAV transgene of interest, and returned to incubate at 37°C for 48 hours. Media was subsequently removed and replaced with appropriate cell growth media supplemented with 1 μ g/mL puromycin (A549) or 0.5 μ g/mL puromycin (NHBE) for transgene selection. Cells were expanded in selection media as polyclonal pools for four days (A549) or 48 hours (NHBE), to nearly 100% confluence. Cells were then split 1:6 and seeded in six replicates in selection media, equating to about 2 million cells per 15cm dish (A549) (Fisher, 430599) or collagen I-coated 15cm dish (NHBE) (Fisher, 08-774-9), and allowed to incubate for further expansion and transgene expression. Transgene expression was induced at three days (A549) and five days (NHBE) after seeding cells into 15cm format.

For transduction of THP-1, cells were seeded in 2mL appropriate growth media at 1 million cells per well in a 6-well plate (Fisher, 08-772-1B). Cells were transfected in 6-well plate format with 25 μ L lentivirus containing the IAV transgene of interest and returned to incubate at 37°C for 48 hours. Cells containing the transgene were selected by incubation with growth media

supplemented with 0.75 μ g/mL puromycin for 72 hours. For subsequent monoclonal selection, cells were serially diluted to 150 cells/mL in growth media supplemented with 0.25 μ g/mL puromycin, diluted again 1:40 in selection media and plated into 96-well flat-bottom plates (Fisher, 08-772-2C). Cells were incubated at 37°C for 3-4 weeks in selection media to allow single cell colony outgrowth. 12 colonies per transgene were selected, expanded for roughly 12 days in selection media into 24-well plates, and screened for inducible, sufficient transgene expression by doxycycline treatment (below) followed by immunoblot. Four successful monoclonal isolates per transgene were expanded in selection media into T175 flasks to a density of 1x10⁶ cells/mL in a final volume of 100mL. Following monoclonal expansion, cells were differentiated into a macrophage-like state with phorbol 12-myristate 13-acetate (PMA) (Fisher, BP685-1). Briefly, 25 million THP-1 cells from each of the four monoclonal pools were plated in growth media supplemented with 0.25 μ g/mL puromycin and 30nM PMA in four 15cm dishes, two dishes per replicate. THP-1 cells were PMA-differentiated for 48 hours before transgene expression was induced. Each monoclonal isolate serves as a replicate for THP-1.

To induce transgene (IAV protein) expression in A549, NHBE and THP-1, cells were treated with doxycycline (Fisher, AAJ6057914) at final concentration 2 μ g/mL for a total of 24 hours. 12 hours after doxycycline treatment, one set of replicates was treated with universal type I interferon (PBL Assay Science, 11200-2) at final concentration 1000U/mL for 12 hours to stimulate an antiviral-like state, and one set of replicates remained untreated. There were few discernible differences in observed protein-protein interactions between treated and untreated replicate sets, therefore replicate sets were collapsed as biological replicates totaling six replicates (A549 and NHBE) or eight replicates (THP-1) to increase statistical power. To achieve sufficiently high protein levels of PB1-F2 in all cell types, PB1-F2-expressing cells were treated with proteasome inhibitor MG-132 (Sigma-Aldrich, 474790) at final concentration 5 μ M at 12 hours after doxycycline treatment for 12 hours before harvest and affinity purification.

PPI sample harvest and affinity purification. To harvest IAV protein- and control bait-expressing A549 and NHBE cells, cells were washed in 10mL 1X phosphate buffered saline (PBS) (Fisher, MT 46-013-CM) and detached from plates by cell scraper (Fisher, 50-809-263) in 10mL 1X PBS followed by a 4mL wash for a 14mL final cell suspension per replicate. THP-1 cells were washed in 10mL 1X PBS and detached by cell scraper in 10mL 1X PBS, and two dishes per replicate were combined. Each dish was then washed with an additional 5mL per plate for a final combined 30mL cell suspension per replicate. Cells were pelleted at 2000rpm, 4°C for 5 minutes, supernatant was aspirated, and pellets were resuspended in 1ml cold lysis buffer (IP buffer pH 7.4 at 4°C [50 mM Tris-HCl, pH 7.5, 150 mM NaCl, 1 mM EDTA] supplemented with 0.5% Nonidet P40 substitute [NP40] (United States Biological, 9036-19-5), Complete mini EDTA-free protease inhibitor (Roche, 11836153001) and PhosSTOP phosphatase inhibitor (Roche, 04906837001). Samples were transferred to 1.5mL epi tubes (Fisher, 05-408-129) and rotated at 4°C for 30 minutes. Samples were subsequently frozen at -80°C for a minimum of 30 minutes, or until affinity purification.

Affinity purification was performed against the Strep tag with 50% suspension Strep-Tactin Sepharose beads (IBA, 2-1201-010). 20µL bead volume (40µL 50% slurry) per sample was washed in IP buffer pH 7.4 at 4°C, pelleted at 1000rpm for 5 minutes and resuspended in 640µL cold IP buffer per sample (total 660µL bead suspension). 660µL bead suspension was then transferred to one 2mL dolphin tube per sample (VWR, 53550-148). During this time, samples were thawed at room temperature for 20-30 minutes, and clarified by centrifugation at 3500 x g, 4°C for 20 minutes to pellet debris. 50µL lysate (input) was reserved for immunoblotting. 950µL remaining lysate per sample was transferred to the corresponding 2mL dolphin tube containing Strep-Tactin Sepharose beads and incubated for 4 hours at 4°C with rotation. Beads were subsequently pelleted at 2000rpm, 4°C for 4 minutes, and 50µL flow-through was reserved for

immunoblotting before flow-through was discarded. Beads were washed twice in 1mL cold wash buffer (IP buffer pH 7.4 at 4°C with 0.05% NP40) and twice in 1mL cold IP buffer (no NP40) by inverting 15 times and pelleting again 2000rpm, 4°C for 4 minutes. After the final wash, beads were resuspended in 450µL cold IP buffer, transferred to lo-bind 0.6mL epitubes (Axygen, MCT-060-L-C) with wide-orifice tips (Rainin, 17007099) and pelleted at 2000rpm, 4°C for 4 minutes. Supernatant was aspirated by 1mL syringe (BD Biosciences, 309628) and 27-G needle (BD Biosciences, 309659), and beads were immediately processed for on-bead digestion.

Immunoblotting. To verify transgene expression in THP-1 monoclonal isolates, 500µL suspensions of doxycycline-induced cells from a 24-well plate were transferred to 1.5mL epitubes and pelleted at 8000rpm for 2 minutes. Supernatant was removed, and cells were washed with 500µL 1X PBS, pelleted again and resuspended in 100µL 2.5X reducing sample buffer (31.2mM Tris-HCl pH 6.8, 10% glycerol, 1% SDS, 0.83% beta-mercaptoethanol, 0.0126% bromophenol blue). Cell samples were vortexed, boiled at 98°C for 30 minutes, vortexed again and cooled to room temperature before storage at -20°C. Verification of transgene expression in A549 and NHBE cells was done at the time of affinity purification. To prepare affinity purification samples for immunoblot, 50µL input or 50µL flow-through was combined with 50µL 2.5X reducing sample buffer, vortexed, boiled at 98°C for 30 minutes, vortexed again and cooled to room temperature before storage at -20°C.

For immunoblotting, samples were thawed at room temperature, and 10µL was loaded into each well of a 26-well 4–20% Criterion™ TGX™ Gel (Bio-Rad, 567-1094). Gels were run at 90 volts for 30 minutes followed by 150 volts for 50 minutes. The samples were then transferred at 0.25 amps for 1 hour to a PVDF Membrane (Bio-Rad, 1620177). Following protein transfer, membranes were blocked in 4% milk in PBST for 1 hour at room temperature, and then incubated with 1:1000 mouse anti-STREP antibody (Qiagen, 34850) in blocking solution

overnight at 4°C. Membranes were washed three times in PBST for 5 minutes each, and then incubated with 1:5000 goat anti-mouse IgG-HRP antibody (Bio-Rad, 170-6516) for 1 hour at room temperature. Membranes were washed three times and stained with Pierce ECL Western Blotting Substrate (ThermoFisher, 32106). Exposures of the blots were taken with autoradiography film (Thomas Scientific, XC59X), and developed with a medical film processor (Konica Minolta Medical & Graphic, SRX-101A). Film was scanned at 300 pixels/inch and stored as 8 bit grayscale TIFF files.

On-bead digestion and peptide desalting. Bead-bound proteins were reduced and alkylated by incubation in one bead volume equivalent of reduction/alkylation buffer (2M urea, 50mM Tris pH 8.0, 1mM Dithiothreitol [DTT] (Sigma, D5545), 3mM iodoacetamide (Sigma, I1149) in HPLC-grade water) for 45 minutes in the dark with gentle agitation to ensure bead suspension. Iodoacetamide was quenched with an additional 3mM DTT. Bead-bound proteins were then digested by incubation with 750ng sequencing-grade trypsin (Promega, V5111) per 10µL bead volume, and incubated overnight at 37°C. Resulting in-solution peptides were extracted from beads by gel-loading tips (Fisher, 02-707-81) into a fresh 0.6mL lo-bind eptitube for each sample and acidified by addition of HPLC-grade formic acid (Fisher Chemical, A117-50) to final concentration 1%.

Acidified peptides were desalted for MS analysis using HPLC-grade reagents and OMIX C18 10µL tips (Agilent Technologies, A5700310K) according to manufacturer's protocol. Briefly, OMIX tips were conditioned with 50% acetonitrile, 0.1% formic acid and equilibrated with two washes of 0.1% formic acid. Peptides were bound to C18 zip-tip by repeated rinsing. Polymer-bound peptides were washed three times with 0.1% formic acid and eluted in 50% acetonitrile, 0.1% formic acid. A second elution in 90% acetonitrile, 0.1% formic acid was performed to

increase peptide recovery. Peptides were lyophilized by vacuum centrifugation (CentriVap Cold Trap, Labconco) and stored at -20°C until MS analysis.

PPI MS data acquisition and analysis. Digested, desalted and dried peptides were dissolved in 12µL 2% acetonitrile, 0.1% formic acid. 2µL of each sample were injected in technical singlet for LC-MS/MS analysis onto an Easy-nLC 1000 (Thermo Fisher Scientific) coupled to a Orbitrap Elite Hybrid Mass Spectrometer (Thermo Fisher Scientific). Briefly, peptides were separated on a 75µm x 25cm fused silica IntegraFrit capillary packed with 1.9µm Reprosil-Pur C18 AQ reversed-phase resin (Dr. Maisch GMBH, r119.aq) over a 120min gradient at a flow rate of 300 nL/minute as described in **Table S2.2**. Buffer A consisted of 0.1% formic acid (FA) in water, and buffer B was 0.1% FA in acetonitrile. For each cycle, one full MS scan in the Orbitrap (150-1500 m/z, at 120,000 resolution with an AGC target of 1×10^6 and maximum injection time of 100 milliseconds) was followed by 20 data-dependent MS/MS scans acquired in the linear ion trap (AGC target 3×10^4 , maximum injection time of 50 milliseconds, fragmented by normalized collision energy at 35%). Target ions already acquired in MS/MS scans were dynamically excluded for 20 seconds (tolerance of 10 ppm). Detailed MS acquisition parameters are reported in **Table S2.2**.

Raw MS files from IAV proteins from all strains and control bait samples were grouped separately by cell line and searched simultaneously within each group using MaxQuant (version 1.6.2.10) (Cox and Mann, 2008). MS/MS spectra were searched against the human proteome (SwissProt human canonical sequences, downloaded 09 October 2018), IAV protein sequences and the eGFP sequence. Trypsin (KR|P) was selected to allow up to two missed cleavages. Variable modifications were assigned for: methionine oxidation and N-terminal protein acetylation. One static modification was assigned for carbamidomethyl cysteine. Label free quantitation (LFQ) was enabled. All other MaxQuant settings were left at the default.

MaxQuant-analyzed data were then scored using the MiST algorithm (Jäger et al., 2011), following previous guidelines (Verschuere et al., 2015) using spectral counts as the quantifying feature. To enable robust scoring, we excluded samples with low spectral counts and low or no bait protein identification, and those with less than two replicates. Following these quality control filtering steps, 590 samples across 14 baits remained for analysis. We ran the MiST algorithm applying a weight set of specificity $S=50\%$, reproducibility $R=45\%$ and abundance $A=5\%$. To identify high-confidence PPIs, we applied a set of stringent scoring criteria: (1) MiST score >0.6 ; (2) the interaction is absent in eGFP and empty-vector control samples; and (3) at least 4/6 replicates have a spectral count >0 . IAV M2 protein in A549 cells and IAV NP protein in NHBE cells retained a disproportionately large number of interactions, therefore we applied more stringent scoring criteria to these two specific samples: (1) MiST score >0.75 ; (2) the interaction is absent in eGFP and empty-vector control samples; (3) at least 5/6 replicates have a spectral count >0 ; and (4) average spectral count >3 . Interactions that fall above these cutoffs represent the final high-confidence PPI list, and contain a total of 126 interactions in A549 (top 4% of interactions), 130 interactions in NHBE (top 9% of interactions), and 76 interactions in THP-1 (top 5% of interactions) (**Table S2.1**). This list was used for further bioinformatic analyses and validation.

Computational analyses methods

Data and Code Availability. At the time of dissertation submission, mass spectrometry metadata for PPI samples are in the process of being deposited to the ProteomeXchange Consortium via the PRIDE partner repository (Perez-Riverol et al., 2019). R package source materials for MiST and Mass Spectrometry Statistics and Quantification (MSstats, version 3) are publicly available through the Krogan Lab GitHub: <https://github.com/kroganlab>. Further

information on MiST scoring can be found on the Krogan Lab GitHub:

<https://github.com/kroganlab/mist>.

Gene Ontology (GO) enrichments. For PPI GO enrichments, the human interacting proteins of each bait were collated across all strains and cell types, and tested for enrichment of GO Molecular Function terms. The over-representation analysis was performed using the enrichGO function of clusterProfiler package (version 3.18.0) in R with default parameters. GO terms were obtained from the R annotation package org.Hs.eg.db (version 3.12.0). Significant GO terms were defined as those with p-value < 0.002. Terms with overlapping genes in each set were compared and the most significant term (lowest p-value) with the largest gene set size was selected as the non-redundant term. PPI enrichments were subject to further manual curation, with a maximum of the top three significant non-redundant GO terms listed and visualized for each bait (**Table S2.1**).

Network visualizations. All networks were generated and visualized in Cytoscape (version 3.8.2) (Shannon et al., 2003). For the IAV-human PPI network, IAV-human PPIs were represented by strain and collated across all cell types. In cases where one human protein is shared between two IAV bait proteins, the maximum MiST score from either bait in any cell type was reported for each IAV strain. Human-human PPIs were annotated as reported in the comprehensive resource of mammalian protein complexes (CORUM) database (Giurgiu et al., 2019). Manual annotations to the network include human-human PPI protein complex name and biological process. Briefly, human prey proteins for each bait were subjected to gene set enrichment analysis using either GO Biological Process terms or CORUM protein complex annotations. Genes that were members of enriched biological processes or protein complexes were labeled in the network using Adobe Illustrator software (v24.1). Labels were manually curated to simplify and generalize terms to facilitate interpretability. Genes mapped under a GO

Biological Process term were manually investigated to ensure the term represented each gene's canonical function; genes that clearly possessed multiple functions, or genes that were otherwise difficult to classify, were excluded to reduce the appearance of misleading annotations.

FIGURES AND LEGENDS

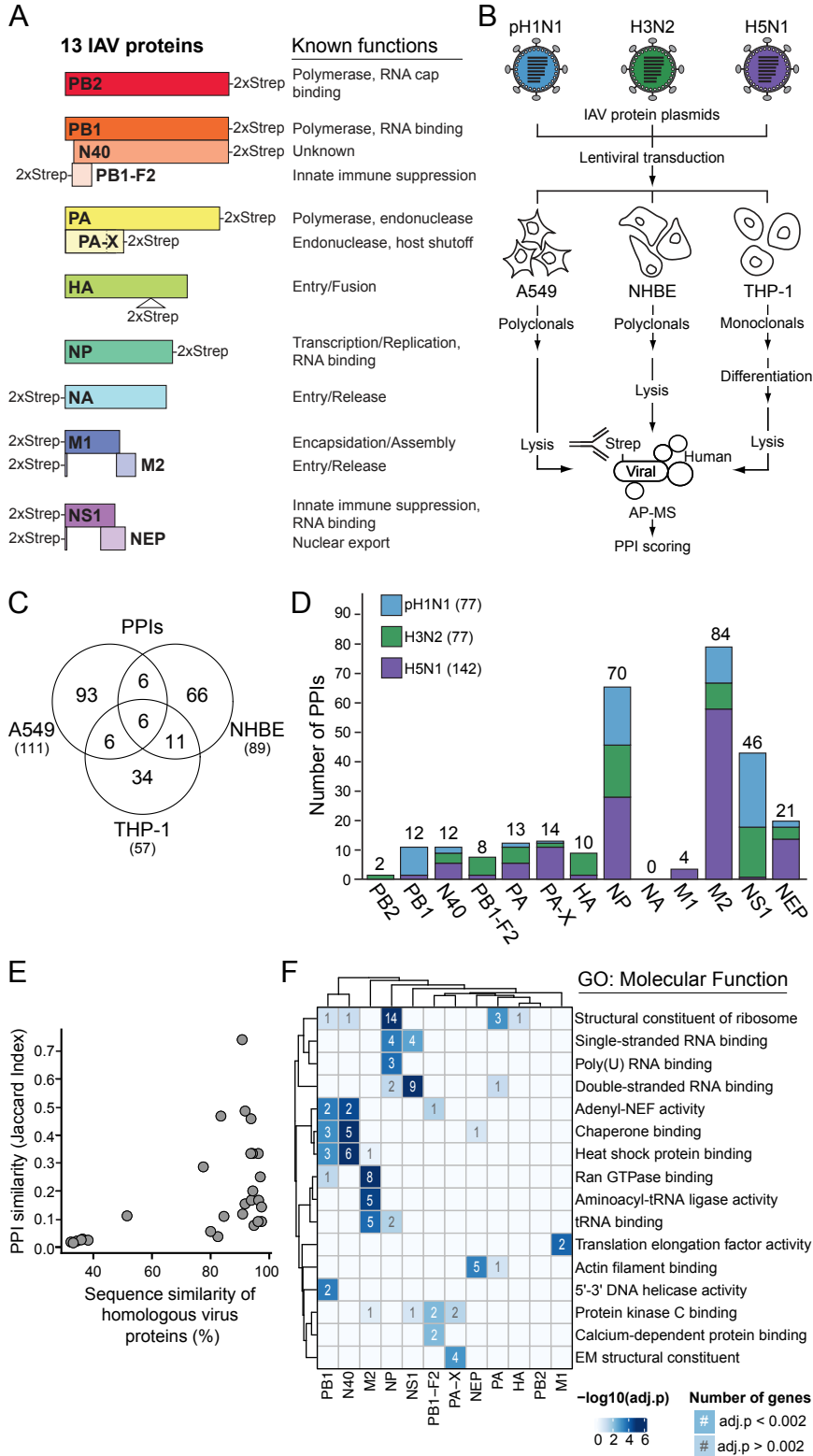


Figure 2.1 AP-MS identifies pH1N1, H3N2 and H5N1 IAV-human PPIs. (A) Schematic of the 13 IAV bait proteins with internal, N- or C-terminal 2xStrep-tag (left) and their known biological functions (right). IAV proteins are drawn to scale and grouped by genomic RNA segment, showing protein products from each segment of the viral genome. (B) AP-MS experiment design to identify human proteins co-purified with Strep-tagged bait proteins from pH1N1, H3N2 and H5N1 IAV in A549, NHBE and THP-1 cell types. 2xStrep-tagged proteins were individually transduced by lentivirus into A549, NHBE and THP-1 cells. A549 and NHBE cells were cultured as polyclonal pools. THP-1 cells were cultured as monoclonal isolates and subsequently treated with PMA to induce differentiation into a macrophage-like state. All cells were treated with doxycycline to induce IAV protein expression and lysed. IAV-human PPIs were purified and identified by AP-MS, and scored to assign interaction confidence. (C) Venn diagram of unique IAV-human PPIs identified in each cell type used in this study. PPI numbers reported are collapsed across virus strains. (D) Bar graph of the unique IAV-human PPIs identified for each IAV protein and strain. PPI numbers reported are collapsed across cell types. (E) Comparison of shared protein interactions (PPI similarity) by Jaccard index against IAV protein sequence similarity. PPIs reported are collapsed across cell types. (F) Heatmap of gene ontology (GO) molecular function enrichments among the human interacting proteins of indicated IAV proteins, collapsed across all strains and cell types and clustered by correlation of enrichment profiles. GO terms were curated from the top 3 non-redundant terms with at least 2 genes for at least one IAV protein. Increasing shading intensity reflects increasing significance of the enrichment term. Numbers of proteins per enriched cluster are shown in white if significant (p -value <0.002), and grey if not significant (p -value >0.002).

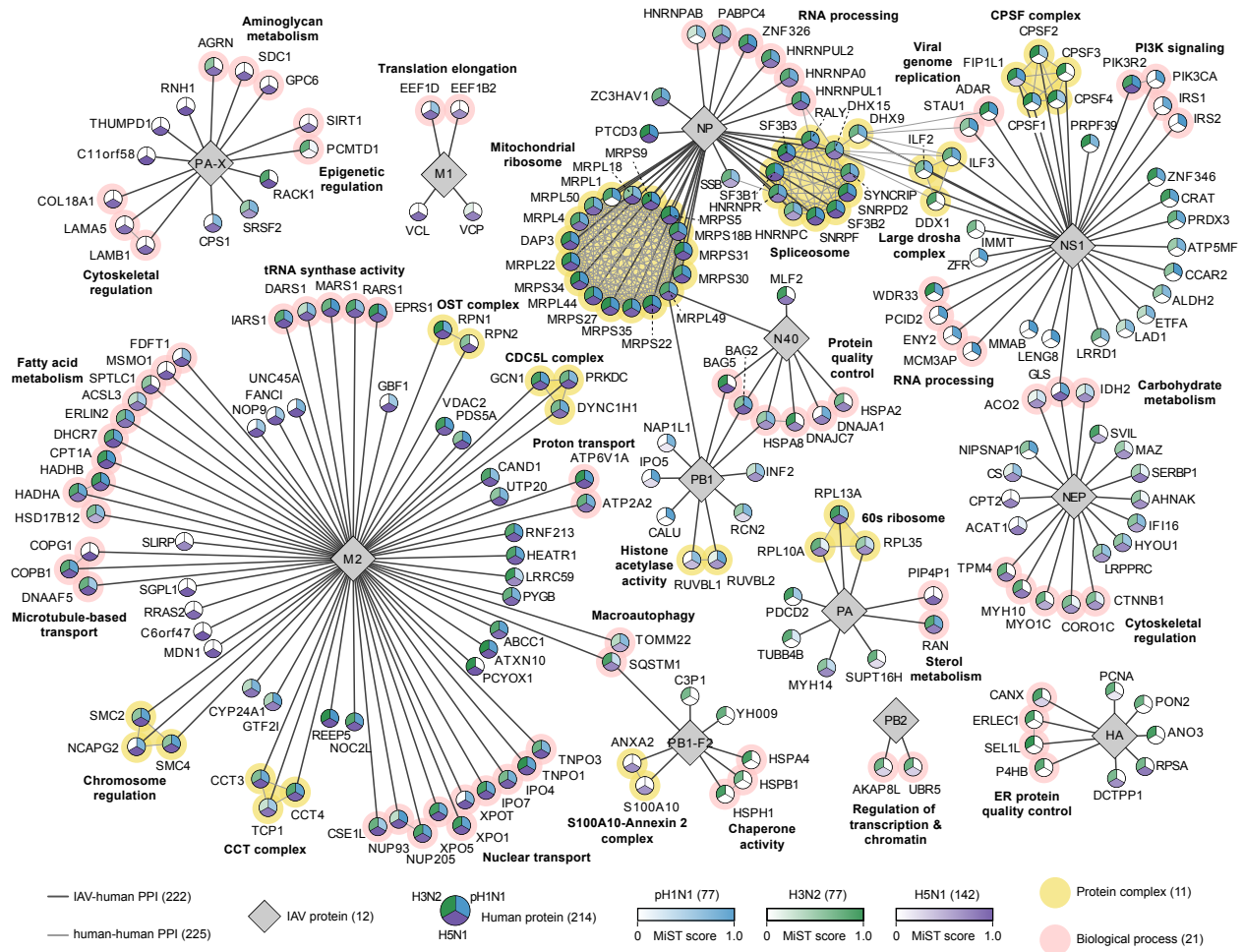
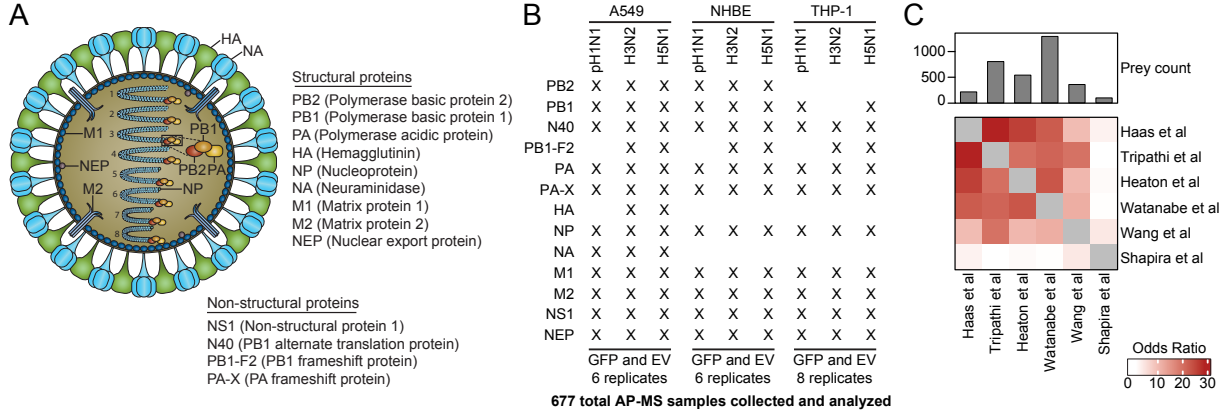


Figure 2.2 IAV PPI networks from three cell types identify strain-specific and pan-IAV-human interactions. High-confidence IAV-human PPIs between 12 IAV proteins (gray diamonds) and 214 human proteins (circular nodes) identified from three IAV strains collapsed across the three cell types. Human protein nodes are split into three sections and colored by the IAV strain for which the interaction was identified: pH1N1 (blue), H3N2 (green) and H5N1 (purple). Color shading is proportional to MiST PPI confidence score (scale at bottom; not identified represented by white color). IAV-human PPIs are depicted (dark grey lines), and human-human PPIs are identified (light grey lines) as curated in the CORUM (Giurgiu et al., 2019) database. Human protein complexes (yellow halo) are labeled as described in CORUM (Giurgiu et al., 2019), and biological processes (pink halo) are labeled as described by GO terms.



677 total AP-MS samples collected and analyzed

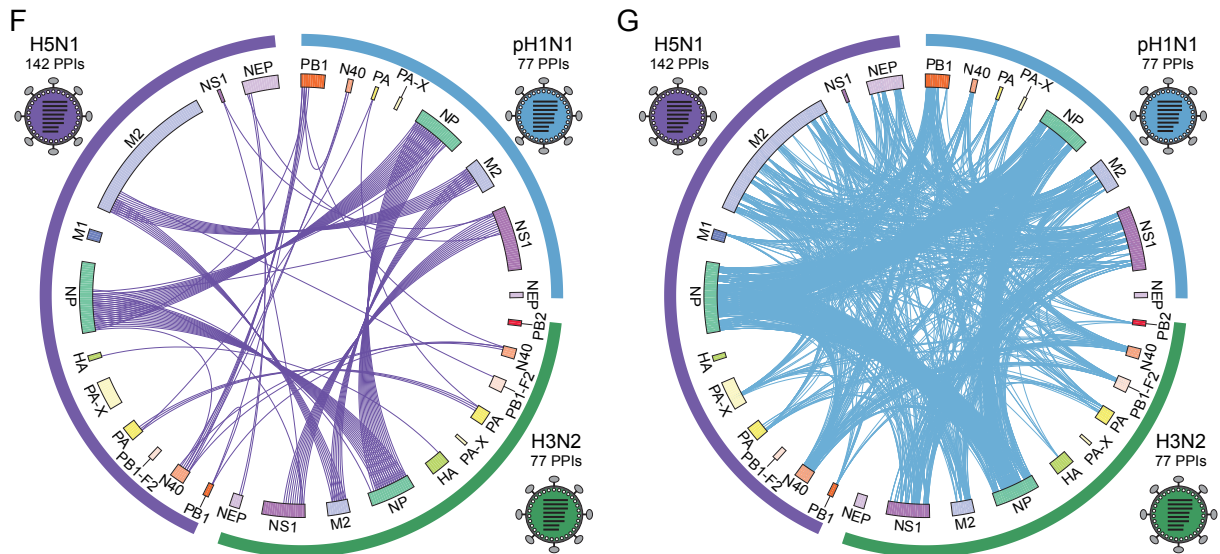
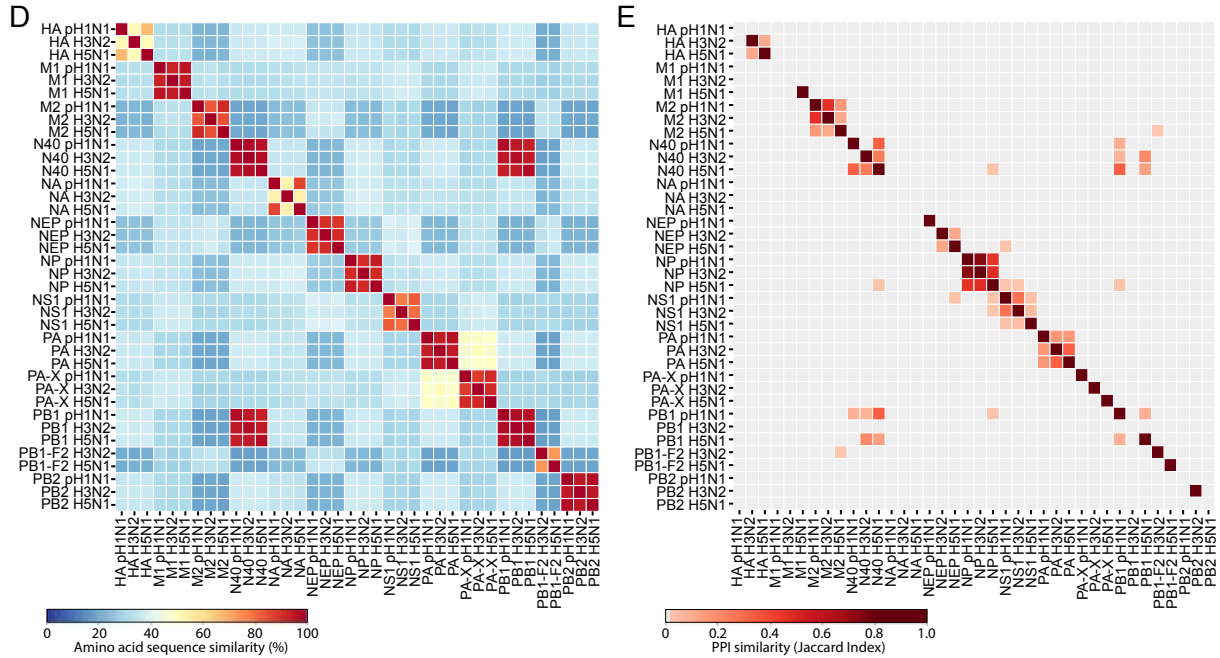


Figure S2.1 Summary of IAV AP-MS data, Related to Figure 2.1. (A) Infographic of IAV proteins depicted in an IAV particle, with the nine structural proteins and four non-packaged proteins included in this study. (B) AP-MS samples successfully collected and analyzed across the 13 IAV bait proteins from the three IAV strains and three cell types, marked by an “X”. pH1N1 does not express PB1-F2 (Garten et al., 2009), therefore no samples were generated. GFP and empty vector (EV) control bait samples were also collected in each cell type. Number of replicates for each bait in each cell type are listed. (C) ID correlation matrix comparing the human interacting proteins identified by AP-MS in this study with other published studies that used AP-MS with affinity-tagged IAV proteins exogenously expressed in cell lines (Tripathi et al., 2015; Watanabe et al., 2014), AP-MS in the context of virus infection (Heaton et al., 2016; Wang et al., 2017), and an orthologous yeast two-hybrid approach (Shapira et al., 2009). (D) Heatmap comparing percent amino acid sequence similarity across the total 38 IAV proteins (12 from pH1N1 which excludes PB1-F2, 13 from H3N2 and 13 from H5N1). (E) Heatmap comparing PPI similarity expressed as Jaccard index for human proteins interacting with the total 38 IAV proteins. (F-G) Circos plots representing the human interacting proteins shared between IAV proteins of the three strains (F, purple lines) or biological pathways of the human interacting proteins shared between IAV proteins of the three strains (G, blue lines). Inner circle depicts the IAV bait proteins (bars for each IAV protein colored as in **Figure 2.1A** and scaled to the number of interactions). Outer circle depicts the IAV strain (pH1N1 blue, H3N2 green, H5N1 purple; bar scaled to the number of interactions).

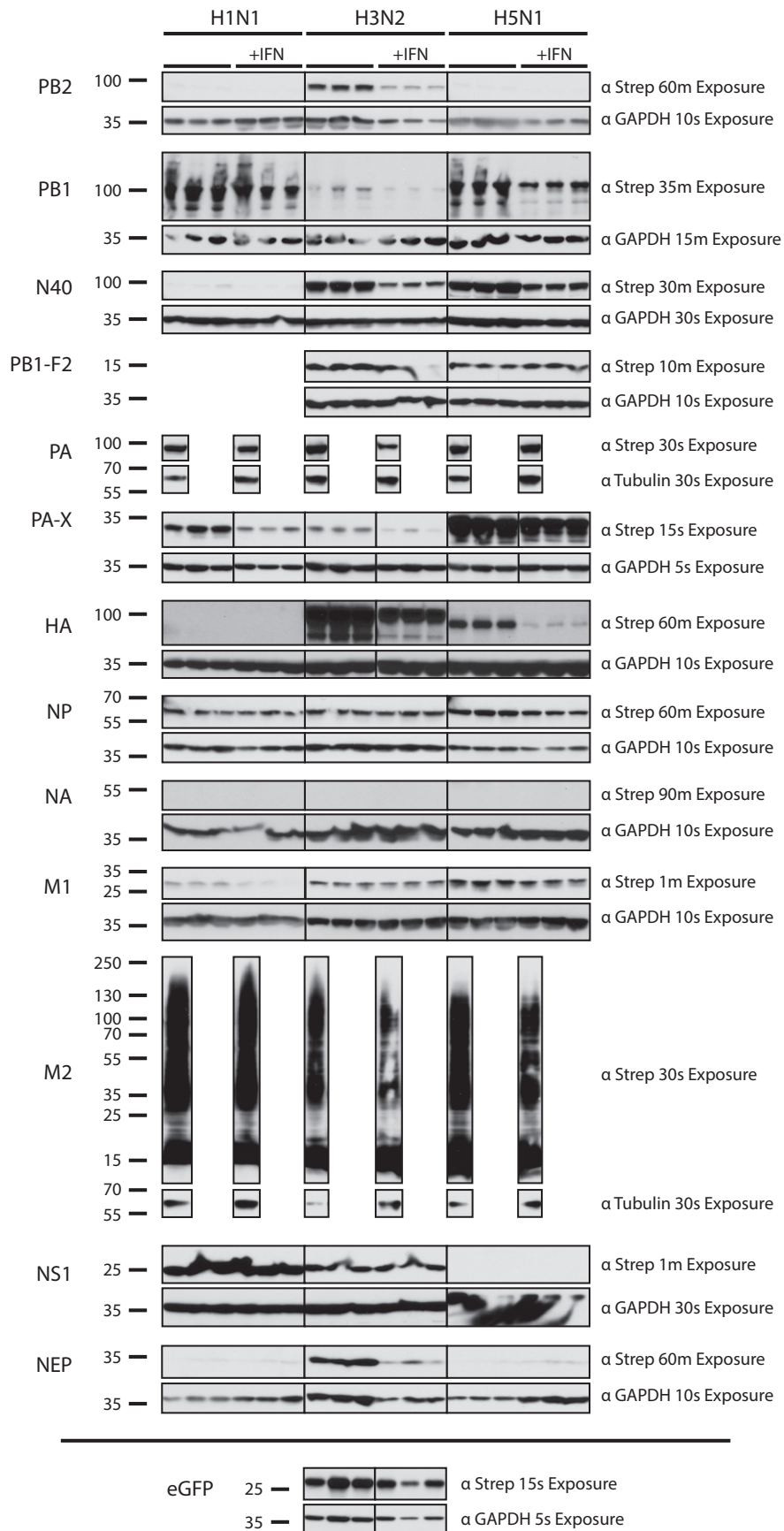
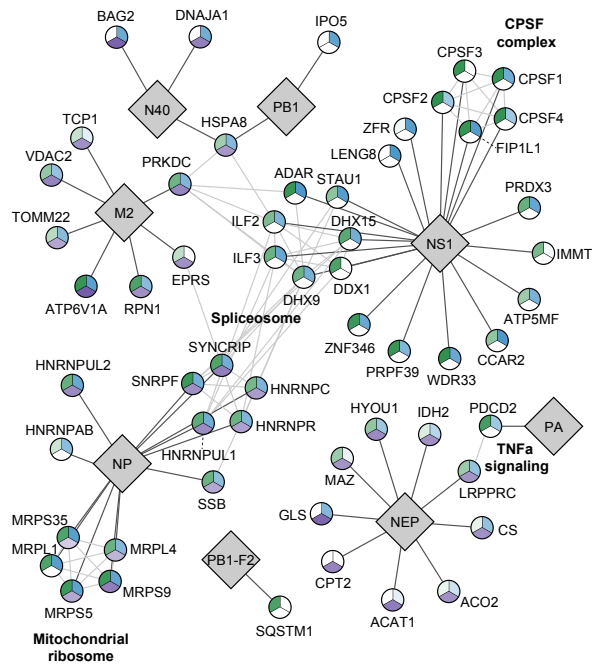
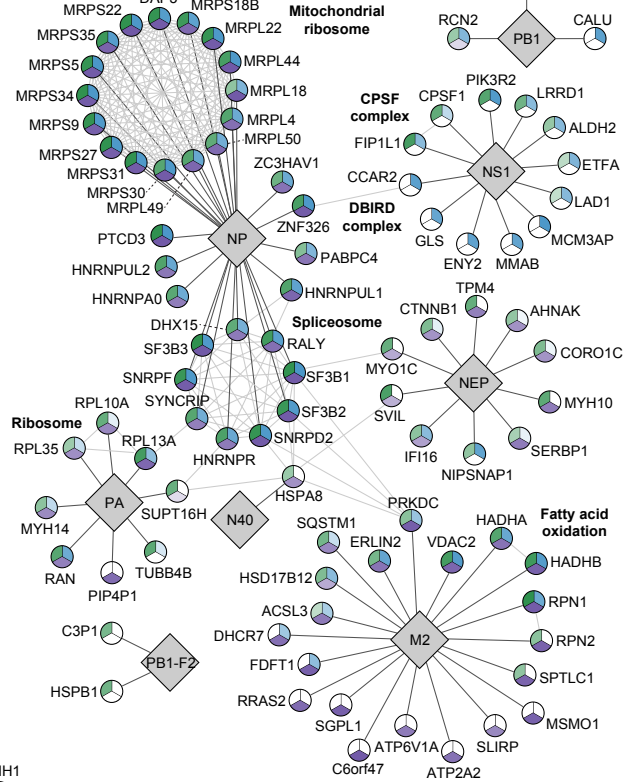


Figure S2.2 IAV protein expression, Related to Figures 2.1 and 2.2. Western blots probing against the 2xStrep-tag to assay IAV protein expression in A549 cells (shown). pH1N1 HA 2xStrep clone did not express. While expression of IAV proteins in other cell types was tested concurrently with AP-MS and verified, access to the data from other contributing authors was unavailable for inclusion at the time of dissertation submission. Please refer to the published manuscript (Haas et al.) for the full figure. (Data not shown: IAV bait protein expression in NHBE cells. HA 2xStrep clones and NA 2xStrep clones from all three strains did not express. IAV bait protein expression in PMA-differentiated THP-1 cells. Baits that did not express include: HA 2xStrep clones from all strains, NA 2xStrep clones from all strains, PB2 2xStrep clones from all strains, and H3N2 PB1 2xStrep.)

THP-1 IAV-Human PPI Network



HTBE IAV-Human PPI Network



A549 IAV-Human PPI Network

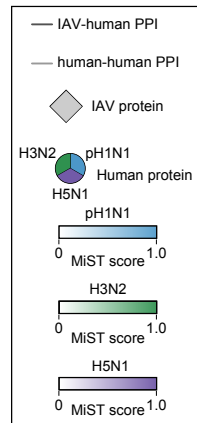
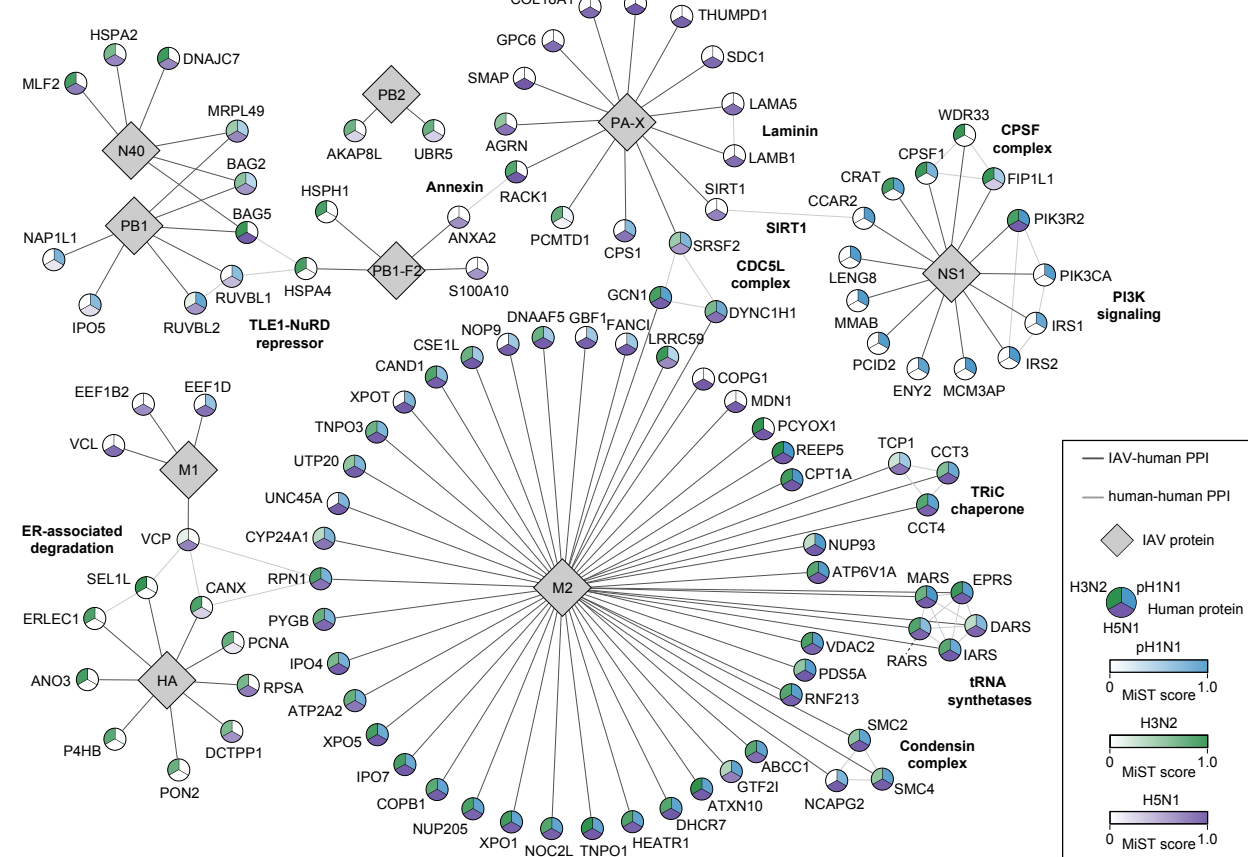


Figure S2.3 PPI networks specific to each cell type, Related to Figure 2.2. PPI networks specific to each cell type. 76 total high-confidence IAV-human PPIs across all strains in PMA-differentiated THP-1 cells are mapped between eight IAV proteins and 56 human proteins (top, left). 130 total high-confidence IAV-human PPIs across all strains in NHBE cells are mapped between eight IAV proteins and 88 human proteins (top, right). 126 total high-confidence IAV-human PPIs across all strains in A549 cells are mapped between nine IAV proteins and 108 human proteins (bottom). IAV protein nodes and human protein nodes are colored as described in **Figure 2.2**. Human-human PPIs are identified as curated in CORUM (Giurgiu et al., 2019) and labeled as described in **Figure 2.2**.

SUPPLEMENTAL TABLES

Table S2.1 AP-MS IAV protein sequences, scored IAV-human PPIs and PPI enrichments, Related to Figures 2.1, 2.2, S2.1, S2.2 and S2.3. Sequences of IAV and control proteins for AP-MS, including tag location, codon-optimization, sequence notes, and full protein and DNA sequences for proteins encoded by pH1N1, H3N2 and H5N1 (Protein_sequences_for_APMS tab). Full list of unfiltered MiST-scored PPIs (Full_PPI_List tab) and thresholded high-confidence scored PPIs (Filtered_PPI_List tab) between 13 proteins from three IAV strains and human proteins in three cell types. Scoring thresholds are described in **Methods**. Column descriptions for PPI lists are provided (PPI_List_Column_Descriptions tab). Finally, Gene Ontology (GO) molecular function (MF) enrichments for PPIs are reported for each IAV protein collapsed across all strains and cell types, with the full enrichment list (PPI_GO_MFfull tab) and with heatmap selection criteria of p-value < 0.002 and top 3 non-redundant terms with at least 2 genes for at least one bait (see also **Methods**) (PPI_GO_MFselection tab). Column descriptions for GO MF lists are provided (GO_List_Column_Descriptions tab). Table is available online only as supplemental material.

Table S2.2 PPI liquid chromatography (LC) and mass spectrometry (MS) acquisition parameters, Related to Methods. LC and MS acquisition parameters are reported for the instrument that acquired PPI data in our study. A table summary is included matching the instrument to their respective LC and MS parameters tabs and to the global proteomic data collected on the instrument, including data type, cell type and IAV strain. Table is available online only as supplemental material.

CHAPTER 3

Global Proteomic Profiling Highlights Modulated Kinases in IAV Infection

In an orthogonal proteomic approach to mapping PPI networks, we performed global protein abundance (AB) and phosphorylation (PH) profiling of primary NHBE and differentiated THP-1 cells infected with pH1N1, H3N2, or H5N1 IAV to identify host pathways and kinases that are modulated during IAV infection (**Figure 3.1A**). Cells were mock infected or infected with pH1N1, H3N2 or H5N1 at MOI 3, harvested at four time points post-infection (3hr, 6hr, 12hr, and 18hr) and processed for protein identification and quantification as well as phosphopeptide enrichment. Peptide samples were analyzed by MS, searched by MaxQuant, and protein abundance and site-specific phosphorylation quantified using MSStats (**Table S3.1**). We identified hundreds of significantly changing abundant proteins and phosphorylation events for each of the three strains in both cell types across the time points (**Figure 3.1B-C, Table S3.1**). We also detected increasing protein abundance of IAV proteins over the time course of infection, indicating productive infection across the collected time points (**Figure 3.1D**). However, viral protein abundance was variable between the IAV strains at some time points, especially at 12 hours in THP-1 cells (**Figure 3.1D**). We therefore chose a single time point with high viral protein abundance to compare the IAV strains at their peak infection in downstream analyses. Virus protein abundance was highest at 18 hours post-infection for pH1N1 and H3N2, and reached comparable levels at 12 hours post-infection for H5N1, therefore these time points were selected for all subsequent analyses (**Figure 3.1D**). While moderate overlap was observed between the three strains, the majority of phosphorylation events are strain-specific, which may indicate unique phosphorylation signatures and re-wiring of host pathways during infection (**Figure S3.1A**). Interestingly, the seasonal circulating IAV strains (pH1N1 and H3N2) share a larger overlap of changing phosphorylation events with each other than with avian-derived H5N1 (**Figure S3.1A**). Significantly changing phosphorylation events across all virus strains were observed in proteins enriched for RNA splicing and processing, cellular and nuclear membranes, regulation of gene silencing, and innate immune response (**Figure S3.1B, Table S3.1**). These statistically significant enrichments are consistent with IAV infection events for co-

opting host RNA machinery to generate, splice and translate viral RNA transcripts and proteins, for virus entry, fusion and exit, for viral RNA export from the nucleus and blocking host mRNA export from the nucleus, and for cellular detection and response to virus (Dou et al., 2018; Klemm et al., 2018).

Protein phosphorylation changes reflect changes in kinase activities and highlight pathways that are regulated by IAV. We next predicted changes in kinase activities during IAV infection from our phosphorylation data. First, to determine if phosphorylation changes were biased by changes in protein levels, we measured the correlation between protein and phosphosite abundance changes for all instances where both protein and phosphorylation could be measured. Each site is represented individually or as a combination of phosphorylated sites when multiple phosphorylations were observed within single peptides. We observed a weak correlation, suggesting that the observed phosphorylation changes were largely not driven by underlying changes in protein abundance (**Figure 3.1E**, **Figure S3.1C**). Next, we predicted changes in kinase activity based on substrate proteins with significantly changing phosphorylation sites in our study (**Table S3.1**). We used a comprehensive catalog to map kinase-substrate relationships (Türei et al., 2021) and set scoring criteria to increase confidence of kinase activity annotations (**Methods**). From this, we identified 13 kinases with significantly changing activity (**Figure 3.1F**). Kinases with activity changes during IAV infection include five mitogen-activated protein kinase (MAPK) family members (MAP2K3, MAP2K6, MAPKAPK2, MAPKAPK3, MAPKAPK5), two ribosomal protein S6 kinase (RPS6K) family members (RPS6KB1, RPS6KB2), and one member of the phosphatidylinositol 3-kinase-related kinase family (PRKDC). In NHBE and THP-1 cells, MAPK family members show decreased activity or no significant change during pH1N1 infection, compared to increased activity during H3N2 and H5N1 infection. Interestingly, this trend is also observed for RPS6K members, although the functional significance is unclear. In THP-1 cells, PRKDC shows increased activity during

pH1N1 and H3N2 infection, and no significant change during H5N1 infection. This may indicate a macrophage-specific response via PRKDC with the predominant human-infecting IAV strains. Collectively, these predictions identify differential kinase activity patterns during infection with the three IAV strains, and may be indicative of the different strain pathogenicities and host responses.

Overlaying PPI and phosphoproteomics results identified 45 human proteins with significantly changing phosphorylation sites upon infection that also interact with 10 IAV proteins (**Figure 3.1G**). For some interacting human proteins, the phosphoregulation pattern is consistent across all three strains. For example, CANX is an HA interactor that is phosphorylated at serine 583 (S583). In both THP-1 and NHBE, CANX S583 is downregulated by all three IAV strains. SRSF2, a PA-X interactor, is universally upregulated at S208 by all three IAV strains. These examples may be representative of PPIs with pan-strain functionality in IAV infection and replication, and host response. For other IAV-interacting proteins, phosphorylation is differentially regulated by specific IAV strains. One example is the cleavage and polyadenylation specificity factor CPSF4, a well-known NS1 interactor that blocks nuclear export of host pre-mRNA and post-transcriptionally inhibits the production of interferon-stimulated genes as part of NS1-mediated host cell shutoff (Hale et al., 2010; Kainov et al., 2011; Nemeroff et al., 1998; Noah et al., 2003). Here, we show that CPSF4 S200 phosphorylation is regulated in a strain-specific manner, with decreased phosphorylation during pH1N1 and H3N2 infection and increased phosphorylation during H5N1 infection. Strain-specific differences in the functionality of CPSF4-NS1 interaction have been reported, namely pH1N1 NS1 is unable to block mRNA export and stimulate mRNA translation as efficiently as H5N1 subtype IAV (Hale et al., 2010; Kainov et al., 2011). The phosphorylation patterns observed may be a result of strain-specific regulation of virus-human interactions, human protein localization or function.

While we observe only one or two sites with increased or decreased phosphorylation for most human proteins in this data set, five IAV-interacting proteins have four or more sites regulated during infection. The highest number of sites with significantly changing phosphorylation include HSPB1 (PB1-F2), PRKDC (M2) and AHANK (NEP). PRKDC is a DNA-damage sensing protein kinase identified as an M2 PPI with five significantly changing phosphorylation sites during infection (**Figure 3.1G**). PRKDC is also identified in our study as a kinase with increased predicted activity upon pH1N1 and H3N2, but not H5N1, infection in THP-1 cells (**Figure 3.1F**). The five identified phosphorylation sites are almost all universally upregulated in phosphorylation with pH1N1, H3N2 and H5N1 infection (**Figure 3.1G**). AHNAK is a large (700 kDa) scaffold protein involved in diverse cellular processes including calcium signaling, cell-cell contact formation, cytoskeletal and membrane architecture and T-cell function (Benaud et al., 2004; Matza et al., 2008, 2009). It interacts with NEP, and among its 11 sites of phosphorylation changes, one site is universally upregulated across the three strains, four sites are universally downregulated across the three strains, and six sites show strain-specific patterns of phosphorylation changes (**Figure 3.1G**). The phosphoregulation of PRKDC and AHNAK PPIs may suggest these are highly regulated nodes in IAV infection. Collectively, the additional layer of phosphoregulation during IAV infection for these IAV-human PPIs may highlight increased functional importance of the interaction in IAV infection.

Methods

Viruses. IAV isolates A/California/04/2009 H1N1, A/Wyoming/03/2003 H3N2 and A/Vietnam/1203/2004 H5N1 HALo were obtained through BEI Resources (NIAID, NIH). A/Vietnam/1203/2004 H5N1 HALo was engineered to contain a deletion in the HA polybasic cleavage site (Park et al., 2006) and allows its use in Biosafety Level 2+ facilities. All IAV viruses were propagated in embryonated chicken eggs (Charles River Laboratories) following methods previously described (Eisfeld et al., 2014). Virus stocks were titrated in Madin-Darby canine kidney (MDCK) cells (ATCC, CCL-34) by plaque assay. All infections with live IAV were performed in accordance with institutional Biosafety Level 2+ biosafety procedures at the Icahn School of Medicine at Mount Sinai and the J. David Gladstone Institutes.

Cell infections for global proteomic analysis. NHBE cells were seeded at 1×10^7 cells per collagen I-coated 15cm dish and cultured in BEBM media with nine BEGM supplemental singlequots (described in **Chapter 2 Methods**). THP-1 cells were expanded in suspension in T75 flasks at a density of 2×10^5 - 8×10^5 cells/mL and cultured in RPMI-1640 with L-glutamine supplemented with 10% FBS, gentamicin (Thermo Scientific, 15750060) at final concentration 50 μ g/mL and 1X Pen/Strep. For plating, THP-1 cells were pelleted at 500 x g for 5 minutes, resuspended in growth media supplemented with PMA (Fisher, BP685-1) at final concentration 10ng/mL to induce differentiation, and subsequently seeded at 2×10^7 cells per 15cm dish. THP-1 cells were differentiated for 72 hours in PMA media, before media was exchanged with growth media (no PMA) for 24 hours to reduce PMA-activated pro-inflammatory response. For infection, cell growth media was removed, and cells were either mock infected or infected in biological duplicate with A/California/04/2009 H1N1 IAV, A/Wyoming/03/2003 H3N2 IAV or A/Vietnam/1203/2004 H5N1 IAV at MOI 2 in 0.5% BSA in 1X PBS with magnesium and calcium. Cells were incubated in virus inoculum at 37°C for 1 hour. After absorption, virus inoculum was aspirated and replaced with cell growth media supplemented with TPCK-trypsin

(Sigma-Aldrich, T8802). Cells were returned to incubate at 37°C before cell harvest and global proteomics sample preparation and processing.

Global proteomics sample preparation. IAV-infected cells were harvested and lysed at 3 hours, 6 hours, 12 hours and 18 hours post-infection in biological duplicate with time point-matched mocks for each IAV strain. At the indicated time point, cells were washed with 1X PBS and lysed in 2mL urea lysis buffer (8M urea, 100mM Tris pH 8.0, 150mM NaCl) supplemented with Complete mini EDTA-free protease inhibitor (Roche, 11836153001) and PhosSTOP phosphatase inhibitor (Roche, 04906837001). Cells were harvested in lysis buffer by cell scraper (Fisher 50-809-263), collected in 15mL Falcon tubes (Fisher, 14-959-53A) and incubated on ice for 30 minutes. Samples were subsequently snap-frozen in liquid nitrogen and stored at -80°C until probe sonication. Samples were thawed on ice and subjected to three rounds of probe sonication (Fisherbrand™ Model 505 Sonic Dismembrator) at 20% amplitude for 20 seconds followed by 10 seconds of rest on ice. Protein concentration was then determined by Bradford assay (Sigma, B6916). Protein from clarified lysate was reduced with 4mM tris(2-carboxyethyl)phosphine (Sigma, C4706) for 30 minutes at room temperature, and alkylated with iodoacetamide at final concentration 10mM for 30 minutes at room temperature in the dark. Iodoacetamide was quenched by addition of DTT at final concentration 10mM and incubation in the dark at room temperature for 30 minutes. For digestion, samples were then diluted with 0.1M ammonium bicarbonate pH 8.0 to a final concentration of 2M urea. Sequencing-grade trypsin (Promega, V5111) was added at a 1:100 (enzyme:protein w:w) ratio and incubated overnight at 37°C. Following digestion, 10% trifluoroacetic acid was added to acidify each sample to a final pH ~2. Samples were desalted by vacuum manifold (Thermo Fisher Scientific) using Sep Pak tC18 cartridges (Waters, WAT054955) and HPLC-grade reagents. Each cartridge was activated with 1mL 80% acetonitrile, 0.1% trifluoroacetic acid, and equilibrated three times with 1mL 0.1% trifluoroacetic acid. Samples were loaded onto C18

cartridges, and peptide-bound cartridges were washed four times with 1mL 0.1% trifluoroacetic acid. Samples were then eluted four times with 0.5mL 50% acetonitrile, 0.25% formic acid to maximize peptide recovery. 10µg of each sample was reserved for global protein abundance MS data acquisition, and the remainder (at least 1mg) was allocated to phosphopeptide enrichment. All samples were lyophilized by vacuum centrifugation (CentriVap Cold Trap, Labconco).

Phosphopeptide enrichment. For phosphopeptide enrichment, iron nitriloacetic acid (NTA) agarose resin was prepared in-house from 50% nickel NTA (Ni-NTA) Superflow bead slurry (Qiagen, 30210). 30µL per sample of 50% Ni-NTA Superflow bead slurry was added to a 2mL bio-spin column (Bio-Rad, 732-6204). Beads were stripped of nickel ions by four 30-second incubations with 500µL 100mM EDTA. Beads were conditioned and loaded with iron by two washes with 500µL H₂O, four 1-minute incubations with 500µL 100mM FeCl₃, three washes with 500µL H₂O, and one wash with 500µL 0.5% formic acid to remove residual iron. Beads were resuspended in 600µL H₂O, and 60µL was aliquoted into a C18 NEST column (Fisher, NC0484000) that was equilibrated with 150µL of 80% acetonitrile, 0.1% trifluoroacetic acid. 1mg of digested, dried peptides were resuspended in 75% acetonitrile, 0.15% trifluoroacetic acid. Peptides were incubated with the beads for 2 minutes, mixed by pipetting and incubated again for 2 minutes. Beads were washed four times with 200µL 80% acetonitrile, 0.1% TFA, followed by three washes with 200µL 0.5% formic acid. Beads were then incubated twice with 200µL 500mM potassium phosphate buffer pH 7 for 15 seconds, and twice with 200µL 0.5% formic acid for 15 seconds. Phosphopeptides were eluted twice to maximize recovery with 75µL 50% acetonitrile, 0.25% formic acid by centrifugation at 3000 rpm for 30 seconds, and lyophilized by vacuum centrifugation (CentriVap Cold Trap, Labconco).

Global phosphorylation and abundance MS data acquisition and analysis. Global abundance (AB) and phosphorylation (PH) MS samples were collected on three instruments following instrument-specific LC and MS acquisition parameters (**Table S3.2**). Samples acquired on an Orbitrap Fusion Tribrid mass spectrometer (Thermo Fisher Scientific) include: (1) NHBE abundance data for pH1N1, H3N2 and H5N1; (2) NHBE phosphorylation data for pH1N1 and H3N2; and (3) THP-1 abundance data for pH1N1, H3N2 and H5N1. Samples acquired on an Orbitrap Elite Hybrid Mass Spectrometer (Thermo Fisher Scientific) include: NHBE phosphorylation data for H5N1. Samples acquired on an Orbitrap Fusion Lumos Tribrid mass spectrometer (Thermo Fisher Scientific) include: THP-1 phosphorylation data for pH1N1, H3N2 and H5N1.

For samples acquired on the Orbitrap Fusion Tribrid, digested, desalted and dried peptides were resuspended in 10 μ L 0.1% TFA (AB samples) or 15 μ L of 0.1% TFA (PH samples). 2 μ L of each sample were injected in technical duplicate (samples from NHBE cells) or technical singlet (samples from THP-1 cells) on an Easy-nLC 1000 (Thermo Fisher Scientific) coupled to an Orbitrap Fusion Tribrid mass spectrometer (Thermo Fisher Scientific). Briefly, peptides were separated on a 75 μ m x 25cm fused silica IntegraFrit capillary packed with 1.9 μ m Reprosil-Pur C18 AQ reversed-phase resin (Dr. Maisch GMBH, r119.aq) over a 180min gradient at a flow rate of 300 nL/minute as described in **Table S3.2**. Buffer A consisted of 0.1% formic acid (FA) in water, and buffer B was 0.1% FA in acetonitrile. Spectra were continuously acquired in a data-dependent manner. One full scan in the Orbitrap (400-1600 m/z at 120,000 resolution with an AGC target of 2×10^5 and maximum injection time of 100 milliseconds) was followed by as many MS/MS scans as could be acquired on the most abundant ions in 3 seconds in the dual linear ion trap (HCD collision energy of 30%, AGC target of 1×10^4 , maximum injection time of 35 milliseconds, and isolation window of 1.6 m/z). Singly and unassigned charge states were rejected. Dynamic exclusion was enabled after n=1 time, with an exclusion duration of 40

seconds (tolerance of ± 10 ppm). Detailed MS acquisition parameters are reported in **Table S3.2**.

For samples acquired on an Orbitrap Elite Hybrid Mass Spectrometer, digested, desalted and dried peptides were resuspended in 10 μ L 0.1% TFA (AB samples) or 15 μ L of 0.1% TFA (PH samples). 2 μ L of each sample were injected in technical duplicate on an Easy-nLC 1000 (Thermo Fisher Scientific) coupled to a Orbitrap Elite Hybrid Mass Spectrometer (Thermo Fisher Scientific). Briefly, peptides were separated on a 75 μ m x 25cm fused silica IntegraFrit capillary packed with 1.9 μ m Reprosil-Pur C18 AQ reversed-phase resin (Dr. Maisch GMBH, r119.aq) over a 240min gradient at a flow rate of 300nL/minute as described in **Table S3.2**. Buffer A consisted of 0.1% formic acid (FA) in water, and buffer B was 0.1% FA in acetonitrile. Spectra were continuously acquired in a data-dependent manner. For each cycle, one full scan in the Orbitrap (200-2000 m/z, at 120,000 resolution with an AGC target of 1×10^6 and maximum injection time of 100 milliseconds) was followed by 20 MS/MS scans acquired in the linear ion trap (AGC target of 3×10^4 , maximum injection time of 50ms, fragmented by normalized collision energy at 35%). Singly and unassigned charge states were rejected. Dynamic exclusion was enabled with a repeat count of 1, an exclusion duration of 20 seconds (tolerance of ± 10 ppm). Detailed MS acquisition parameters are reported in **Table S3.2**.

For samples acquired on the Orbitrap Fusion Lumos Tribrid, digested, desalted and dried peptides were resuspended in 15 μ L of 4% formic acid, 3% acetonitrile. 2 μ L of each sample were injected in technical singlet onto an Easy-nLC 1200 (Thermo Fisher Scientific) interfaced via a nanoelectrospray source (Nanospray Flex) coupled to an Orbitrap Fusion Lumos Tribrid mass spectrometer (Thermo Fisher Scientific). Briefly, peptides were separated on a C18 reverse phase column (75 μ m x 25cm packed with 1.9 μ m Reprosil-Pur C18 AQ reversed-phase resin) over the course of a 180 minute data acquisition as described in **Table S3.2**. Buffer A

consisted of 0.1% formic acid (FA) in water, and buffer B was 0.1% FA in acetonitrile. Spectra were continuously acquired in a data-dependent manner. One full scan in the Orbitrap (at 120,000 resolution in profile mode with an AGC target of 2×10^5 and maximum injection time of 100 milliseconds) was followed by as many MS/MS scans as could be acquired on the most abundant ions in 3 seconds in the dual linear ion trap (rapid scan type with an intensity threshold of 5000, HCD collision energy of 30%, AGC target of 1×10^4 , maximum injection time of 35 milliseconds, and isolation width of 1.6 m/z). Singly and unassigned charge states were rejected. Dynamic exclusion was enabled with a repeat count of 1, an exclusion duration of 30 seconds, and an exclusion mass width of ± 10 ppm. Detailed MS acquisition parameters are reported in **Table S3.2**.

Raw MS files from IAV infection time course samples were grouped separately by cell line, enrichment (abundance vs phosphorylation), and instrument, and searched simultaneously within each group using MaxQuant (version 1.6.1.0) (Cox and Mann, 2008). MS/MS spectra were searched against the human proteome (SwissProt human canonical sequences, downloaded 09 October 2018) and IAV protein sequences. Trypsin (KR|P) was selected to allow up to two missed cleavages. Variable modifications were assigned for: N-terminal protein acetylation, N-terminal protein methionine oxidation, and phosphorylation of serine, threonine, and tyrosine (the latter for phosphorylation enrichment samples only). One static modification was assigned for carbamidomethyl cysteine. LFQ was enabled. Match between runs was enabled with a 1.5min matching time window and 20min alignment window. All other MaxQuant settings were left at the default.

Peptide ion intensities from the output of MaxQuant were summarized to protein intensities using the R Bioconductor package MSstats (version 3.19.4) (Choi et al., 2014), specifically the function `dataProcess`, with default settings except that the noise-filtering (Tsai et al., 2020) was

turned on by setting `featureSubset = "highQuality"` and `remove_uninformative_feature_outlier = TRUE`. For phosphopeptide data, the peptide ion intensities were similarly summarized to a single intensity per unique observed single-peptide combination of phosphorylated sites by relabeling the protein of each feature as the combination of protein name and observed phosphorylated sites. The Bioconductor package `artMS` (version 1.3.9) (doi: 10.18129/B9.bioc.artMS) was used for this relabeling. The differences in log₂-transformed intensity between infected and mock samples were scored using the `MSstats` function `groupComparison`, which fits a single linear model for each protein with a single categorical variable for condition. From these models, `MSstats` reports pairwise differences in means between conditions as log₂FC with a p-value based on a t-test assuming equal variance across all conditions, and reports adjusted p-values using the false discovery rate (FDR) estimated by the Benjamini-Hochberg procedure. One single time point per virus was selected for both cell types based on high viral protein abundance in the abundance data: at 18 hours post-infection for pH1N1 and H3N2, and 12 hours post-infection for H5N1. To determine significant changes in protein abundance and phosphorylation, selection criteria included: (1) adjusted p-value < 0.05; and (2) $|\text{absolute}(\log_2\text{FC})| > 1$ (**Table S3.1**).

Computational analyses methods

Data and Code Availability. At the time of dissertation submission, mass spectrometry metadata for abundance and phosphorylation data are in the process of being deposited to the ProteomeXchange Consortium via the PRIDE partner repository (Perez-Riverol et al., 2019). R package source materials for `MiST` and `Mass Spectrometry Statistics and Quantification` (`MSstats`, version 3) are publicly available through the Krogan Lab GitHub: <https://github.com/kroganlab>. Further information on `MiST` scoring can be found on the Krogan Lab GitHub: <https://github.com/kroganlab/mist>.

Gene Ontology (GO) enrichments. For PH GO enrichments, proteins with significantly up- and down-regulated phosphorylation events (defined as adjusted p-value < 0.05, absolute(log2FC) > 1, and observed in infected and mock samples) of each virus strain were collated at 18 hours post-infection (pH1N1, H3N2) and at 12 hours post-infection (H5N1) across all cell types, and tested for enrichment of GO terms from among all three ontologies: Biological Process, Molecular Function and Cellular Component. The over-representation analysis was performed using the enricher function of clusterProfiler package (version 3.12.0) in R with default parameters. GO terms were obtained from the R annotation package org.Hs.eg.db (version 3.12.0). Significant terms were defined as those with adjusted p-value < 0.05. We selected a set of non-redundant terms following an automated clustering procedure. We first constructed a term tree based on distances (1-Jaccard Similarity Coefficients of shared genes in KEGG or GO) between the significant terms. The term tree was cut at a specific level ($h = 0.99$) to identify clusters of non-redundant gene sets. For results with multiple significant terms belonging to the same cluster, we selected the most significant term (i.e. lowest adjusted p-value) (**Table S3.1**).

Network visualizations. All networks were generated and visualized in Cytoscape (version 3.8.2) (Shannon et al., 2003). For the PPI-phosphorylation overlay network, proteins were selected and visualized if they were identified in the PPI data above MiST scoring thresholds and in the phosphorylation data at the restricted time points (18 hours post-infection with pH1N1 and H3N2; 12 hours post-infection with H5N1) with an absolute(log2FC) > 1 and adjusted p-value < 0.05 in any cell type. If a site was detected across multiple cell lines, the maximum absolute value, non-infinite fold-change was used.

FIGURES AND LEGENDS

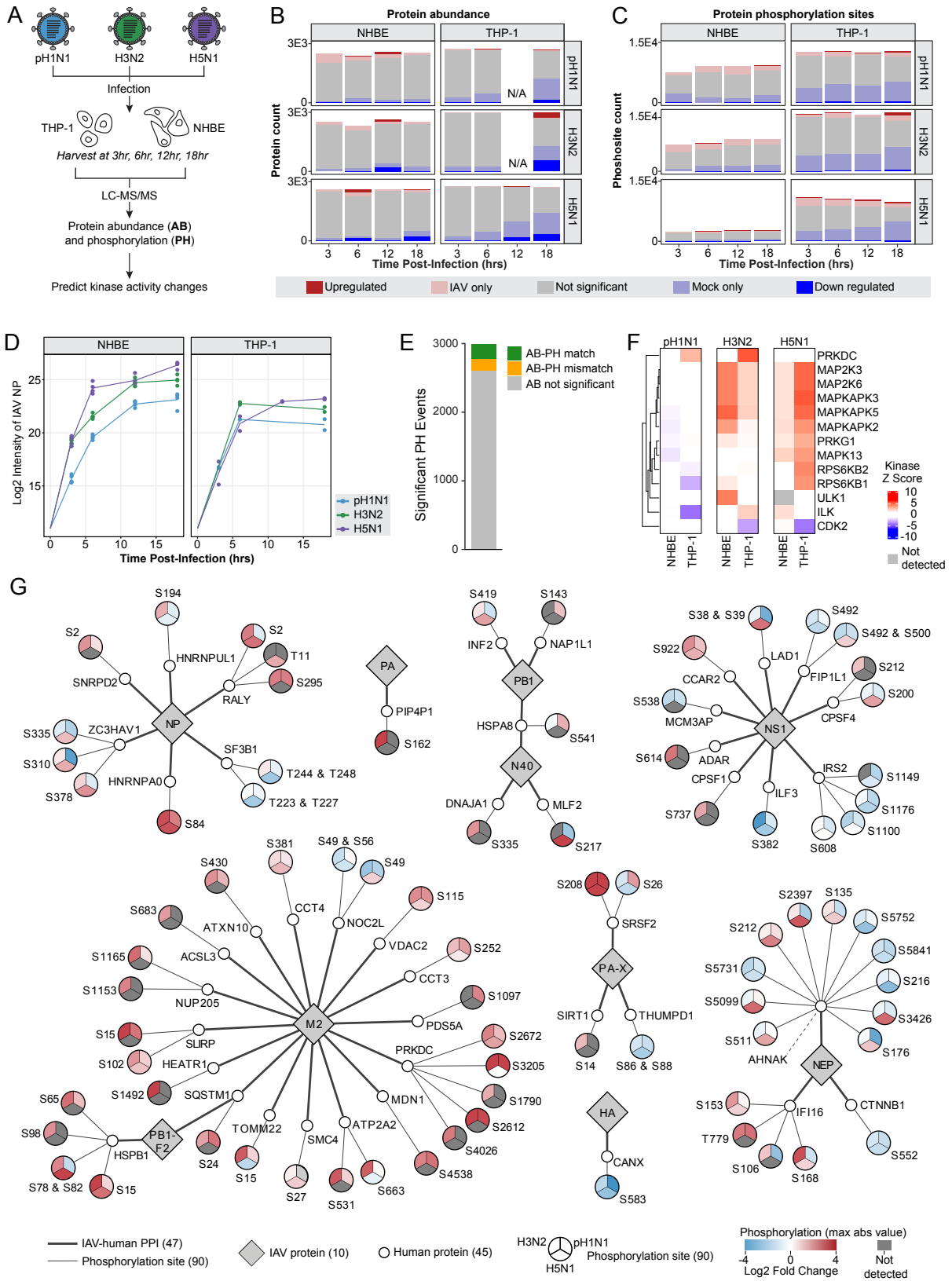


Figure 3.1 Global proteomic profiling highlights modulated kinases in IAV infection. (A) Strategy for *ex vivo* global proteomic profiling with IAV infection. NHBE and PMA-differentiated THP-1 cells were mock-infected or infected with pH1N1, H3N2 or H5N1 IAV. Samples were harvested at four time points post-infection with time-matched mocks, processed for global abundance (AB) and phosphorylation (PH), and analyzed by mass spectrometry (LC-MS/MS). Significant changes in AB and PH were quantified, and PH data was then used to predict kinases with modulated activity during infection. (B) Bar chart plotting the total number of proteins quantified in the AB dataset at each time point with pH1N1, H3N2 or H5N1 IAV infection in THP-1 and NHBE cells. Total includes proteins that significantly increase in abundance (red), significantly decrease in abundance (blue) and do not significantly change in abundance (grey). Proteins identified only in IAV-infected samples or mock-infected samples are also shown. Totals are not available (N/A) for pH1N1 and H3N2 IAV at the 12 hour time point in THP-1 cells, as these samples did not pass MS quality control. (C) Bar chart plotting the total number of phosphorylation sites quantified in the PH dataset at each time point with pH1N1, H3N2 or H5N1 IAV infection in THP-1 and NHBE cells. Total includes the number of sites that significantly increase in phosphorylation (red), significantly decrease in phosphorylation (blue) and do not significantly change in phosphorylation (grey). Phosphosites identified in only IAV-infected samples or mock-infected samples are also shown. (D) Log₂ intensity of virus protein abundance (Log₂ Intensity) for IAV NP protein detected over a time course of pH1N1, H3N2 and H5N1 infection in NHBE and THP-1 cells. Data points are not shown for pH1N1 and H3N2 IAV at the 12 hour time point in THP-1 cells, as these samples did not pass MS quality control. (E) Correlation of the AB and PH data. Phosphorylation events that are significantly correlated (AB-PH match; green), significantly anti-correlated (AB-PH mismatch; yellow), or not correlated (AB not significant; grey) with changes in protein AB are shown. Data is taken at 18 hours (pH1N1, H3N2) and 12 hours (H5N1) post-infection, and represented as a total collective across all virus strains and cell types. (F) Heatmap of kinase activity predictions from the phosphorylation data with pH1N1, H3N2 and H5N1 infection in both cell types at 18 hours post-infection (pH1N1, H3N2) and 12 hours post-infection (H5N1) with FDR < 0.05 and at least two known phosphorylation sites detected in the global phosphoproteomics dataset per kinase. Increased kinase activity is shown in red, and decreased kinase activity is shown in blue (kinase Z score); kinases that were not detected are shown in grey. (G) Map of IAV-human PPIs including 45 human proteins (small white circles) that interact with 10 IAV proteins (grey diamonds) and possess significantly changing phosphorylation sites (adjusted p-value < 0.05) at 18 hours post-infection (pH1N1, H3N2) and 12 hours post-infection (H5N1). Significantly changing phosphorylation sites on each human protein (emanating large circular nodes) are stratified by IAV strain (pie sections) and colored by the maximum log₂ fold change in phosphorylation compared to mock-infected controls (increased phosphorylation in red; decreased phosphorylation in blue). If a site was detected across multiple cell lines, the maximum absolute value, non-infinite fold-change was used. Dark gray color indicates the site was not detected. Phosphorylation sites are labeled by amino acid abbreviation (Serine S, Threonine T, Tyrosine Y) and position. IAV-human PPIs are represented by dark grey lines, and edges to phosphorylation site nodes are represented by lighter grey lines.

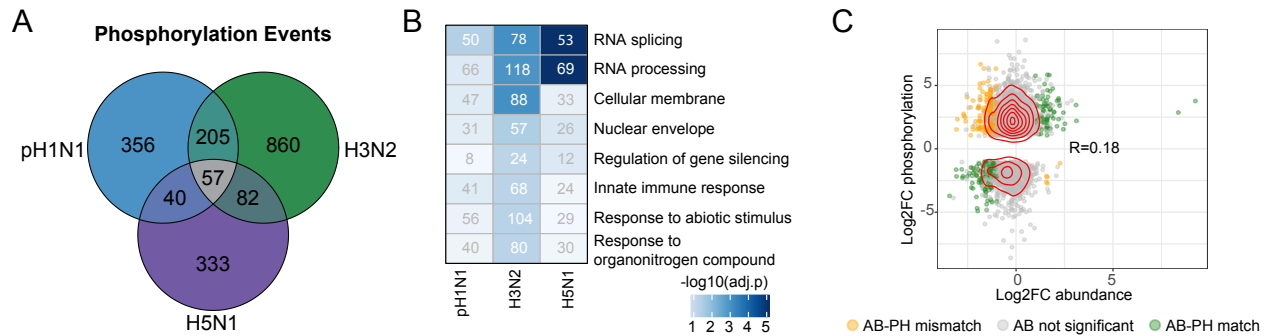


Figure S3.1 Strain-specific and shared phosphorylation sites, phosphorylation GO enrichments and AB and PH dataset correlation, Related to Figure 3.1. (A) Venn diagram of the total number of significantly changing phosphorylation events at 18 hours post-infection with pH1N1 and H3N2, and 12 hours post-infection with H5N1, collapsed across both cell types. (B) Heatmap of GO enrichments of the phosphorylation data at 18 hours post-infection with pH1N1 and H3N2, and 12 hours post-infection with H5N1, collapsed across cell types. Increasing shading intensity reflects increasing significance of the enrichment term. Significant GO terms were defined as those with adjusted p-value < 0.05, and non-redundant terms were selected by automated clustering procedure (see also **Methods**). The number of proteins per enriched cluster are shown in white if significant (adjusted p-value < 0.05), and grey if not significant (adjusted p-value > 0.05). (C) Scatterplot of proteins with log₂ fold changes in protein abundance (x-axis) and log₂ fold changes in phosphorylation (y-axis), showing significant but weak correlation (R=0.18). Data points are colored as in **Figure 3.1E**, with changes in phosphorylation significantly correlated (AB-PH match; green), significantly anti-correlated (AB-PH mismatch; yellow) or not correlated (AB not significant; grey) with changes in protein abundance.

SUPPLEMENTAL TABLES

Table S3.1 Global protein abundance and phosphorylation data, phosphorylation GO enrichments and predicted kinase activities, Related to Figures 3.1 and S3.1. Full list of global protein abundance measurements (AB_Full tab), list of significant protein abundance measurements (AB_Sig tab), full list of phosphorylation site measurements (PH_Full tab), and list of significant phosphorylation site measurements (PH_Sig tab) with pH1N1, H3N2 and H5N1 IAV infection in NHBE and THP-1 cells. All tabs report the log₂ fold change in protein abundance and phosphorylation at the specified site, as well as adjusted p-value. Full lists report measurements from all time points (3hr, 6hr, 12hr, 18hr). Significant lists report measurements at 18 hours post-infection with pH1N1 and H3N2, and at 12 hours post-infection with H5N1, with selection criteria of: (1) adjusted p-value < 0.05; and (2) absolute(log₂FC) > 1 (see also **Methods**). Empty data cells represent no protein detected at the indicated time point, IAV strain or cell type. Column descriptions for all AB and PH tabs are reported (ABPH_Column_Descriptions). GO enrichments for significantly changing phosphorylation sites are reported at 18 hours post-infection with pH1N1 and H3N2, and at 12 hours post-infection with H5N1, in NHBE and THP-1 cells with the full enrichment list (PH_GO_full tab) and with heatmap selection criteria of adjusted p-value < 0.05 and automated clustering to select non-redundant terms (see also **Methods**) (PH_GO_selection tab). Column descriptions for GO lists are provided (GO_List_Column_Descriptions tab). Finally, a full list of predicted kinase activities at each time point post-infection with pH1N1, H3N2 or H5N1 in NHBE and THP-1 cells is reported (Predicted_Kinase_Activity tab). Column descriptions for Kinase Activity are provided (KinaseActivity_Column_Description tab). Table is available online only as supplemental material.

Table S3.2 AB and PH liquid chromatography (LC) and mass spectrometry (MS) acquisition parameters, Related to Methods. LC and MS acquisition parameters are reported for the three instruments that acquired AB and PH data in our study. A table summary is included matching each instrument to their respective LC and MS parameters tabs and to the global proteomic data collected on each instrument, including data type, cell type and IAV strain. Table is available online only as supplemental material.

CHAPTER 4

Patient Exome Sequencing Identifies Gene Variants Encoding Proteins that are Regulated in Abundance and Phosphorylation during IAV Infection

To investigate the clinical relevance of our proteomics dataset, we next explored if proteins we found to be regulated *ex vivo* during infection were implicated in patient responses to IAV. We obtained de-identified human samples following informed consent from individuals at five eMERGE study sites and the St. Jude Children's Hospital. We identified 495 individuals of homogeneous European American ancestry inferred by using a clustering approach, of which 161 were hospitalized with severe influenza infection and 334 served as outpatient controls (**Figure 4.1A**). We used ICD9 codes as the phenotypic trait for the analysis. We sequenced the whole exomes of the 495 participants, with 97% of targeted bases covered at a depth of 20x or greater. We identified a total of 3,621,267 variants in 22 million base pairs across the coding regions of 22,621 genes, of which 90% were rare variants (minor allele frequency (MAF) < 1%). There was no evidence of site-specific effects or other systematic biases in the analysis of the filtered data (**Methods**).

We first analyzed predicted loss-of-function (pLOF) variants from the patient dataset to identify potential functional variation in proteins that we identified as IAV-human PPIs, that are regulated in protein abundance (AB) during IAV infection, or that are regulated in protein phosphorylation (PH) during IAV infection. We applied methods suitable to identify nonsynonymous exonic, frameshift substitution, and stop gain/loss exonic variants with MAF < 1% (**Methods**). Because the power to detect singletons is limited by their low frequency, we used a collapsing method by which rare *de novo* mutations that can likely impact protein levels are considered jointly for association analysis. With this approach, we identified five pLOF variants out of 214 PPI genes, 24 pLOF variants out of 3656 AB genes, and 49 pLOF variants out of 3658 PH genes (FDR < 0.05) (**Table S4.1**). From the list of phosphorylation sites identified in our *ex vivo* proteomic data, we then identified pLOF at specific phospho-serine, phospho-threonine, and phospho-tyrosine positions reported in PhosphoSitePlus (Hornbeck et al., 2015) for each of the PPI, AB and PH factors (**Table S4.1, Methods**). We identified phospho-variants in six PPI genes, 75 AB

genes and 146 PH genes (**Table S4.1**). One PPI gene highlighted by both analyses is AHNAK, which was found to contain phosphorylation disruption mutations at serine position 210 (AHNAK_S210), and differed significantly between the hospitalized patients and the control groups (FDR < 0.05) (**Figure 4.1B**, **Table S4.1**). The rare variant discovery power for phosphorylation disrupting mutations was limited when not restricted to pLOF variants.

Hypothesizing that disease outcome may correlate with variations in genes involved in the immune response, we next asked if patient genetic variants involved in immune response are regulated in protein abundance and phosphorylation during IAV infection. We focused on 302 genes that were enriched in the severe disease cohort and involved in immune signaling pathways, specifically in TRIF(TICAM1)-mediated TLR4 signaling, interferon alpha/beta signaling, and ERK/MAPK signaling (**Table S4.1**). We identified an enrichment of rare variants with pLOF at 59 loci that underlie severe influenza disease and other life-threatening viral diseases in previously healthy patients (FDR < 0.05). These 59 loci were enriched for variants that have genetic defects, including pLOF or splice site disruptions (**Table S4.1**). To assess whether these 59 pLOF genes correspond to proteins that change in abundance or phosphorylation during IAV infection, we performed permutation tests (**Methods**). We detected 17/59 and 27/59 genes in the protein abundance and phosphorylation datasets, respectively. 15/17 have significant changes in protein abundance, and 25/27 have significant changes in protein phosphorylation during IAV infection (**Figure 4.1C**, **Table S4.1**). We found the sets of 15/59 (AB) genes and 25/59 (PH) genes represent a statistically significant enrichment in identifying proteins with significant protein abundance and phosphorylation changes during IAV infection compared to randomized gene sets within the 302 inborn error genes (**Figure 4.1C**, see also **Methods**). This suggests that our global proteomics datasets highlight genes that may be implicated in regulating influenza disease severity.

Interestingly, the majority of the 15 abundance proteins, identified as pLOF variants in patients with severe disease, decrease in abundance with pH1N1, H3N2 and H5N1 IAV infection, particularly in THP-1 cells (**Figure 4.1D**). Nine of these proteins (PPP2CA, PPP2R1A, PTPN6, STAT1, UBA7, RIPK2, TAB1, PDE12 and CD14) are involved in cytokine signaling, interleukin signaling and Toll-like receptor (TLR2, TLR4, TLR7, TLR8, TLR9) signaling cascades. These pathways are commonly activated in host cells upon virus detection to restrict virus replication. IAV may downregulate these proteins to suppress host innate immune signaling or modulate host response, particularly in macrophage cells, and to establish infection. In support of this, PP2A, comprised of PPP2CA catalytic and PPP2R1A regulatory subunits, was shown to be required for efficient IAV replication, and acts not by altering immune signaling but rather by modulating cell survival pathways to prolong survival of cells infected with different H1N1-, H3N2- and H5N1-subtyped IAV (Gerlt et al., 2021). STAT1 inactivity due to a tyrosine point mutation that mimics non-phosphorylated state reduced early induction of interferon-stimulated genes (ISGs) during H1N1 IAV infection and resulted in high susceptibility to IAV infection in mouse models (Liu et al., 2021). pLOF variants of these genes in human patients may not allow effective restriction of virus replication and may not allow effective viral clearance, and thus increase disease severity.

From the phosphorylation statistical enrichment, the 25 phosphorylated proteins include 54 phosphorylation sites that significantly changed with pH1N1, H3N2 and H5N1 infection in NHBE and THP-1 cells (**Figure 4.1E**). Differential phosphoregulation patterns emerge between IAV strains and cell types. For example, H3N2 strongly upregulates phosphorylation sites on proteins (e.g. SNW1_224, PML at four sites, SP110_244, STAT1_727, TNFAIP3 at five sites and NCOR1 at two sites) that are involved in NOTCH3 intracellular, NOD-like receptor and JNK signaling in both NHBE and THP-1 cells. In contrast, pH1N1 and H5N1 upregulate phosphorylation on a smaller subset of these proteins, predominantly in THP-1 cells. This may

indicate that H3N2 is less effective at suppressing the innate immune response, making it potentially less severe than pH1N1 and H5N1. Similar phosphoregulation patterns emerge between the three IAV strains as well. For example, a number of phosphorylation sites on proteins were downregulated by at least two of the three strains in THP-1 cells (e.g. NCOR1_1750 and NCOR1_2396, MAP3K1_292 and MAP3K1_923, CREBBP_2063 and TRAF3_29) and could represent immune cell-specific targets of IAV dampening host response to infection. For pH1N1 and H3N2, these similarities converged on genes involved in DDX58/IFIH1-mediated induction of interferon alpha and beta. Collectively, these analyses identify severe influenza disease-associated genes whose protein abundance and phosphorylation are regulated by IAV during infection, and could be potential therapeutic protein targets to improve disease outcome.

Methods

Research subjects. We obtained de-identified human samples following informed consent from individuals at five eMERGE study sites (Cincinnati Children's Hospital Medical Center (CCHMC), Marshfield, Mt Sinai, Northwestern University, and Vanderbilt) and the St. Jude Children's Hospital. We based the diagnosis of IAV infection on established clinical criteria. Approval for human subjects research was obtained from the institutions involved.

Whole-exome capture and DNA sequencing. Exome enrichment was accomplished with the NimbleGen SeqCap EZ Exome+UTR (Roche NimbleGen, version 2) that targets 64 Mb of coding exons and miRNA regions plus 32 Mb untranslated regions (UTRs) for solution-based capture following the manufacturer's protocol. Library preparation was performed with 200ng of genomic DNA using KAPA HyperPlus library kit (Roche, KK8514) using adaptors compatible with Illumina sequencer on the Hamilton STAR automated platform. We performed amplification, pooling, hybridization, washing, and elution according to the manufacturer's instructions. We assessed the libraries for quality with a high sensitivity DNA ScreenTape assay on the 2,200 TapeStation System (Agilent) and quantity with KAPA Library Quantification Kits for Illumina platforms (Kapa Biosystems). The libraries were diluted to 2nM and clustered using an Illumina cBot with a HiSeq 3000/4000 paired-end cluster kit on a patterned flow cell and a HiSeq 3000/4000 SBS kit (300 cycles, Illumina v2.5 reagents) on the HiSeq 4000 sequencing platform.

Data processing. Each individual's whole exome sequencing (WES) data were mapped to the human reference genome (build hg19) using the Burrows-Wheeler Aligner (v0.7) (Li and Durbin, 2009). After marking duplicates using Picard (<http://broadinstitute.github.io/picard/>), the Genome Analysis Toolkit (GATK v3.1) was used to remove duplicates, perform local realignment, and map quality score recalibration to produce a BAM file (DOI:10.1101/201178). Single nucleotide

polymorphism (SNP) calls were made by the HaplotypeCaller v3.4, filtering poor calls by the Variant Quality Score Recalibration (VQSR) filter from GATK (DOI:10.1101/201178). We sorted the aligned reads based on genome position using Picard (<http://broadinstitute.github.io/picard/>) and recalibrated the base quality score using default parameters. Each sample's final gvcf files were streamed to Illumina DRAGEN Bio-IT Platform (v3.1, Illumina), applying the default parameters in the '--vc-enable-gatk-acceleration true' option to identify and remove low-quality variants. We identified 3,621,267 genetic variants from the exome sequencing data after quality control, of which 3,256,844 had minor allele frequency (MAF) < 0.1%.

Gene-based association and phosphorylation site prediction. Using a gene-based association method with various filters applied, we binned together the predicted loss-of-function (pLOF) variants (nonsynonymous exonic, frameshift substitution, and splicing variants) to identify their contributions to disease with good power. Nonsynonymous exonic, frameshift substitution, and splicing variants with MAF < 1% were collected. Variant annotations and pLOF were predicted by ANNOVAR using dbNSFP (Wang et al., 2010). A variant was pLOF if the variant was predicted deleterious from any of the following annotation algorithms: SIFT and SIFT 4G (Vaser et al., 2016), PolyPhen-2 HDIV and PolyPhen-2 HVAR (Adzhubei et al., 2010), likelihood ratio test (LRT), and Mutation Taster (Schwarz et al., 2014). SKAT-O tests (Lee et al., 2012) were applied, adjusting for hospital, age, sex, and top 10 principal components (PCs). False discovery rate (FDR) < 0.05 was applied to identify genes as significant (**Table S4.1**). Each base position was converted to codon coding using Ensembl Variant Effect Predictor (VEP) (McLaren et al., 2016) and RefSeq as reference data. Kinase-specific phosphorylation site prediction was performed on the tested variants from the sets of genes involved (FDR < 0.05). Phospho-serine, phospho-threonine, and phospho-tyrosine sites were predicted using PhosphoSitePlus (Hornbeck et al., 2015). The prediction scores greater than and equal to 0.5

were considered predictive of a protein phosphorylation site. The rare variant discovery power for phosphorylation disrupting mutations was limited when not restricted to pLOF variants.

Global abundance and phosphorylation permutation tests. We first defined the experimental gene set, and compared the overlap between the 59 rare-variant pLOF severe disease-associated genes and the IAV-infectivity global abundance (AB) and phosphorylation (PH) profiling data. 17/59 genes (AB) and 27/59 (PH) genes were detected in our datasets. 15/17 (AB) and 25/27 (PH) showed significant changes in protein abundance or phosphorylation (**Table S4.1**), and were plotted (**Figure 4.1C**, black dots). Significant changes in protein abundance were defined as: (1) limited to one time point at 18 hours post-infection for pH1N1 and H3N2, and at 12 hours post-infection for H5N1; and (2) adjusted p-value < 0.05. Significant changes in protein phosphorylation were defined as: (1) limited to one time point at 18 hours post-infection for pH1N1 and H3N2, and at 12 hours post-infection for H5N1; (2) requiring site detection in at least 3 IAV-infected replicates or 3 mock replicates; and (3) adjusted p-value < 0.05. The additional analysis restriction for phosphorylation sites increases detection reliability and confidence. We next identified a background of "random samples" for the permutation tests. The 59 severe disease pLOF genes were identified from a larger set of 302 inborn error genes. From the set of 302 inborn error genes, we detected 87 proteins in the AB data and 113 proteins in the PH data. Background gene sets were size-matched to experimental gene sets and defined at 17 (AB) and 27 (PH). Randomized sets of 17/87 and 27/113 genes were used as background ("random samples") for AB and PH permutation tests, respectively. Permutation tests were then performed by comparing the experimental sets of significantly changing AB and PH proteins (**Figure 4.1C**, black dots) to 1000 iterations of randomly-selected, size-matched background gene sets ("random samples"), and plotting the number of corresponding proteins with significant changes in protein abundance or phosphorylation from each randomized iteration (**Figure 4.1C**, blue dots). This enabled the calculation of an empirical p-value, which

was defined as the fraction of randomly sampled results that were greater than the true, experimentally-derived result.

FIGURE AND LEGEND

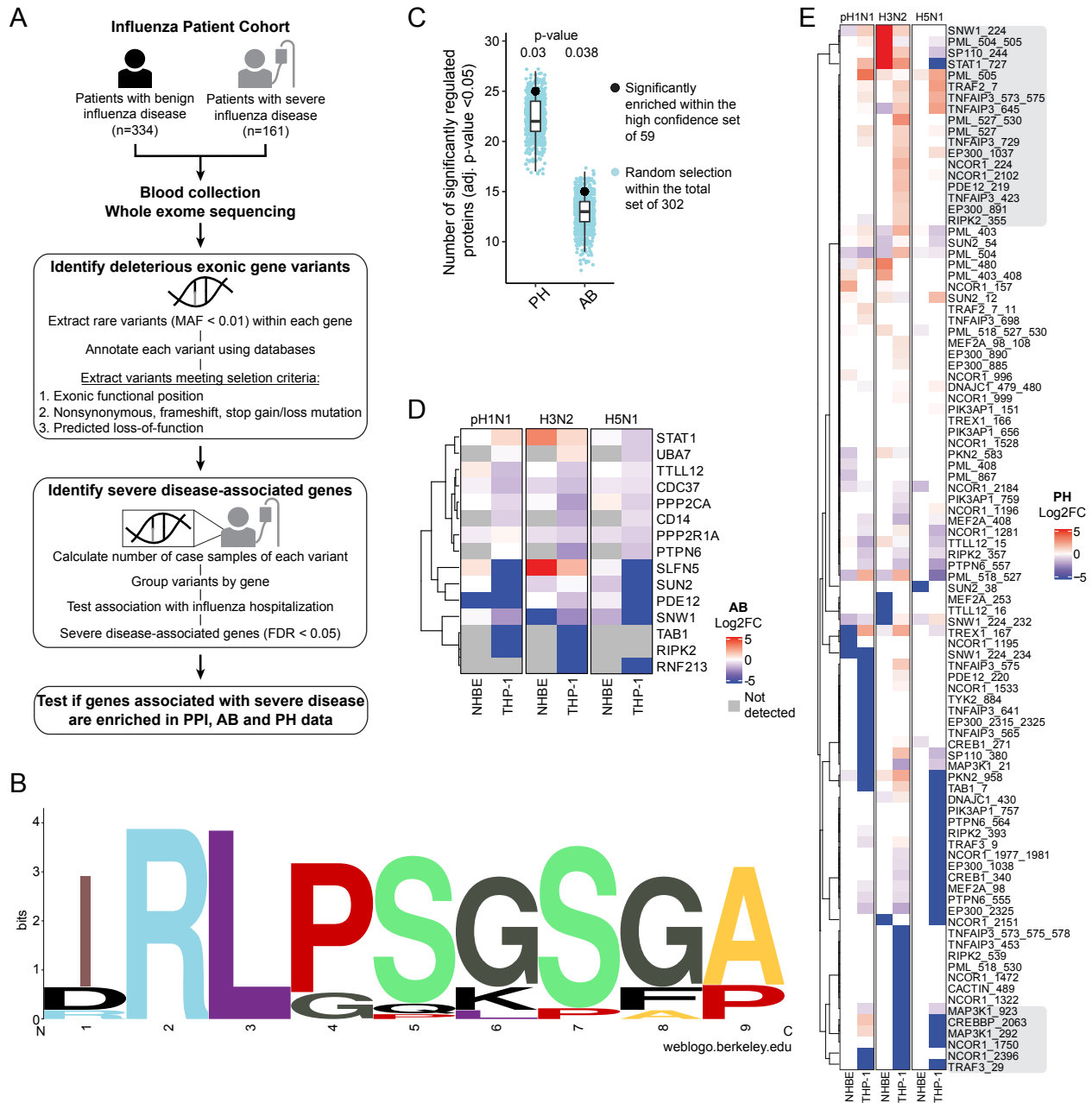


Figure 4.1 Patient exome sequencing identifies gene variants encoding proteins that are regulated in abundance and phosphorylation during IAV infection. (A) Schematic representation of the sample collection and data analysis pipeline for identifying differential mutations in genes of patients associated with severe influenza disease. (B) Sequence LOGO display for phosphorylation disruption mutations found in AHNAK at serine position 210 (AHNAK_S210), using motifs identified by pLOF analysis as likely to be loss of phosphorylation (see also **Methods**). The sequence LOGO visualizes the results of a multiple sequence alignment encompassing AHNAK_S210P/Q in the middle. The height of each letter stack indicates the sequence conservation at that position, and the height of symbols within the stack indicates the relative frequency of each amino acid at that position. Sequence LOGO was

created using WebLogo 2.8.2 (Crooks et al., 2004). (C) Permutation tests identifying genes associated with severe influenza disease that were significantly changing in global protein abundance (AB) and phosphorylation (PH) during IAV infection. From the set of 59 pLOF severe influenza disease genes, 15 proteins were identified as significantly changing in AB and 25 proteins were identified as significantly changing in PH (black dots). Genes from the 59 pLOF severe influenza disease gene set are significantly enriched compared to 1000 iterations of randomly sampled background (blue dots). Background was determined by selecting size-matched sets of randomized genes within the total set of inborn error genes and plotting the number of proteins from that randomized gene set that significantly changed during infection in AB and PH data (see also **Methods**). (D) Proteins from the AB dataset significantly enriched within the 59 pLOF severe influenza disease genes (black dot in (C), AB tab) in NHBE and THP-1 cells at 18 hours post-infection with pH1N1 and H3N2 IAV infection, and at 12 hours post-infection with H5N1 IAV infection. Log₂ fold change in protein abundance (log₂FC AB) is shown (increased AB in red, decreased AB in blue). Proteins not detected are shown in grey. (E) Proteins and corresponding phosphorylation sites (Protein_AminoAcidSite) from the PH dataset significantly enriched within the 59 pLOF severe influenza disease genes (black dot in (C), PH tab) in NHBE and THP-1 cells at 18 hours post-infection with pH1N1 and H3N2 IAV infection, and at 12 hours post-infection with H5N1 IAV infection. Log₂ fold change in protein phosphorylation (log₂FC PH) is shown (increased PH in red, decreased PH in blue). Grey boxes highlight proteins discussed in the text.

SUPPLEMENTAL TABLE

Table S4.1 Identification of rare gene variants in patients with severe influenza disease and permutation tests with global proteomic profiling data, Related to Figure 4.1.

Association test results between hospitalized and non-hospitalized influenza disease patients with pLOF variants in genes mapping back to PPI factors (PPIgenes_pLOF tab), AB proteins (ABgenes_pLOF tab) and PH proteins (PHgenes_pLOF tab). Genes with phosphorylation disruption mutations in identified pLOF variants that overlapped with phosphorylation sites with significant changes in IAV infection mapping back to PPI factors (PPIgenes_pLOF_and_PHsites_ovlpd tab), AB proteins (ABgenes_pLOF_and_PHsites_ovlpd tab) and PH proteins (PHgenes_pLOF_and_PHsites_ovlpd tab). Association test results between hospitalized patients and non-hospitalized patients identifying inborn error genes related to immunity with pLOF variants extracted (pLOF_in_Inborn_Error_Genes). A detailed mutation test report is included for identifying inborn errors in immune genes in hospitalized patients vs non-hospitalized patients with pLOF variants extracted (pLOF_variants_severe_flu tab). Finally, lists are included for the subsets of 59 pLOF genes in severe influenza disease with significant changes in protein abundance (n=15 proteins) (InbornErrorGenes_AB tab) and protein phosphorylation (n=25 proteins, 54 sites) (InbornErrorGenes_PH tab). Empty cells represent no protein detected at the indicated time point, virus strain or cell type. Table available online only as supplemental material.

CHAPTER 5

siRNA Knockdown Identifies Pro-viral and Antiviral Factors of IAV and SARS-CoV-2 Infection

To identify host proteins with antiviral and pro-viral activity, we adapted an arrayed siRNA screening approach (Dornfeld et al., 2018) in A549 cells to knock down select human proteins from the PPI and phosphorylation (PH) datasets (**Figure 5.1A**). A total of 290 genes were knocked down, and include: (1) 212/214 IAV interacting proteins that were targetable by siRNA; and (2) a panel of 64 kinases (including 12 kinases from **Figure 3.1F**) and 14 phosphorylated proteins (**Table S5.1**). A549 knockdown cells were assayed for cell viability, and infected with Influenza A/WSN/1933 H1N1. Percent infection was quantified by immunostaining for viral protein NP and measuring percent NP-positive (%NP+) cells by flow cytometry. Log₂ fold changes in IAV infection were calculated by normalizing %NP+ cells for experimental siRNA against the mean of multiple non-targeting (NT) control siRNA per replicate. Cell viability staining shows siRNA knockdown cells were above 92% viable (**Table S5.1**). Since siRNA knockdown alone did not meaningfully reduce cell viability, we next asked if cell viability resulting from synthetic lethality of siRNA knockdown and IAV infection biased the log₂ fold changes in IAV infection. Increased or decreased IAV infection was not correlated with increased or decreased viability of cells with siRNA knockdown and IAV infection (**Figure 5.1B**, **Table S5.1**), therefore no gene knockdowns were removed from analysis due to toxicity. We performed the assay in biological duplicate, with the two replicates showing a correlation $R^2 = 0.78$ for log₂ fold change in IAV infection (**Figure 5.1C**). As expected, NT control siRNA did not affect IAV infection (black dots, **Figure 5.1C**), and IAV NP-targeting siRNA inhibited IAV infection (green dots, **Figure 5.1C**).

We classified pro-viral and antiviral factors using a threshold log₂ fold change of ≤ -2 or ≥ 2 , respectively, for the IAV PPI and PH screens (**Figure 5.1D-E**, **Table S5.1**). Using this cutoff, for the PPI screen, we classified 44 genes as regulators of IAV infection (**Figure 5.1D**). 37 were classified as pro-viral and seven were classified as antiviral factors (**Figure 5.1D**). These 44 functional proteins interact with 12 IAV proteins, corresponding to at least one functional

interaction per IAV protein. In comparison to previous genome-wide siRNA knockdown studies (Brass et al., 2009; Karlas et al., 2010; König et al., 2010; Ward et al., 2012), we identify 37 novel human proteins that functionally affect IAV infection. Whereas these studies achieve a <2% hit rate for identifying genes that functionally affect IAV infection, our AP-MS-based strategy achieves a 20.6% hit rate for identifying functional nodes and represents a notably higher hit rate. This is consistent with previous findings that genetic screens based on PPI data show ten-fold higher hit rates for identifying functional factors of infection by IAV and other viruses (Hiatt et al., manuscript accepted for publication in *Nat. Commun.*; Watanabe et al., 2014). From the PH targets, 10 were classified as pro-viral factors, and no targets were classified as antiviral factors (**Figure 5.1E**). Collectively among both screens, 47 host factors that regulate IAV infection are pro-viral, highlighting the strength of proteomics-based technologies in identifying human protein nodes critical to infection.

At the time of this report, SARS-CoV-2 variants of concern are continuing to surge, and it is predicted SARS-CoV-2 will circulate as an endemic virus during the typical flu season (Phillips, 2021). It is important to understand the molecular differences between these two co-circulating endemic respiratory viruses, and to identify host factors essential for their replication. To identify human proteins essential for both viruses, we knocked down the 54 IAV PPI and PH pro-viral and antiviral factors in A549 cells, and challenged knockdown cells with SARS-CoV-2 infection (**Figure S5.1A, Methods**). A549 cells were reverse transfected in six or nine replicates with gene-targeting siRNA or control siRNA, including non-targeting siRNA and ACE-2-targeting siRNA. Cells were assessed for viability with siRNA knockdown by cytotox staining, and infected with SARS-CoV-2 at MOI 0.1 PFU/cell for 72 hours. SARS-CoV-2 infection was quantified by RT-qPCR against viral N protein. Cell viability staining shows siRNA knockdown cells were above 65% viable, with a median cell viability ranging 94.3-97.3% across all siRNA knockdown cells and replicates (**Table S5.1**). The log₂ fold change in SARS-CoV-2 infection was calculated

for each experimental siRNA against a replicate-matched non-targeting control siRNA (**Methods**). We classified pro-viral and antiviral factors using a threshold of median log₂ fold change ≤ -2 or ≥ 2 , respectively, and identified three IAV PPI factors that regulate SARS-CoV-2 infection (**Figure 5.1F**, **Figure S5.1B**, **Table S5.1**). While no siRNA knockdowns from the PH dataset passed our log₂ fold change thresholding criteria for SARS-CoV-2 (**Figure S5.1B**), 7/10 PH targets mildly decreased SARS-CoV-2 infection with significance (p-value < 0.02) (**Table S5.1**). This may suggest an alternative perturbation method (e.g. drug inhibition) is needed to produce a robust effect on infection. To assess if there are similarities in kinase activities between IAV and SARS-CoV-2, we overlaid our phosphorylation data of IAV infection in human NHBE and THP-1 cells with phosphorylation data of SARS-CoV-2 infection in African green monkey Vero E6 cells (Bouhaddou et al., 2020) and human lung epithelial Calu-3 cells (Thorne et al., 2021). We identified eleven shared kinases (**Figure S5.1C**). Interestingly, these kinases share similar predicted kinase activity profiles upon infection with both viruses in their respective cell types (**Figure S5.1D**). Infection with IAV and SARS-CoV-2 resulted in increased activity of MAPK signaling members (MAP2K3, MAP2K6, MAPKAPK3, MAPKAPK5, MAPKAPK2, MAPK13) and RPS6K signaling members (RPS6KB1 and RPS6B2), and decreased activity of CDK2. These kinases provide examples of similar signaling signatures initiated by IAV and SARS-CoV-2, and may represent druggable pan-respiratory virus targets that modulate virus infection.

Collectively from the IAV PPI screen, IAV PH screen, and SARS-CoV-2 targets screen, we classified a total of 54 unique genes as regulators of viral infection (**Figure 5.1G**). All 54 genes regulate IAV infection, and three of these 54 genes also regulate SARS-CoV-2 infection. Two gene hits from the IAV PPI screen, PRKDC and AHNAK, are notable as they are IAV-interacting proteins with multiple IAV-regulated phosphorylation sites. PRKDC interacts with pH1N1, H3N2 and H5N1 M2 (**Figure 2.2**, **Table S2.1**), is predicted to increase in kinase activity during pH1N1

and H3N2 IAV infection (**Figure 3.1F**) and has six IAV-regulated phosphorylation sites itself (**Figure 3.1G**), PRKDC knockdown also increased IAV infection over 4-fold, identifying PRKDC as an antiviral factor (**Figure 5.1G**). AHNAK is a high confidence H5N1 NEP interactor in NHBE cells, and is identified in pH1N1 and H3N2 NEP pull-downs below our stringent scoring thresholds, indicating it might not be strain-specific (**Figure 2.2, Table S2.1**). AHNAK also has multiple phosphorylation events that are differentially regulated by the three IAV strains (**Figure 3.1G**), and it acts as a pro-viral factor with siRNA knockdown decreasing IAV infection (**Figure 5.1G**). Among the gene hits from the IAV PH screen, two IAV-regulated phosphoproteins and eight kinases were classified as pro-viral factors. These include two Aurora kinases (AURKA and AURKB), and four MAPK family members (MAPK12, MAPK3, MAPKAPK2, and MAPKAPK5). From the SARS-CoV-2 infection screen, siRNA knockdown of COPB1 (IAV M2 interactor) and AHNAK (IAV NEP interactor) decreased both IAV and SARS-CoV-2 infection (**Figure 5.1G**). In contrast, siRNA knockdown of RUVBL2 (IAV PB1 interactor) decreased IAV infection but increased SARS-CoV-2 infection (**Figure 5.1G**). RUVBL2 phenotype is novel for both viruses, and it is unclear how RUVBL2 differentially modulates infection. While we report these three proteins as IAV PPIs, to our knowledge, none are previously reported as PPIs with SARS-CoV-2 proteins. However, AHNAK was profiled as an RNA binding protein whose RNA binding kinetics peak early in SARS-CoV-2 infection (Kamel et al., 2021). Collectively, the two pro-viral factors for IAV and SARS-CoV-2 infection (COPB1 and AHNAK) represent potential gene targets for antiviral therapies against both respiratory viruses.

Methods

IAV siRNA screen

siRNA reverse transfection. A549 cells were reverse transfected in 24-well format with 290 gene-targeting siRNA (Dharmacon, siGENOME siRNA SMARTpool cherry picked pre-designed library, 0.1nmol/well), non-targeting control siRNA (Dharmacon, D-001206-14-05) or NP-targeting control siRNA (Dharmacon, custom sequence 5'-GGAUCUUAUUUCUUCGGAGUU-3'). In each well of a 24-well plate (Fisher, 08-772-1), siRNA was diluted to final concentration 75nM gene-targeting siRNA, 75nM non-targeting siRNA, or 30nM NP-targeting siRNA in 100 μ L with OptiMem Reduced Serum Media (Thermo Fisher, 31985062). One NT and one NP siRNA per 24-well plate were included for each replicate. 2 μ L/well Lipofectamine RNAiMAX Transfection Reagent (Thermo Fisher, 13778075) and 98 μ L/well OptiMem media were mixed and incubated for 5 minutes. 100 μ L RNAiMAX mix and 100 μ L siRNA dilution were combined in each well, mixed and incubated for 20 minutes. During this incubation, A549 cells were trypsinized with 0.25% trypsin EDTA (Fisher, MT 25-053-CI), pelleted at 1200rpm for 5 minutes, and resuspended in DMEM with L-glutamine without sodium pyruvate and 20% FBS at a density of 3×10^5 cells/mL. After the 20-minute incubation, 200 μ L of 6×10^4 A549 cells were added to each well and returned to incubate at 37°C and 5% CO₂ for 48 hours. The experiment was performed in two sets for PPI and PH targets, each with two replicates per gene to assay IAV infectivity and one replicate per gene to assay cell viability.

IAV infections. All IAV infections were performed in accordance with BSL2* biosafety procedures. A549 cells were infected in 24-well format 48 hours after reverse transfection. Cell media was aspirated and cells were washed with 400 μ L 1X PBS (Fisher, MT 21-030-CV). Cells were infected at MOI 0.1 with Influenza A/WSN/1933 H1N1 virus strain (kindly provided by S. Chanda lab) diluted in a total of 100 μ L 0.5% Bovine Serum Albumin (BSA) (GoldBio, A-420-100) in 1X PBS per well. Plates were returned to incubate for 1 hour at 37°C and 5% CO₂, and

rocked by hand every 10 minutes during incubation. Following adsorption, virus inoculum was aspirated, and 400 μ L post-infection media (DMEM with L-glutamine without sodium pyruvate, 0.1% FBS, 0.3% BSA, 0.5 μ g/mL TPCK-treated trypsin [Sigma-Aldrich, T8802-50MG], 1X P/S) was added to each well. Cells were returned to incubate at 37°C and 5% CO₂ for 24 hours. 24 hours post-infection, cells were trypsinized with 0.25% trypsin, moved to a 96-well U-bottom plate (Fisher 08-772-17), pelleted at 800 x g for 3 minutes, and fixed in 150 μ L 1% formaldehyde (Sigma, F8775-500ML) in 1X PBS. Cells were stored at 4°C until cell staining and flow cytometry.

Cell staining and flow cytometry. Percent IAV infection of A549 cells was quantified by immunostaining for IAV nucleoprotein (NP) followed by flow cytometry. To remove and exchange buffers between incubations and washes, cells were pelleted in 96-well U-bottom plates at 800 x g for 3 minutes. Fixed A549 cells were pelleted and incubated in 100 μ L block and permeabilization buffer (1% BSA, 0.1% saponin [Sigma, 47036-50G-F] in 1X PBS) for 30 minutes at room temperature. Cells were pelleted and incubated with 100 μ L 1:1000 dilution of anti-Influenza A nucleoprotein (NP) [HT103] antibody (Kerafast, EMS010) in block and permeabilization buffer for 1 hour at room temperature. Cells were pelleted, washed once with 200 μ L wash buffer (1% BSA in 1X PBS) and incubated in 100 μ L 1:1000 goat anti-mouse IgG (H+L) secondary antibody Alexa Fluor Plus 488 (Fisher, A32723) in block and permeabilization buffer for 1 hour at room temperature in the dark. Cells were washed once with 200 μ L wash buffer and fixed in 150 μ L 1% formaldehyde in 1X PBS. Samples were run in 96-well format on an Attune NxT flow cytometer (Thermo Fisher). A549 cells were gated at forward side scatter voltage 80 and side scatter voltage 275 (R1, A549 singlet cells), and Alexa Fluor Plus 488 signal quantified by blue laser 1 at voltage 205 (percent NP+). 100 μ L of cells were acquisitioned and all events recorded at 1000 μ L/min.

siRNA viability of A549 knockdown cells was quantified by live-cell amine-reactive viability staining to fluorescently label non-viable cells followed by flow cytometry. 48 hours after transfection, cells were trypsinized with 0.25% trypsin, neutralized with DMEM with L-glutamine without sodium pyruvate, 10% FBS and 1X P/S, and transferred from 24-well plates to 96-well U bottom plates. To remove and exchange buffers between incubations and washes, cells were pelleted in 96-well plates at 800 x g for 3 minutes. Cells were pelleted and incubated in 100 μ L/well 1:500 Ghost Dye Red 710 (Tonbo Biosciences, 13-0871-T100) in 1X PBS for 20 minutes at room temperature protected from light. Cells were pelleted and washed twice with 100 μ L/well MACS buffer (PBS no calcium or magnesium [Fisher, MT-21031CV], 2mM EDTA [Fisher, MT-46034CI], 0.5% BSA; filtered through 500mL EMD Millipore Stericup™ Sterile Vacuum Filter Units .22 μ M PVDF [Fisher, SCGVU05RE]). Cells were pelleted and resuspended in 150 μ L 1X PBS, and immediately analyzed in 96-well format on an Attune NxT flow cytometer (Thermo Fisher). A549 cells were gated at forward side scatter voltage 60 and side scatter voltage 280 (R1, A549 singlet cells), and Ghost Dye Red 710 signal quantified by red laser 2 at voltage 260 (dead cells). 100 μ L of cells were acquisitioned and all events recorded at 1000 μ L/min.

Final cell gating and quantification for data analysis of %Ghost 710+ cells (percent dead cells) and %NP+ cells (percent IAV infectivity) was performed with FlowJo version 9.3.2 software. For cell viability, %Ghost710+ cells (percent dead cells) and %Ghost 710- cells (percent alive cells) for each siRNA knockdown are reported as calculated with FlowJo (**Table S5.1**). For IAV infectivity, singlet cell count and %NP+ cells for each experimental siRNA are reported as calculated with FlowJo (**Table S5.1**). Singlet cell count was used as a readout for cell viability of A549 cells with siRNA knockdown and IAV infection. Singlet cell count and %NP+ cells for each experimental siRNA was normalized to the mean cell count or %NP+ cells of non-targeting (NT) control siRNA corresponding to each set of 24-well plates transfected, infected, collected and

stained concurrently. Log₂ fold changes in viability (singlet cell count experimental siRNA vs NT siRNA) and percent IAV infection (%NP+ cells experimental siRNA vs NT siRNA) were calculated from these values (**Table S5.1**).

SARS-CoV-2 siRNA screen

siRNA transfections. A549 cells stably expressing the ACE2 receptor (A549-ACE2) were kindly provided by O. Schwartz and were maintained at 37°C, 5% CO₂ in DMEM supplemented with 10% FBS, Pen/Strep and 10 µg/mL blasticidin S (Sigma, SBR00022). An siRNA library (Dharmacon, OnTargetPlus siRNA SMARTpool cherry picked pre-designed library, 2nmol/well) of 54 target genes of interest, a non-targeting control and an ACE2-targeting control was used to transfect A549-ACE2 cells, previously seeded at a density of 6250 cells per well in a 384-well plate. Briefly, 0.1µL of Lipofectamine RNAiMAX reagent and 4pmoles of each siRNA pool were diluted in a final volume of 10µL of OptiMEM. Following 5 minutes of incubation, 10µL of the siRNA-lipid complexes were added to the cells, which were then incubated for 48 hours. Cells were then either infected with SARS-CoV-2 or left untreated for another 72 hours to determine cell viability using the CellTiter-Glo luminescent viability assay (Promega, G7570) according to the manufacturer's protocol. Luminescence was measured in a Tecan Infinity 2000 plate reader, and the percentage of metabolically active cells was calculated by normalizing the values to those obtained in untreated (100% viability) and 4% formalin-treated (0% viability) conditions included in each experiment. Experiments were performed in technical triplicate, with two biological replicates for PPI targets (total n=6 per gene) and three biological replicates for PH targets (total n=9 per gene).

Virus infections and qRT-PCR quantification. The SARS-CoV-2

(BetaCoV/France/IDF0372/2020) strain was a kind gift from the National Reference Centre for Respiratory Viruses at Institut Pasteur Paris, and was propagated once in VeroE6 cells to

generate viral stock. 48 hours post-transfection, A549-ACE2 cells were infected with SARS-CoV-2 at MOI 0.1 PFU per cell. Briefly, cell media was removed and 20 μ L of viral inoculum, prepared in serum-free media, was added to each well. After 1 hour adsorption at 37°C, the inoculum was removed and replaced by DMEM supplemented with 2% FBS and Pen/Strep. The supernatant was harvested 72 hours post-infection and heat-inactivated at 95°C for 5 minutes. The presence of viral genomes was subsequently quantified using the Luna Universal One-Step RT-qPCR kit (New England Biolabs, E3005S). Specific primers targeting the N gene (5'-TAATCAGACAAGGAACTGATTA-3' [forward] and 5'-CGAAGGTGTGACTTCCATG-3' [reverse]) were used as previously described (Chu et al., 2020). RT-qPCR was performed under the following cycling conditions in an Applied Biosystems QuantStudio 6 thermocycler: 55°C for 10 minutes, 95°C for 1 minute, 40 cycles of 95°C for 10 seconds, followed by 60°C for 1 min. The number of viral genomes in the supernatant was calculated by performing a standard curve with RNA derived from a viral stock with a known viral titer, and is expressed as PFU equivalents per mL. These data were then used to compute log₂ fold changes for experimental siRNA normalized to replicate-matched non-targeting controls. The log₂ fold changes were computed separately for each replicate, and the median and median absolute deviation (MAD) were then calculated for each sample across all its replicates in the screen set (six replicates for PPI and nine replicates for PH). The PPI and PH screen sets were analyzed separately, and the results are reported in **Figure 5.1**, **Figure S5.1** and **Table S5.1**. P-values were calculated using two-sided Wilcoxon signed-rank tests.

FIGURES AND LEGENDS

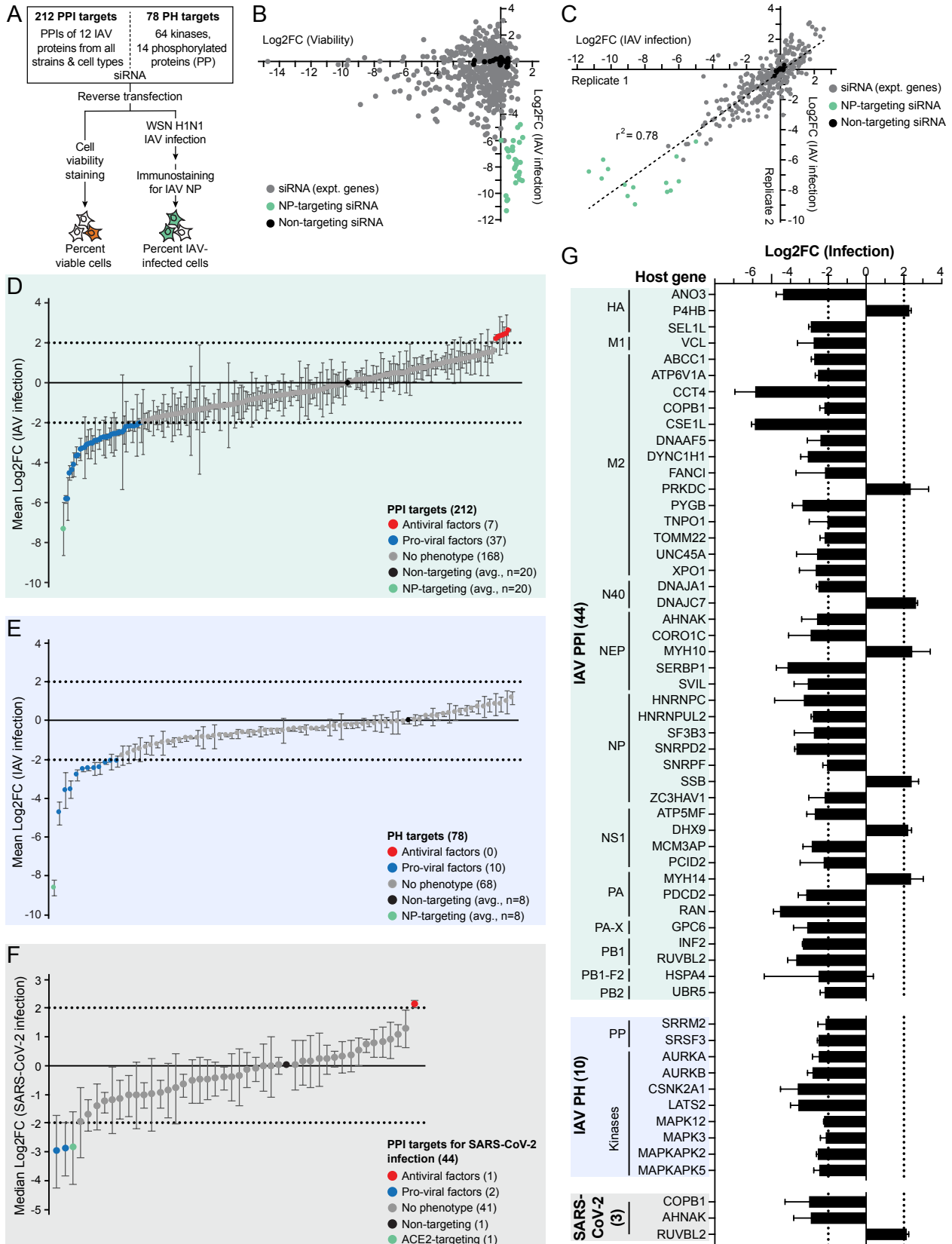


Figure 5.1 siRNA knockdown identifies pro-viral and antiviral factors of IAV infection. (A) An arrayed siRNA screening approach knocking down 212 PPI and 78 PH targets, including 64 kinases and 14 phosphorylated proteins (PP). A549 cells were reverse transfected with pools of four gene-targeting siRNA, pools of four non-targeting siRNA or IAV NP-targeting siRNA. Cell viability was determined at 48 hours post-transfection by live-cell staining and quantification by flow cytometry. Cells were infected at 48 hours post-transfection with Influenza A/WSN/1933 H1N1 virus at an MOI of 0.1. At 24 hours post-infection, cells were fixed and immunostained for IAV NP as a readout for percent IAV infection and quantified by flow cytometry. (B) Plot comparing the log₂ fold change in cell viability with siRNA knockdown (x-axis) against the log₂ fold change in infection (y-axis) for each gene from each replicate. IAV NP-targeting siRNA (green dots), non-targeting control siRNA (black dots), and experimental gene-targeting siRNA (grey dots) are represented. (C) Replicate correlation plot comparing the mean log₂ fold change in IAV infection between two replicates. Dots are colored as in (B). (D-E) Distribution of the mean log₂ fold change in IAV infection of experimental siRNA normalized to non-targeting control siRNA for (D) 212 PPI targets and (E) 78 PH targets. Error bars represent standard deviation. siRNA with a log₂ fold change ≤ -2 were labeled pro-viral factors (blue dots) and siRNA with a log₂ fold change ≥ 2 were labeled antiviral factors (red dots). siRNA in between these thresholds were labeled no/weak phenotype (grey dots). The mean log₂ fold change in IAV infection of positive-control IAV NP-targeting siRNA (green dot) and non-targeting control siRNA (black dot) are represented. (F) Distribution of log₂ fold changes of SARS-CoV-2 infection for siRNA knockdown of 44 PPI targets compared to non-targeting control siRNA (black dot), plotted as the median of six replicates for each target. siRNA with median log₂ fold change ≤ -2 were labeled pro-viral factors (blue dots) and siRNA with median log₂ fold change ≥ 2 were labeled antiviral factors (red dots). siRNA in between these thresholds were labeled no/weak phenotype (grey dots). The median log₂ fold change of positive-control ACE2-targeting siRNA is represented (green dot). Error bars represent median absolute deviations (MAD). (G) Bar chart of pro-viral and antiviral factors for IAV and SARS-CoV-2 screens. The mean log₂ fold change in IAV infection is plotted for 44 PPI factors (top), and for 10 PH factors (middle). Error bars represent standard deviation. The median log₂ fold change in SARS-CoV-2 infection is plotted for three IAV PPI factors (bottom). Error bars represent median absolute deviations (MAD). PPI pro-viral and antiviral factors map back to 12 IAV proteins (top, labeled at left). PH pro-viral and antiviral factors map back to two phosphorylated proteins (PP) and eight kinases (middle, labeled at left).

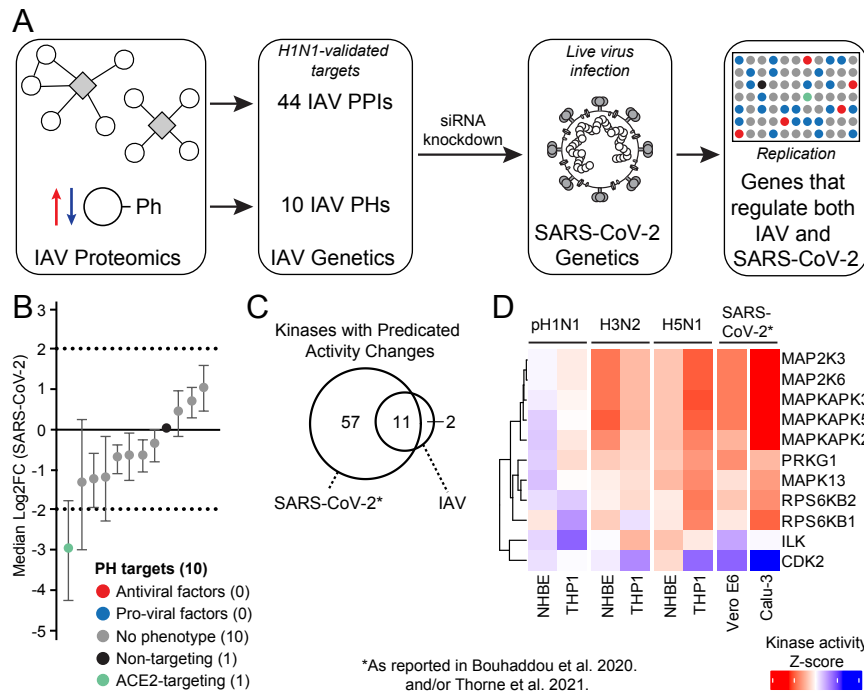


Figure S5.1 Probing IAV targets against SARS-CoV-2 infection identifies factors that regulate both IAV and SARS-CoV-2, Related to Figure 5.1. (A) IAV and SARS-CoV-2 comparison strategy. From the IAV PPI and PH proteomic datasets, 54 IAV targets encompassing 44 siRNA-validated PPIs and 10 siRNA-validated PH proteins (from **Figure 5.1D-E**) were tested against SARS-CoV-2 infection by siRNA knockdown in A549 cells to identify genes that regulate both IAV and SARS-CoV-2 infection. (B) Distribution of log₂ fold changes of SARS-CoV-2 infection for siRNA knockdown of 10 PH targets compared to non-targeting control siRNA (black dot), plotted as the median of nine replicates for each target. siRNA with median log₂ fold change ≤ -2 were labeled pro-viral factors (blue dots) and siRNA with median log₂ fold change ≥ 2 were labeled antiviral factors (red dots). siRNA in between these thresholds were labeled no/weak phenotype (grey dots). The median log₂ fold change of positive-control ACE2-targeting siRNA is represented (green dot). Error bars represent median absolute deviations (MAD). (C) Comparison of kinases with significant activity changes during IAV infection (this study) and during SARS-CoV-2 infection (from (Bouhaddou et al., 2020), asterisk signifies data was derived from this publication). (D) Heatmap of kinase activity predictions from the phosphorylation data with IAV infection (at 18 hours post-infection with pH1N1 and H3N2, and at 12 hours post-infection with H5N1; in NHBE and THP-1 cells) and SARS-CoV-2 infection (at 24 hours post-infection; in Vero E6 and Calu-3 cells) from published studies (Bouhaddou et al., 2020; Thorne et al., 2021) and thresholded at p-value < 0.05 . Asterisk signifies SARS-CoV-2 data is derived from (Bouhaddou et al., 2020; Thorne et al., 2021). Kinase Z-score reflects predicted kinase activity, with increased kinase activity in red and decreased kinase activity in blue.

SUPPLEMENTAL TABLE

Table S5.1 siRNA targets and log₂FC against IAV and SARS-CoV-2 infection, Related to Figures 5.1 and S5.1. For the IAV screen, this table reports a list of siRNA target genes from the IAV PPI and PH datasets with corresponding cell viability (IAVsiRNA_CellViability tab) and the log₂ fold change in IAV infection (IAVsiRNA_IAVinfectivity tab). For the SARS-CoV-2 screen, this table reports a list of siRNA target genes with corresponding cell viability (SARS2siRNA_CellViability tab) and the log₂ fold change in SARS-CoV-2 infection (SARS2siRNA_SARSCoV2infectivity tab). Table is available online only as supplemental material.

CHAPTER 6

Host-Directed Compounds Targeting IAV and SARS-CoV-2 Factors Identify Inhibitors of pH1N1, H3N2 and H5N1 IAV Infection

While therapeutics that target IAV proteins are available and in clinical use for antiviral treatment, increasing levels of drug resistant viral populations limit their efficacy, particularly for 2009 pH1N1 and pH1N1-like seasonal strains and H3N2 seasonal strains (Gubareva et al., 2019; Hussain et al., 2017; Omoto et al., 2018; Takashita et al., 2019). Host-directed therapies offer an alternative treatment approach by targeting human proteins that regulate viral infection. To identify potential host-directed therapies against IAV infection, we identified and screened compounds targeting a subset of the 44 siRNA-validated pro-viral and antiviral PPI factors and 13 kinases with IAV-modulated activity changes (**Figure 6.1A**). A total of 29 unique compounds targeting eight PPI factors and 12 kinases (**Table S6.1**) were manually curated by literature search and selected based on target specificity and drug availability. Due to similarities in kinase activity signatures between IAV and SARS-CoV-2 (**Figure S5.1D**), we also leveraged previously published SARS-CoV-2 PH data reporting kinase-targeting antiviral compounds (Bouhaddou et al., 2020) to mine our IAV PH data for new drugs with potential dual activity against both respiratory viruses. We identified and screened 8 compounds with antiviral activity against SARS-CoV-2 (Bouhaddou et al., 2020) that target 8 kinase pathways that were detected in our global IAV phosphorylation data (**Figure 6.1A, Table S6.1**). A total of 37 unique compounds were screened against pH1N1, H3N2 and H5N1 IAV infection in A549 cells (**Figure S6.1, Table S6.1**). Cell viability was determined by MTT assay in uninfected A549 cells and quantification of percent alive cells. Antiviral activity was measured by immunostaining for IAV NP protein followed by high throughput imaging and quantification of percent IAV-infected cells. Compounds with selectivity index (SI) > 2 were classified as having antiviral activity. We identified 16 compounds with antiviral activity against at least one IAV strain, and seven compounds with antiviral activity against all three IAV strains. The seven pan-IAV inhibitors target three IAV PPIs (both pro-viral and antiviral), two IAV-modulated kinases (both upregulated and downregulated) and two SARS-CoV-2 antiviral targets (**Table S6.1**).

We found inhibitors of four IAV PPI factors to possess antiviral activity against at least two IAV strains (**Figure 6.1B-E**). Three factors are IAV M2 interactors, and one factor is an IAV HA interactor. V1-ATPase subunit ATP6V1A interacts with M2 from all three IAV strains, and its targeting compound, Bafilomycin A1, shows potent broad spectrum activity (**Figure 6.1B**). Bafilomycin A1 has been reported to inhibit IAV infection with PR8 H1N1 strain in A549 cells (Yeganeh et al., 2015), consistent with its pan-IAV antiviral activity in our study. Alexidine, which also targets V1-ATPase/ATP6V1A, decreases infection of all three strains but shows higher cytotoxicity and a SI < 2 (**Figure S6.1, Table S6.1**). ATP-binding cassette transporter ABCC1 is a high-confidence interactor of H5N1 M2, and interacts below scoring thresholds with pH1N1 and H3N2 M2. Interestingly, ABCC1-targeting compound daunorubicin shows antiviral activity against all three strains (**Figure 6.1C**), indicating the ABCC1-M2 interaction may not be strain-specific. DNA-dependent protein kinase (DNA-PK) PRKDC is an M2 interactor in all three IAV strains and a kinase with IAV-modulated activity. Interestingly, DNA-PK inhibitor NU7441 inhibits only pH1N1 and H3N2 infection (**Figure 6.1D**), which is consistent with our global PH data showing increased activity of PRKDC in only pH1N1 and H3N2 infection (**Figure 3.1F**). To our knowledge, daunorubicin (ABCC1), and NU7441 (PRKDC) are novel inhibitors of IAV infection. PACMA31, which targets IAV HA PPI factor protein disulfide-isomerase (PDI) P4HB that interacts with H3N2 HA, also shows antiviral activity against all three IAV strains (**Figure 6.1E**). In total, for these PPI factors, the effect of drug treatment on IAV infection largely mirrored the effect of siRNA knockdown (**Figure 5.1G**), except for P4HB and PRKDC, where siRNA knockdown increased IAV infection but compound treatment inhibited IAV infection.

In addition to the PRKDC kinase inhibitor, we found that inhibitors of seven additional kinases show antiviral activity against at least one strain of IAV (**Figure S6.1, Table S6.1**). Two of these seven compounds show pan-IAV antiviral activity. Dinaciclib, an inhibitor of cyclin-dependent kinase CDK2, shows potent broad spectrum activity against the three strains (**Figure 6.1F**). A

previous study reports Dinaciclib antiviral activity with H7N9 IAV (Perwitasari et al., 2015), further supporting broad spectrum potency. ULK1 inhibitor MRT68921 shows antiviral activity against H3N2 and H5N1 (SI > 2), and decreases pH1N1 infection (SI < 2) (**Figure 6.1G**, **Table S6.1**). ULK1 in complex with other proteins has been shown to activate mTOR-dependent autophagy (Petherick et al., 2015), a pathway that is necessary for IAV infection (Wang et al., 2019). To our knowledge, MRT68921 is a novel antiviral for IAV, likely acting through ULK1 inhibition to downregulate autophagy and suppress infection. Additionally, three inhibitors of four members of the MAPK pathway show antiviral activity against at least one IAV strain (**Figure 6.1H**). Lestaurtinib, which targets MAP2K3 and MAP2K6, shows antiviral activity against pH1N1 and H5N1 (SI > 2), and decreases H3N2 infection (SI < 2) (**Figure 6.1H**). MAPK-13-IN-1, which targets MAPK13 (p38 δ), shows broad spectrum activity with some differences in potency between the three IAV strains (**Figure 6.1H**). Although SI values for MAPK-13-IN-1 cannot be quantitatively calculated based on the concentrations we used (**Table S6.1**), the lack of toxicity at the tested concentrations indicates SI is likely to be above 2. PF-3644022, which targets MAPKAPK2, shows antiviral activity against H5N1 (**Figure 6.1H**). Due to virus stock issues, pH1N1 was unable to be screened with PF-3644022. However, our global PH data show changes in MAPKAPK2 activity during infection for all three strains (**Figure 3.1F**), and siRNA knockdown of MAPKAPK2 inhibits WSN H1N1 infection (**Figure 5.1G**), indicating MAPKAPK2 may be a regulatory node for multiple IAV strains. Taken together, these three MAPK-targeting compounds suggest the MAPK signaling pathway may be essential for multiple strains of IAV infection and targetable for host-directed antiviral therapy.

Of the eight SARS-CoV-2 antiviral compounds screened, three compounds show antiviral activity against at least two strains of IAV (**Figure 6.1I-K**). Gilteritinib shows broad spectrum antiviral activity against the three IAV strains (**Figure 6.1I**). Gilteritinib targets AXL kinase, which functions in the MAPK signaling pathway upstream of p38, MAP2K3 and MAP2K6. Although

inhibitors against MAP2K3 and MAP2K6 (Lestaurtinib) and MAPK13 (p38 δ) (MAPK13-IN-1) showed antiviral activity against multiple IAV strains, other SARS-CoV-2 antiviral p38 inhibitors screened against IAV infection did not (Ralimetinib targeting MAPK14 (p38 α) and MAPK11 (p38 β); ARRY-797 targeting MAPK14 (p38 α)) (**Figure S6.1, Table S6.1**). This suggests that IAV and SARS-CoV-2 converge on upstream kinases in the MAPK pathway, and that their kinase signaling activity is essential for infection. Pictilisib, which targets PIK3CA and PIK3CD, also shows broad spectrum antiviral activity against the three IAV strains (**Figure 6.1J**). SI values for Pictilisib could not be quantitatively calculated based on the concentrations we used (**Table S6.1**), however the lack of toxicity indicates SI is likely to be above 2. Previous findings that other PIK3CA-targeting compounds inhibit infection by two different IAV strains further support PIK3CA as a targetable node for IAV host-directed therapy (Ehrhardt et al., 2006). PIK3CA has been shown to act through PR8 H1N1 IAV protein NS1 (Ehrhardt et al., 2007), and we identified PIK3CA as an interactor of pH1N1 NS1 (**Figure 2.2**), but how PIK3CA regulates H3N2 and H5N1 infection is unclear. MK-2206, which targets the AKT kinases (AKT1, AKT2, AKT3), shows strong antiviral activity against H5N1 and moderate antiviral activity against pH1N1 (**Figure 6.1K**). AKT signaling may be a unique host signaling pathway more heavily utilized by H5N1 avian-derived IAV strain. Collectively, these three compounds provide examples of orthologous SARS-CoV-2 PH data revealing new therapeutic targets for multiple strains of IAV. These three compounds could serve as potential antiviral treatments for both respiratory viruses. In addition, Dinaciclib (CDK2) and MAPK13-IN-1 (MAPK13), which show antiviral activity against pH1N1, H3N2 and H5N1 IAV in our study (**Figure 6.1F,H**), were also shown to have antiviral activity against SARS-CoV-2 (Bouhaddou et al., 2020). In total, these five compounds with antiviral activity against multiple strains of IAV and SARS-CoV-2 represent potential targets for potential host-directed pan-respiratory virus therapies.

Methods

Compound treatment, cytotoxicity and IAV antiviral assays. PPI-targeting and kinase-targeting compounds were manually curated by target-specific literature search performed by specialists within our group. IAV PB2-targeting compound Pimodivir (VX-787) was included as a positive control due to its antiviral activity against multiple H1N1-, H3N2- and H5N1-subtype IAV in human cell and mouse models and in patients (Byrn et al., 2015; Finberg et al., 2019; Trevejo et al., 2018). Compounds were purchased from vendors specified in **Table S6.1**. Drug antiviral assays were performed as compounds and IAV strains were received and available, and each set of compounds was performed alongside the Pimodivir control. For drug antiviral assays, A549 cells were seeded at 8,000 cells per well in DMEM growth media described above in 96-well plates (Falcon, 353072) 24 hours before IAV infection. Cells were pretreated with compound 2 hours before infection, where cell growth media for the corresponding well was replaced with media containing 20 μ M, 6 μ M, 2 μ M, 700nM, 200nM or 80nM of each compound, or the equivalent volume of DMSO vehicle (control). The only exception is Pimodivir, which was added at 0.2 μ M, 0.06 μ M, 0.02 μ M, 7nM, 2nM or 0.8nM. Each compound or DMSO vehicle was tested in triplicate. Cells were mock infected for cell toxicity assay, or infected with IAV for antiviral assay. Drug-containing media was removed and replaced with A/California/04/2009 H1N1 (MOI 0.5 PFU per cell), A/Wyoming/03/2003 H3N2 (MOI 0.5 PFU per cell), A/Vietnam/1203/2004 H5N1 HALo (MOI 0.05 PFU per cell), or no virus in 0.5% BSA in 1X PBS containing TPCK-trypsin (Sigma-Aldrich, T8802-50MG). Cells were incubated for 1 hour at 37°C to allow virus adsorption. Virus inoculum was subsequently removed, and 100 μ l of drug- or vehicle-containing media was added. Uninfected A549 cells were assayed for cytotoxicity in parallel with the antiviral assay, matched for time and concentration. For cytotoxicity, 10 μ l of Cell Proliferation Kit I (MTT) labeling reagent (Roche, 11465007001) was added to each well to a final concentration 0.5mg/mL, and incubated for 3 hours at 37°C. 100 μ l of solubilization solution (Roche, 11465007001) was then added to each well, and plates were incubated at

37°C overnight. Spectrophotometrical absorbance of each well was measured using a microplate (ELISA) reader (BioTek Instruments, NEO2SM) to quantify cell viability. For IAV infection, cells were fixed to the 96-well plate in final concentration 4% formaldehyde for 20 minutes and immunostained for IAV NP protein with a DAPI counterstain at room temperature. Briefly, cells were washed three times with 1X PBS for 5min, permeabilized with 0.1% Triton X-100 (Fisher Scientific, 9002-93-1) in 1X PBS for 15min, blocked in 1% BSA in 1X PBS for 1hr and incubated in 1:1000 anti-IAV NP (an in-house monoclonal antibody HT103, provided by Dr. Thomas Moran, Thomas.Moran@mssm.edu) and DAPI (Thermo Scientific, 62248) for 1hr. Cells were washed again three times with 1X PBS for 5min, and incubated in 1:1000 goat anti-mouse AlexaFluor 488 (Invitrogen, A11029) in the dark for 1hr. Cells were washed twice in 1X PBS for 5min, suspended in 1X PBS and subsequently analyzed by Celigo Image Cytometer (Nexcelom) using instrument cell counting software to count the total number of IAV-infected cells (green channel, 536nm). Infectivity was measured by the accumulation of viral NP protein (fluorescence accumulation). Percent infection was quantified as $((\text{Infected cells}/\text{Total cells}) - \text{Background}) * 100$, and the DMSO control was then set to 100% infection for analysis. Data analysis was performed in GraphPad Prism (version 9.3.0), using nonlinear regression fit and fit hill functions to identify IC50, IC90, CC10 and CC50 values (**Table S6.1**). Selectivity index (SI) for each compound was calculated as $\text{CC50}/\text{IC50}$ (**Table S6.1**), and compounds with a SI > 2 were reported as antiviral.

FIGURES AND LEGENDS

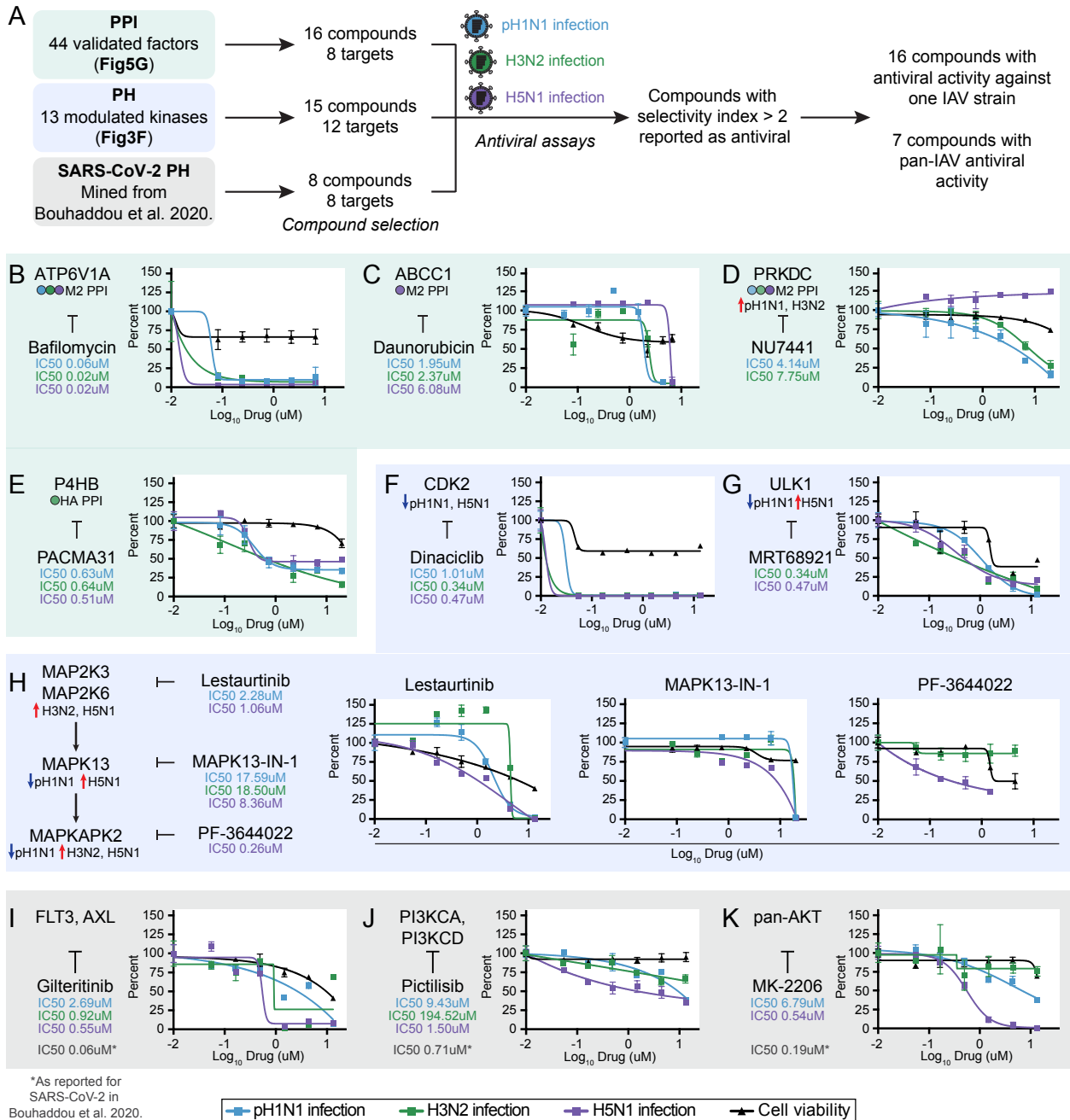


Figure 6.1 Host-directed compounds targeting IAV and SARS-CoV-2 factors identify inhibitors of pH1N1, H3N2 and H5N1 IAV infection. (A) Compounds were manually curated for targets from the 44 siRNA-validated PPI factors (16 compounds, 8 targets) and from the 13 modulated kinases in the PH data (15 compounds, 12 targets), totaling 29 unique compounds across both data types. Compounds with antiviral activity against SARS-CoV-2 were mined from a SARS-CoV-2 global PH study (Bouhaddou et al., 2020) to identify and test new drugs with potential dual activity against IAV (8 compounds, 8 targets). In total across all three data types, 37 unique compounds were screened for their effect on pH1N1, H3N2 and H5N1 infection by antiviral assay (see also **Table S6.1**). Compounds with a selectivity index (SI) > 2 were reported

as antiviral. 16/37 compounds showed antiviral activity against at least one strain of IAV, and 7/37 compounds showed antiviral activity against all three IAV strains. For panels (B-K), A549 cells were pre-treated with compound at the indicated doses and infected with pH1N1, H3N2 or H5N1 IAV for 48 hours. Percent IAV-infected cells was determined by immunostaining against IAV NP protein followed by high throughput imaging and quantification (pH1N1 blue line, H3N2 green line, H5N1 purple line). Percent cell viability (black line) was quantified by MTT assay in uninfected A549 cells (see also **Methods**). To the left of each panel, schematics mark PPI or PH target and corresponding compound. Targets are annotated with PPI or predicted kinase activities from the PPI or PH data. Compounds are annotated with IC₅₀ values for the IAV strains in which SI > 2. Error bars represent standard error of mean (SEM). (B-D) Dose-response curves for M2 PPI-targeting compounds, including: ATP6V1A-targeting compound bafilomycin A1; ABCC1-targeting compound daunorubicin; and PRKDC-targeting compound NU7441. PRKDC is also a kinase identified in the IAV PH data. (E) Dose-response curve for HA PPI P4HB-targeting compound PACMA31. (F-G) Dose-response curves for PH kinase-targeting compounds, including: CDK2-targeting compound dinaciclib; and ULK1-targeting compound MRT68921. (H) Dose-response curves for members of the MAPK pathway (pathway schematic on the left), including MAP2K3, MAP2K6, MAPK13 and MAPKAPK2, each annotated with their corresponding compounds. Due to virus stock issues, pH1N1 was unable to be screened with PF-3644022. (I-K) Dose-response curves for SARS-CoV-2 mined antiviral compounds targeting three kinase pathways modulated in IAV and SARS-CoV-2 infection, including: FLT3 and AXL targeted by Gilteritinib; PI3KCA and PI3KCD targeted by Pictilisib; and AKT1, AKT2 and AKT3 (pan-AKT) targeted by MK-2206. SARS-CoV-2 IC₅₀ values are included as reported in (Bouhaddou et al., 2020), where SARS-CoV-2 infection was quantified by RT-qPCR of SARS-CoV-2 N protein in compound-treated A549-ACE2 cells.

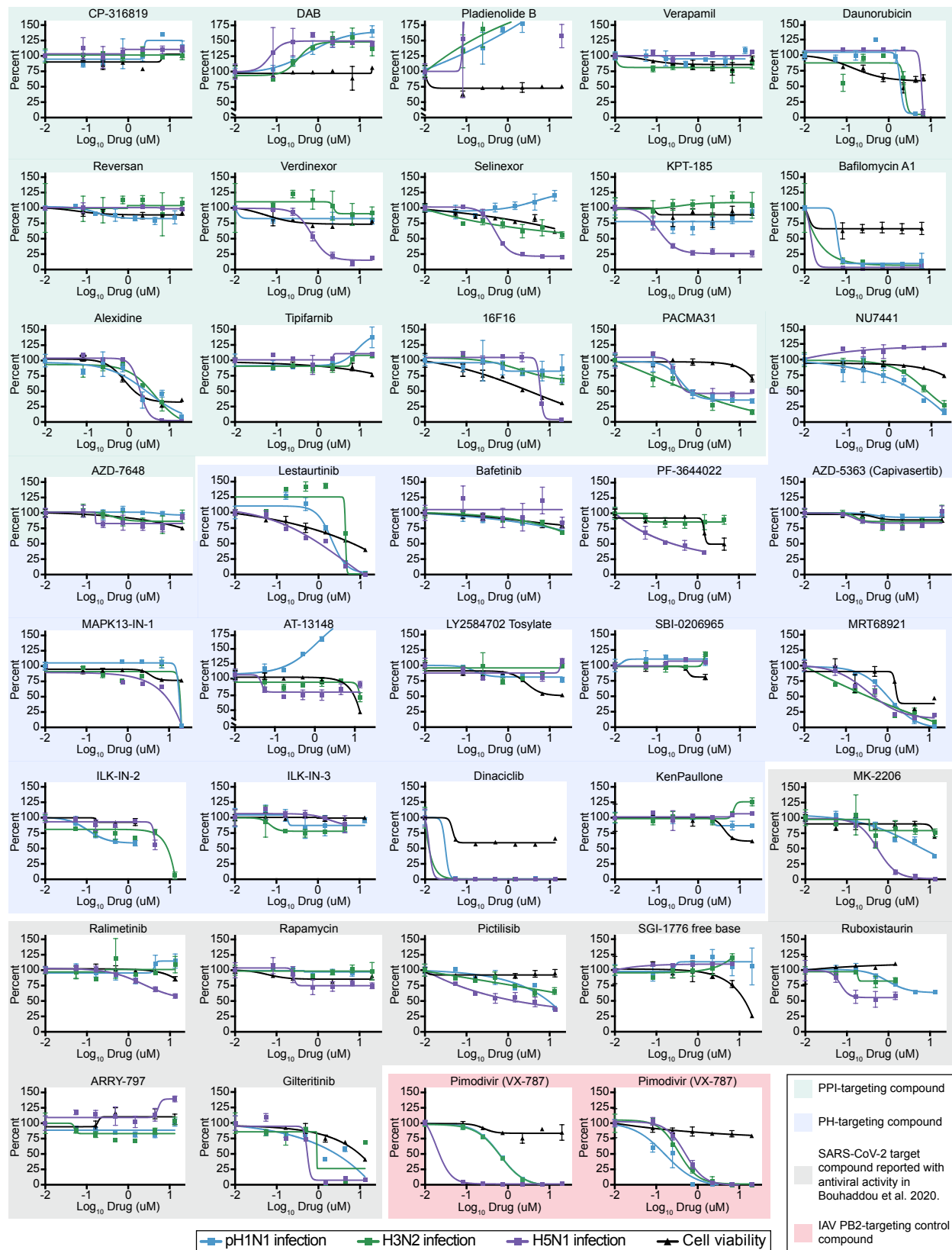


Figure S6.1 Host-directed compound dose-response curves for pH1N1, H3N2 and H5N1 IAV and cell viability, Related to Figure 6.1. Dose-response curves for a total of 37 host-directed compounds, including: 29 IAV PPI- and kinase-targeting drugs, and 8 kinase-targeting drugs mined from a published study with antiviral activity against SARS-CoV-2 (Bouhaddou et al., 2020). Due to virus stock issues, pH1N1 was unable to be screened with PF-3644022. Dose-response curves are also included for IAV PB2-targeting control compound Pimodivir (VX-787), which was run in two sets. Assays were performed in A549 cells, with high throughput imaging and quantification of percent IAV-infected cells (%NP+ cells) for each of the three IAV strains (pH1N1 blue line, H3N2 green line, H5N1 purple line), and percent viable cells (black line). The mean of three biological replicates is shown. Error bars represent standard error of mean (SEM).

SUPPLEMENTAL TABLE

Table S6.1 Compound screening against IAV infection, Related to Figures 6.1 and S6.1.

Table listing the 37 host-directed compounds screened in this study (Compounds tab), including: 29 IAV PPI- and kinase-targeting compounds; and 8 kinase-targeting compounds mined from a published study with antiviral activity against SARS-CoV-2 (Bouhaddou et al., 2020). Table reports the compound's designated protein target and maps the protein target to the dataset in which it was identified, either from the functionally validated IAV PPI dataset (**Figure 5.1G**), IAV kinase analysis (**Figure 3.1F**), or from a SARS-CoV-2 global PH study that reports compounds with antiviral activity against SARS-CoV-2 (Bouhaddou et al., 2020). Also reported in the table are each compound's U.S. approval status, supplier, catalog number, PubChem ID, IC50 and IC90 (IAV inhibition), CC10 and CC50 (cell viability), and selectivity index (SI). Compounds that were screened and do not have IAV inhibition (IC50 or IC90) or cell toxicity (CC10 or CC50) values as determined by nonlinear regression fit and fit hill functions are reported as >20uM. For compounds where CC50 is reported as >20uM, SI was calculated and reported as $>(20\mu\text{M}/\text{IC}50)$. For compounds where CC50 and IC50 are reported as >20uM, SI is reported as N/A. Column descriptions are provided in the final tab. Table is available online only as supplemental material.

CHAPTER 7

Discussion

This study represents a first-in-class, integrative systems biology approach that unifies *ex vivo* proteomic data with patient genomic data to generate a comprehensive network model of IAV infection. By studying circulating or potential-circulating IAV strains, we identify essential, druggable host targets that offer clinically relevant potential treatment alternatives to increasingly obsolete classes of IAV protein-targeting drugs. Using a two-pronged proteomic approach, we interrogated three different IAV strains (pH1N1, H3N2, and H5N1) in multiple cell types of infection (primary bronchial epithelial, lung epithelial and myeloid cell lines) to identify novel strain-specific and pan-IAV PPIs and IAV-modulated host kinase signaling pathways. Combining the cellular proteomic data with whole exome sequencing data from an influenza patient cohort pinpointed a number of potential molecular regulators of host response and determinants of disease outcome. By functional genetic screening, we found 54 human genes that map back to 44 PPI factors and 10 PH factors act as pro-viral and antiviral factors in IAV infection. Three of these functional PPI factors also regulate infection by SARS-CoV-2, and act as pro-viral (COPB1, AHNAK) and antiviral (RUVBL2) factors of SARS-CoV-2 infection. Screening compounds that target IAV-interacting and IAV-modulated proteins identified 16 compounds that suppress replication by at least one strain of IAV, with seven compounds exhibiting pan-IAV activity and five compounds inhibiting multiple strains of IAV and SARS-CoV-2. These findings provide novel gene targets and compounds that could help inform rational drug design or drug repurposing strategies for HDT to treat influenza and COVID-19.

By AP-MS, we identified a total 332 IAV-human PPIs (**Figure 2.1C-D, Table S2.1**) mapped between 12 IAV proteins of pH1N1, H3N2 and H5N1 IAV and 214 human proteins in three different cell types (**Figure 2.2**). We identified both known and novel IAV-human PPIs, and pan-IAV and strain-specific PPIs. PPIs shared across all three viruses include proteins involved in RNA processing, nuclear transport, macroautophagy and fatty acid metabolism (**Figure 2.2**), and may represent co-opted protein targets essential to multiple strains of IAV infection.

Consistent with this, human proteins that interact above scoring thresholds with IAV proteins from at least two strains represent 13/44 factors whose knockdown decreased IAV infection (**Figure 5.1G, Table S5.1**), and represent targets for two compounds with antiviral activity against at least two strains of IAV (**Figure 6.1B,D**). In comparison, strain-specific interactors are most noticeable among IAV proteins with known roles in modulating host response, including NS1, PA-X and PB1-F2 (**Figure 2.2**). This unique co-opting of host protein complexes may be reflective of unique virological characteristics for each strain, for example pandemic or potential-pandemic vs seasonal (i.e. pH1N1 or H5N1 vs H3N2) or human-adapted vs avian (i.e. pH1N1 or H3N2 vs H5N1) IAV. The lower overlap of PPIs between the three cell types in our study (**Figure 2.1C**) emphasizes the importance of studying IAV in multiple physiologically relevant cell types to fully recapitulate virus biology during replication *in vivo*. Notably, 44/212 PPI factors were functionally classified as pro-viral and antiviral factors, and correspond to a hit rate of ~20.6% with at least one functional interaction for each of the 12 IAV bait proteins (**Figure 5.1G**). In comparison to other OMICS-based approaches, the high functional hit rate that we observe here suggests that by focusing on virus-host PPIs, interactomes present a discrete, manageable dataset enriched for targetable, actionable host factors.

By profiling global protein abundance and phosphorylation changes at peak IAV replication (**Figure 3.1B-D**), we computationally predicted changes in kinase activity for 13 kinases (**Figure 3.1F**). Most kinases show similar activity profiles across the three IAV strains, indicating the different strains may share common targets to rewire host signaling and response. These common targets may represent host signaling node vulnerabilities of IAV. For example, two kinases, MAPKAPK2 and MAPKAPK5, that increased in activity during infection by two IAV strains (**Figure 3.1F**) were necessary for efficient IAV infection (**Figure 5.1G**). 11 of the 13 kinases also show similar activity profiles during SARS-CoV-2 infection, including increased activity of MAPK signaling pathway members such as MAPK13 (p38 δ), MAP2K3 and MAP2K6,

and decreased activity of CDK2 (**Figure S5.1D**), highlighting similar signaling signatures of IAV and SARS-CoV-2 infection. Downregulation of CDK2 activity is also observed with infection by SARS-CoV (Surjit et al., 2006) and herpesviruses including Kaposi sarcoma herpesvirus (Izumiya et al., 2003) and herpes simplex virus type 1 (Ehmann et al., 2000). While siRNA knockdown of MAPK13, MAP2K3, MAP2K6 and CDK2 did not affect IAV infection (**Table S5.1**), host-directed compounds MAPK13-IN-1 (targeting MAPK13), Lestaurtinib (targeting MAP2K3, MAP2K6) and Dinaciclib (targeting CDK2) show antiviral activity against at least two strains of IAV (**Figure 6.1F,H**). This highlights the strength of pairing genetic and pharmacological perturbation to investigate functionality. These compounds affect replication of other viruses as well. For example, Dinaciclib and MAPK13-IN-1 show antiviral activity against SARS-CoV-2 infection (Bouhaddou et al., 2020), and Lestaurtinib shows antiviral activity against human adenovirus infection (Saha and Parks, 2021). Given the similar kinase activity profiles and antiviral activity of targeting compounds against multiple strains of IAV and other viruses, MAPK13, MAP2K3, MAP2K6 and CDK2 represent attractive potential candidates for pan-viral HDT.

By merging our PPI and PTM data, we identified phosphoregulated interactions for 10 IAV proteins (**Figure 3.1G**), including 9 phosphoregulated PPI factors that functionally affect IAV infection (**Figure 5.1G**). For example, TOMM22, AHNAK, ZC3HAV1, and INF2 interact with M2, NEP, NP and PB1, respectively, which are structural IAV proteins with important roles in viral entry and budding (M2), nuclear export of viral RNA (NEP), viral RNA encapsidation and trafficking (NP), and viral RNA replication (PB1). TOM22 phosphorylation at position serine 15 is increased during pH1N1 and H3N2 infection and decreased during H5N1 infection (**Figure 3.1G**). It has previously been shown that TOM22 is phosphorylated at serine 15 by casein kinase 2 (CSNK2), and this phosphorylation promotes mitophagy, a type of autophagy specific for degrading defective mitochondria (Kravic et al., 2018). Integrating H5N1 M2 interactors from

our study with transcriptomic (RNA-seq) and genome-wide siRNA screens of H3N2 and H5N1 IAV infection in human macrophages revealed a number of additional host proteins involved in mitophagy and mitochondrial homeostasis as important for IAV infection (Martin-Sancho et al., 2021). M2 interaction with serine 15-phosphorylated TOMM22 provides one potential molecular example of IAV co-opting mitophagy, a process likely essential for infection as TOM22 is identified in our study as a pro-viral factor of IAV (**Figure 5.1G**). It is also interesting to note that two of the phosphoregulated PPI factors that act as pro-viral factors of IAV infection are identified with pLOF phosphorylation variants in our whole exome sequencing data from an influenza patient cohort. We found that AHNAK serine 210 and INF2 serine 588 phosphorylation sites contain pLOF phosphorylation disruption mutations in patients with severe influenza disease (**Figure 4.1B, Table S4.1**), indicating they may also be involved in modulating host response to IAV infection and disease outcome. Further work that determines the mechanistic significance of specific phosphorylation sites on these interacting proteins could clarify how influenza exploits phosphorylation of host proteins and protein complexes to achieve essential processes for infection or modulation of host response.

Exome sequencing data from an influenza patient cohort profiled pLOF gene variants associated with severe disease that were also regulated at the protein level by IAV infection. pLOF genetic variants were identified for five PPI factors, 24 AB factors and 49 PH factors (**Table S4.1**). Interestingly, three of these five PPI factors (IRS2, RNH1, SEL1L) interact with IAV proteins that have known roles in modulating host innate immune response, viral pathogenicity and antigen response (NS1, PA-X, HA, respectively) (**Figure 2.2**). Future studies are merited to determine the mechanistic role of these proteins in cellular IAV infection and the role of pLOF variants of these proteins in driving severe influenza disease. Three of the five PPI factors also suppress or support IAV infection, and include: AHNAK (NEP), MYH14 (PA) and SEL1L (HA) (**Figure 5.1G**). Mapping phosphorylation disruption mutations found in patients with

severe influenza disease against the phosphorylation sites identified in our *ex vivo* PH data identified pLOF phosphorylation sites for six PPI factors including AHNAK, 75 AB factors and 146 PH factors (**Table S4.1**), and may indicate phosphorylation events important for triggering the cellular innate immune response. In patients with severe disease, 59 pLOF genes involved in immune signaling were statistically enriched in our proteomic data for changes in protein abundance (15 proteins) and phosphorylation (25 proteins with total 54 phosphorylation sites) during IAV infection (**Figure 4.1C**). Notably, nine pLOF genes involved in cytokine signaling, interleukin signaling and TLR signaling (including TLR3 signaling) decreased in protein abundance with pH1N1, H3N2 and H5N1 infection, highlighting these proteins as targets IAV modulates likely as an evasion strategy to favor infection. Inborn errors causing pLOF of TLR3 are identified in patients with severe viral disease, viral pneumonia or other complications from infection by a number of viral pathogens, including IAV (Lim et al., 2019), SARS-CoV-2 (Zhang et al., 2020), enterovirus (Chen et al., 2021) and herpes simplex virus 1 (Zhang et al., 2007). This highlights TLR3 as a critical pan-viral target for disease outcome, likely due to its role as a dsRNA sensor that aids in viral recognition, activation of innate immunity and induction of interferon (Lester and Li, 2014). Our study pinpoints other downstream members of the TLR3 signaling pathway that contain pLOF genetic variations in patients with severe influenza disease (**Table S4.1**), which could result in defective IAV restriction or clearance, and potentially represent a predisposition for increased disease severity. These factors may be targeted therapeutically to modulate the interferon response and improve disease outcome. Often, strategies to identify key disease-associated targets for biomarkers and drug therapies combine patient genetic association data with *in vivo* proteomic data from patient plasma samples, however, accessibility of plasma proteomic data has been limited by challenges in patient plasma sample processing, acquisition and analysis (Suhre et al., 2021). As new advances in plasma proteomics emerge to close this gap (Suhre et al., 2021), the combination of patient genetic data with *ex vivo* proteomic data presented here could also serve as a complementary

approach to identify potential clinically relevant molecular determinants of disease severity. Collectively, these data provide an exciting example of *ex vivo* proteomic data highlighting potential clinical molecular drivers of influenza disease severity.

Interestingly, four human protein interactors of two IAV proteins targeted in antiviral drug development (M2, HA) show promising evidence as broad spectrum HDT targets. These four host proteins functionally affect IAV infection (**Figure 5.1G**), and compounds targeting these four host factors show pan-IAV antiviral activity: Bafilomycin A1 targeting ATP6V1A (M2 interactor); Daunorubicin targeting ABCC1 (M2 interactor); NU7441 targeting PRKDC (M2 interactor and IAV-modulated kinase); and PACMA31 targeting P4HB (HA interactor) (**Figure 6.1B-E**). M2 is the IAV protein target of amantadine and rimantadine inhibitors, two classes of antivirals approved for clinical use that are now obsolete for IAV treatment due to virus resistance, particularly among 2009 pH1N1-like and H3N2 seasonal strains (Dong et al., 2015; Hayden and Hay, 1992). HA is one of the IAV proteins responsible for host cell entry by binding to sialic acid on epithelium cells, and is an attractive but challenging target for antiviral therapeutics due to high antigenic drift and shift (Koel et al., 2013; Lewis et al., 2016). There are no HA-targeting drugs currently available for clinical use. Recent antiviral strategies instead target human sialic acid to block HA binding and IAV entry. For example, sialic acid inhibitors were recently shown to target HA and have *ex vivo* antiviral efficacy (Chang et al., 2021). Antiviral compound Fludase (DAS181), a bacteria-derived sialidase fusion protein that cleaves sialic acid from epithelium cell surface to prevent IAV entry (Malakhov et al., 2006), enrolled its first patient in a Phase III clinical trial in 2019 and is moving towards FDA approval and clinical use. Fludase (DAS181) is a promising example of a host-directed strategy to successfully treat IAV infection. Here, we identified four host-directed pre-clinical and FDA-approved compounds that target three functional IAV M2 PPIs and one HA PPI, all of which have broad spectrum activity against pH1N1, H3N2 and H5N1 infection. None of these compounds are currently in

clinical trials or approved for use in treating influenza. Collectively, these four compounds represent potential alternative, host-directed targets for treating influenza disease.

IAV co-circulates seasonally with SARS-CoV-2 and emerging variants of concern, which represents a significant current and future challenge for public health. Human clinical data on IAV and SARS-CoV-2 co-infection during the 2020-2021 influenza season is limited, as public health measures instigated to limit the transmission of SARS-CoV-2, including shelter-in-place, masking and social distancing, largely limited the transmission of IAV (Olsen et al., 2020). However, a retrospective analysis determined a 49.8% co-infection rate of SARS-CoV-2 and IAV among patients early in the COVID-19 pandemic in Wuhan (Yue et al., 2020). Another study of a small patient cohort identified a high prevalence of individuals co-infected with H1N1-subtyped IAV and SARS-CoV-2, and a positive correlation between IAV co-infection and mortality rate (Alosaimi et al., 2021). In addition, in cell culture and in mice, IAV infection leads to increased susceptibility to SARS-CoV-2 co-infection and increased SARS-CoV-2 viral loads, and results in more severe lung damage, morbidity and mortality (Achdout et al., 2021; Bai et al., 2021a). This observation is specific to IAV in comparison to co-infection with other respiratory viruses (Bai et al., 2021a). IAV and SARS-CoV-2 present similar respiratory disease symptoms (Centers for Disease Control and Prevention, National Center for Immunization and Respiratory Diseases (NCIRD), 2022), and successful treatment currently relies on accurate detection and diagnosis, with pharmacological treatment specific to either virus. Identifying human proteins that are essential for both IAV and SARS-CoV-2 infection allows identification of common host targets for potential pan-respiratory virus HDT.

Here, we have taken a novel approach that combines genetic and pharmacological screening to identify host node vulnerabilities of both IAV and SARS-CoV-2. We challenged the 54 functional IAV PPI and PH factors by siRNA knockdown against SARS-CoV-2 infection, and identified two

human genes, COPB1 and AHNAK, that act as pro-viral factors in both IAV and SARS-CoV-2 infection (**Figure 5.1G**). A third gene, HNRNPUL2, acts as a pro-viral factor in IAV infection (**Figure 5.1G**) and falls just below our log₂ fold change cutoffs as a pro-viral factor for SARS-CoV-2 infection (**Table S5.1**). While we report these factors as IAV-human PPIs (M2-COPB1, NEP-AHNAK), to our knowledge, neither are reported as SARS-CoV-2-human PPIs. COPB1, a subunit of the coatamer complex I (COPI) that is associated with non-clathrin coated vesicles and involved in endosomal transport, was shown to be essential for IAV infection by other siRNA-based studies (Beylevel et al., 2018; Brass et al., 2009; Karlas et al., 2010), although to our knowledge its interaction with IAV M2 is novel. COPB1 was also shown to be required for infection of other RNA viruses, including vesicular stomatitis virus (Panda et al., 2011), and the secretory pathway was shown to promote SARS-CoV viral RNA replication and synthesis (Knoops et al., 2010). COPB1, as part of the COPI complex, and its role in endosomal transport may facilitate essential steps in viral RNA synthesis and trafficking or viral assembly for IAV and SARS-CoV-2. HNRNPUL2 interacts with IAV NP in our study, and is reported to interact with SARS-CoV-2 nucleocapsid (N) protein (Cai et al., 2021). IAV NP and SARS-CoV-2 N proteins share functional similarities; both proteins are viral RNA (vRNA)-binding proteins involved in encapsidation of vRNA and formation of viral ribonucleoproteins (vRNPs), vRNP trafficking, and virus replication (Bai et al., 2021b; Dou et al., 2018). NP and N proteins are abundantly expressed during infection, and evolutionarily conserved among related influenza viruses and coronaviruses, respectively, which make them attractive broad spectrum drug or vaccine targets (Bai et al., 2021b; Heiny et al., 2007; Hu et al., 2017; McGee and Huang, 2022). HNRNPUL2, a predominantly nuclear protein with RNA binding activity whose cellular function is under-characterized, likely facilitates NP and N in essential vRNA replication or vRNP trafficking functions. While we report these three genes as promising candidates for pan-viral HDT, future work is needed to determine the specific mechanisms by which these proteins affect IAV and SARS-CoV-2 infection.

Out of eight compounds that show antiviral activity against SARS-CoV-2 (Bouhaddou et al., 2020) and that target kinase pathways detected in our IAV phosphorylation data, three compounds show antiviral activity against at least two IAV strains: Gilteritinib, Pictilisib and MK-2206 (**Figure 6.1I-K**). As mentioned above, two additional compounds identified from our IAV PH data, Dinaciclib and MAPK13-IN-1, show antiviral activity against all three strains of IAV in our study (**Figure 6.1F,H**), and show antiviral activity against SARS-CoV-2 as reported in a previous study (Bouhaddou et al., 2020). In total, five compounds from our study show antiviral activity against multiple strains of IAV and SARS-CoV-2 infection. This highlights the power of leveraging and mining orthogonal phosphoproteomic analyses of infection by different respiratory viruses to identify novel pan-viral HDT. These five compounds target kinases of diverse pathways, and include FLT3/AXL (Gilteritinib), MAPK (MAPK13-IN-1), PI3K (Pictilisib), AKT (MK-2206) and CDK (Dinaciclib) signaling pathways (**Table S6.1**). None of these compounds are currently in clinical trials for influenza or COVID-19. While our results with Pictilisib (targeting PI3KCA, PI3KCD) and MK-2206 (targeting AKT1, AKT2, AKT3) are novel for IAV, other PI3K and AKT signaling inhibitors are in clinical trials for influenza (Planz, 2013). Collectively, these findings represent novel potential pan-respiratory antiviral HDT.

Several protein targets and therapeutics are identified by multiple orthogonal data in this study and warrant further investigation. While we have functionally characterized PPI and kinase factors with IAV infection, future work is needed to elucidate molecular mechanisms by which these pro-viral and antiviral factors affect specific stages of the virus life cycle and host antiviral response. For example, DNA damage-sensing protein kinase PRKDC is identified as an IAV M2 interactor (**Figure 2.2, Table S2.1**), and as a kinase with increased predicted activity during pH1N1 and H3N2, but not H5N1, infection in THP-1 cells (**Figure 3.1F**). PRKDC also has five sites that are almost all upregulated in phosphorylation with pH1N1, H3N2 and H5N1 infection

(**Figure 3.1G**). While siRNA knockdown of PRKDC increases IAV infection (**Figure 5.1G**), DNA-PK inhibitor NU7441 shows antiviral activity against pH1N1 and H3N2 infection, but not H5N1 infection (**Figure 6.1D**). It should be noted that while NU7441 is a potent and selective inhibitor for PRKDC, NU7441 also inhibits mTOR and PI3K in cell-free assays (NU7441 vendor information). Although NU7441 has not yet been tested in SARS-CoV-2 infection to our knowledge, a different PRKDC inhibitor did not affect SARS-CoV-2 infection (Bouhaddou et al., 2020). This highlights PRKDC as a highly regulated, functional protein specific to IAV infection, although its mechanism of action is unclear. PRKDC acts as a pattern recognition receptor for DNA, inducing the interferon response via activation of STING and TBK1, leading to IRF3 translocation and initiation of interferon production (Ferguson et al., 2012; Morchikh et al., 2017). IAV and other RNA viruses modulate and block DNA sensing, for example through the cGAS-STING innate immune sensing pathway, to promote infection (Webb and Fernandez-Sesma, 2022). IAV M2 has been shown to induce the release of mitochondrial DNA during infection and trigger the cGAS-dependent innate immune response, which is mitigated by IAV NS1 protein inhibiting DNA-mediated activation of interferon beta production (Moriyama et al., 2019). M2 interaction with PRKDC may sequester PRKDC and provide a second mechanism for mitigating and dampening DNA-mediated activation of interferon production to favor infection. siRNA knockdown of PRKDC may rescue viral infection (**Figure 5.1G**) by diminishing downstream interferon production. In our study, PRKDC is phosphorylated (**Figure 3.1G**) and has increased predicted activity with IAV infection (**Figure 3.1F**). Another phosphoproteomic study similarly identified PRKDC as a kinase activated upon infection with H3N2-subtype IAV in primary human macrophage cells (Söderholm et al., 2016). PRKDC may be involved in other, interferon-independent processes essential for IAV infection, which may be suppressed with NU7441 treatment. For example, PRKDC interacts with and phosphorylates host proteins involved in cell survival signaling including several AKT proteins (Anisenko et al., 2020), and M2 was shown to induce AKT-mTOR-dependent autophagy which promotes replication (Wang et

al., 2019). Further experiments are needed to determine if PRKDC can act as an upstream molecular regulator of autophagy with M2.

Another protein target highlighted by multiple orthogonal data in this study is AHNAK, a large, ~700kDa nuclear scaffold protein that interacts with IAV NEP and is highly phosphoregulated during IAV infection. AHNAK interacts with H5N1 IAV NEP above our PPI scoring thresholds, and with pH1N1 and H3N2 NEP below our thresholds (**Figure 2.2, Table S2.1**), indicating the interaction may not be strain-specific. The AHNAK-NEP interaction is specific to NHBE cells (**Figure S2.3, Table S2.1**). AHNAK has 11 sites that are differentially regulated in phosphorylation with pH1N1, H3N2 and H5N1 infection, with about half of the sites universally up- or downregulated and half of the sites regulated in strain-specific patterns (**Figure 3.1G**). Interestingly, AHNAK was identified with pLOF genetic variants in patients with severe influenza disease, and identified with pLOF phosphorylation mutations at site serine 210 in patients with severe influenza disease (**Figure 4.1B**), indicating AHNAK may play an important role in disease outcome. AHNAK is also a pan-respiratory virus gene target, as its knockdown decreases IAV infection and decreases SARS-CoV-2 infection (**Figure 5.1G**). AHNAK's role in IAV and SARS-CoV-2 infection is unknown, but may be tied to viral RNA export and/or virus budding. AHNAK regulates calcium signaling and downstream immune functions in T-cells (Matza et al., 2008). Calcium-dependent cell-cell contact formation has been shown to trigger AHNAK's phosphorylation by protein kinase B and relocalization outside the nucleus (Sussman et al., 2001), localization to the plasma membrane and complex formation with S100A10-Annexin 2 complex (Benaud et al., 2004). AHNAK has been proposed to coordinate cytoskeleton and membrane architecture changes together with S100A10-Annexin 2 complex (Benaud et al., 2004; Han et al., 2012; Jolly et al., 2014). This function is important in pathogen infection with bacterium *Salmonella*, where AHNAK is recruited to membrane ruffles and is required for infection (Jolly et al., 2014). IAV NEP facilitates export of viral ribonucleoprotein

(vRNP) complexes from the nucleus to the cytoplasm (Neumann et al., 2000; O'Neill et al., 1998), and facilitates virus formation and budding at the plasma membrane through its interaction with a membrane-embedded F-type proton-translocating ATPase (Gorai et al., 2012). AHNAK and IAV NEP perhaps coordinate cellular cytoskeletal and membrane remodeling for vRNP export and trafficking or IAV assembly and budding at the membrane. We found five additional human proteins involved in cytoskeletal regulation interact with NEP (**Figure 2.2**), and NEP PPIs are enriched in actin binding (**Figure 2.1F**), which support this model. Interestingly, we found that S100A10-Annexin 2 complex members (S100A10, ANXA2) interact with H5N1 PB1-F2 (**Figure 2.2**), indicating that NEP and PB1-F2 may work together by targeting AHNAK and S100A10-Annexin 2, respectively, to coordinate cytoskeleton and membrane remodeling for vRNP trafficking and virus budding. This would be a novel cellular role for PB1-F2. To date, no published studies identify AHNAK as an interactor of SARS-CoV-2 proteins, however AHNAK was profiled as an RNA binding protein whose RNA binding kinetics peak early in SARS-CoV-2 infection (Kamel et al., 2021). Our study uniquely identifies AHNAK as essential for SARS-CoV-2 infection, perhaps through AHNAK's interaction with viral RNA that may play a critical role in viral RNA production, trafficking or assembly during infection.

In summary, this study highlights the unique strength of an integrative systems biology approach to generate multi-dimensional data profiling IAV, and identify functional and druggable human proteins essential for IAV infection. By utilizing global proteomics, patient exome sequencing, functional genetics and pharmacological screening, we identify human gene targets and compounds that can be a starting point to develop pan-IAV host-directed antivirals and potential pan-respiratory virus host-directed antivirals (**Figure 5.1G, Figure 6.1B-K**). We hope the highly collaborative approach to data-driven target identification for host-directed therapies presented here can be employed to find additional pan-viral therapies and mechanisms beyond IAV and SARS-CoV-2 for other infectious diseases.

REFERENCES

- Achdout, H., Vitner, E.B., Politi, B., Melamed, S., Yahalom-Ronen, Y., Tamir, H., Erez, N., Avraham, R., Weiss, S., Cherry, L., et al. (2021). Increased lethality in influenza and SARS-CoV-2 coinfection is prevented by influenza immunity but not SARS-CoV-2 immunity. *Nat. Commun.* *12*, 5819.
- Adzhubei, I.A., Schmidt, S., Peshkin, L., Ramensky, V.E., Gerasimova, A., Bork, P., Kondrashov, A.S., and Sunyaev, S.R. (2010). A method and server for predicting damaging missense mutations. *Nat. Methods* *7*, 248–249.
- Alosaimi, B., Naeem, A., Hamed, M.E., Alkadi, H.S., Alanazi, T., Al Rehily, S.S., Almutairi, A.Z., and Zafar, A. (2021). Influenza co-infection associated with severity and mortality in COVID-19 patients. *Viol. J.* *18*, 127.
- Amorim, M.J., Bruce, E.A., Read, E.K.C., Foeglein, A., Mahen, R., Stuart, A.D., and Digard, P. (2011). A Rab11- and microtubule-dependent mechanism for cytoplasmic transport of influenza A virus viral RNA. *J. Virol.* *85*, 4143–4156.
- Anisenko, A., Kan, M., Shadrina, O., Brattseva, A., and Gottikh, M. (2020). Phosphorylation Targets of DNA-PK and Their Role in HIV-1 Replication. *Cells* *9*.
- Bai, L., Zhao, Y., Dong, J., Liang, S., Guo, M., Liu, X., Wang, X., Huang, Z., Sun, X., Zhang, Z., et al. (2021a). Coinfection with influenza A virus enhances SARS-CoV-2 infectivity. *Cell Res.* *31*, 395–403.
- Bai, Z., Cao, Y., Liu, W., and Li, J. (2021b). The SARS-CoV-2 Nucleocapsid Protein and Its Role in Viral Structure, Biological Functions, and a Potential Target for Drug or Vaccine Mitigation. *Viruses* *13*.
- Batra, J., Hultquist, J.F., Liu, D., Shtanko, O., Von Dollen, J., Satkamp, L., Jang, G.M., Luthra, P., Schwarz, T.M., Small, G.I., et al. (2018). Protein Interaction Mapping Identifies RBBP6 as a Negative Regulator of Ebola Virus Replication. *Cell* *175*, 1917–1930.e13.

Benaud, C., Gentil, B.J., Assard, N., Court, M., Garin, J., Delphin, C., and Baudier, J. (2004). AHNAK interaction with the annexin 2/S100A10 complex regulates cell membrane cytoarchitecture. *J. Cell Biol.* 164, 133–144.

Beyleveld, G., Chin, D.J., Moreno Del Olmo, E., Carter, J., Najera, I., Cillóniz, C., and Shaw, M.L. (2018). Nucleolar Relocalization of RBM14 by Influenza A Virus NS1 Protein. *mSphere* 3.

Bojkova, D., Klann, K., Koch, B., Widera, M., Krause, D., Ciesek, S., Cinatl, J., and Münch, C. (2020). Proteomics of SARS-CoV-2-infected host cells reveals therapy targets. *Nature* 583, 469–472.

Bouhaddou, M., Memon, D., Meyer, B., White, K.M., Rezelj, V.V., Correa Marrero, M., Polacco, B.J., Melnyk, J.E., Ulferts, S., Kaake, R.M., et al. (2020). The Global Phosphorylation Landscape of SARS-CoV-2 Infection. *Cell* 182, 685–712.e19.

Brass, A.L., Huang, I.-C., Benita, Y., John, S.P., Krishnan, M.N., Feeley, E.M., Ryan, B.J., Weyer, J.L., van der Weyden, L., Fikrig, E., et al. (2009). The IFITM proteins mediate cellular resistance to influenza A H1N1 virus, West Nile virus, and dengue virus. *Cell* 139, 1243–1254.

Byrn, R.A., Jones, S.M., Bennett, H.B., Bral, C., Clark, M.P., Jacobs, M.D., Kwong, A.D., Ledebor, M.W., Leeman, J.R., McNeil, C.F., et al. (2015). Preclinical activity of VX-787, a first-in-class, orally bioavailable inhibitor of the influenza virus polymerase PB2 subunit. *Antimicrob. Agents Chemother.* 59, 1569–1582.

Cai, T., Yu, Z., Wang, Z., Liang, C., and Richard, S. (2021). Arginine methylation of SARS-Cov-2 nucleocapsid protein regulates RNA binding, its ability to suppress stress granule formation, and viral replication. *J. Biol. Chem.* 297, 100821.

Casado, P., Rodriguez-Prados, J.-C., Cosulich, S.C., Guichard, S., Vanhaesebroeck, B., Joel, S., and Cutillas, P.R. (2013). Kinase-substrate enrichment analysis provides insights into the heterogeneity of signaling pathway activation in leukemia cells. *Sci. Signal.* 6, rs6.

Cele, S., Jackson, L., Khan, K., Khoury, D.S., Moyo-Gwete, T., Tegally, H., Scheepers, C., Amoako, D., Karim, F., Bernstein, M., et al. (2021). SARS-CoV-2 Omicron has extensive but

incomplete escape of Pfizer BNT162b2 elicited neutralization and requires ACE2 for infection. medRxiv.

Centers for Disease Control and Prevention (CDC) (2004). Update: influenza activity--United States, 2003-04 season. *MMWR Morb. Mortal. Wkly. Rep.* 53, 284–287.

Centers for Disease Control and Prevention, National Center for Immunization and Respiratory Diseases (NCIRD) (2021a). Types of Influenza Viruses.

<https://www.cdc.gov/flu/about/viruses/types.htm> (accessed 26 July 2021).

Centers for Disease Control and Prevention, National Center for Immunization and Respiratory Diseases (NCIRD) (2021b). CDC Seasonal Flu Vaccine Effectiveness Studies.

<https://www.cdc.gov/flu/vaccines-work/effectiveness-studies.htm> (accessed 26 July 2021).

Centers for Disease Control and Prevention, National Center for Immunization and Respiratory Diseases (NCIRD) (2022). Similarities and Differences between Flu and COVID-19.

<https://www.cdc.gov/flu/symptoms/flu-vs-covid19.htm> (accessed 12 November 2021).

Chang, Y.-J., Yeh, C.-Y., Cheng, J.-C., Huang, Y.-Q., Hsu, K.-C., Lin, Y.-F., and Lu, C.-H. (2021). Potent sialic acid inhibitors that target influenza A virus hemagglutinin. *Sci. Rep.* 11, 8637.

Chanput, W., Mes, J.J., and Wichers, H.J. (2014). THP-1 cell line: an in vitro cell model for immune modulation approach. *Int. Immunopharmacol.* 23, 37–45.

Chen, J., Jing, H., Martin-Nalda, A., Bastard, P., Rivière, J.G., Liu, Z., Colobran, R., Lee, D., Tung, W., Manry, J., et al. (2021). Inborn errors of TLR3- or MDA5-dependent type I IFN immunity in children with enterovirus rhombencephalitis. *J. Exp. Med.* 218.

Chen, W., Calvo, P.A., Malide, D., Gibbs, J., Schubert, U., Bacik, I., Basta, S., O'Neill, R., Schickli, J., Palese, P., et al. (2001). A novel influenza A virus mitochondrial protein that induces cell death. *Nat. Med.* 7, 1306–1312.

Choi, M., Chang, C.-Y., Clough, T., Broudy, D., Killeen, T., MacLean, B., and Vitek, O. (2014). MSstats: an R package for statistical analysis of quantitative mass spectrometry-based proteomic experiments. *Bioinformatics* 30, 2524–2526.

Chu, D.K.W., Pan, Y., Cheng, S.M.S., Hui, K.P.Y., Krishnan, P., Liu, Y., Ng, D.Y.M., Wan, C.K.C., Yang, P., Wang, Q., et al. (2020). Molecular Diagnosis of a Novel Coronavirus (2019-nCoV) Causing an Outbreak of Pneumonia. *Clin. Chem.* 66, 549–555.

Commissioners of the Lancet COVID-19 Commission. Task Force Chairs and members of the Lancet COVID-19 Commission, Commission Secretariat and Staff of the Lancet COVID-19 Commission, and Commissioners of the Lancet COVID-19 Commission (2021). Priorities for the COVID-19 pandemic at the start of 2021: statement of the Lancet COVID-19 Commission. *Lancet* 397, 947–950.

Cox, J., and Mann, M. (2008). MaxQuant enables high peptide identification rates, individualized p.p.b.-range mass accuracies and proteome-wide protein quantification. *Nat. Biotechnol.* 26, 1367–1372.

Crooks, G.E., Hon, G., Chandonia, J.-M., and Brenner, S.E. (2004). WebLogo: a sequence logo generator. *Genome Res.* 14, 1188–1190.

Daigneault, M., Preston, J.A., Marriott, H.M., Whyte, M.K.B., and Dockrell, D.H. (2010). The identification of markers of macrophage differentiation in PMA-stimulated THP-1 cells and monocyte-derived macrophages. *PLoS One* 5, e8668.

Daniels, R., Kurowski, B., Johnson, A.E., and Hebert, D.N. (2003). N-linked glycans direct the cotranslational folding pathway of influenza hemagglutinin. *Mol. Cell* 11, 79–90.

Davies, N.G., Abbott, S., Barnard, R.C., Jarvis, C.I., Kucharski, A.J., Munday, J.D., Pearson, C.A.B., Russell, T.W., Tully, D.C., Washburne, A.D., et al. (2021). Estimated transmissibility and impact of SARS-CoV-2 lineage B.1.1.7 in England. *Science* 372.

Dawood, F.S., Iuliano, A.D., Reed, C., Meltzer, M.I., Shay, D.K., Cheng, P.-Y., Bandaranayake, D., Breiman, R.F., Brooks, W.A., Buchy, P., et al. (2012). Estimated global mortality associated

with the first 12 months of 2009 pandemic influenza A H1N1 virus circulation: a modelling study. *Lancet Infect. Dis.* 12, 687–695.

Diep, J., Ooi, Y.S., Wilkinson, A.W., Peters, C.E., Foy, E., Johnson, J.R., Zengel, J., Ding, S., Weng, K.-F., Laufman, O., et al. (2019). Enterovirus pathogenesis requires the host methyltransferase SETD3. *Nat Microbiol* 4, 2523–2537.

Dong, G., Peng, C., Luo, J., Wang, C., Han, L., Wu, B., Ji, G., and He, H. (2015). Adamantane-resistant influenza A viruses in the world (1902-2013): frequency and distribution of M2 gene mutations. *PLoS One* 10, e0119115.

Dornfeld, D., Dudek, A.H., Vausselin, T., Günther, S.C., Hultquist, J.F., Giese, S., Khokhlova-Cubberley, D., Chew, Y.C., Pache, L., Krogan, N.J., et al. (2018). SMARCA2-regulated host cell factors are required for MxA restriction of influenza A viruses. *Sci. Rep.* 8, 2092.

Dou, D., Revol, R., Östbye, H., Wang, H., and Daniels, R. (2018). Influenza A Virus Cell Entry, Replication, Virion Assembly and Movement. *Front. Immunol.* 9, 1581.

Eckhardt, M., Hultquist, J.F., Kaake, R.M., Hüttenhain, R., and Krogan, N.J. (2020). A systems approach to infectious disease. *Nat. Rev. Genet.* 21, 339–354.

Ehmann, G.L., McLean, T.I., and Bachenheimer, S.L. (2000). Herpes simplex virus type 1 infection imposes a G(1)/S block in asynchronously growing cells and prevents G(1) entry in quiescent cells. *Virology* 267, 335–349.

Ehrhardt, C., Marjuki, H., Wolff, T., Nürnberg, B., Planz, O., Pleschka, S., and Ludwig, S. (2006). Bivalent role of the phosphatidylinositol-3-kinase (PI3K) during influenza virus infection and host cell defence. *Cell. Microbiol.* 8, 1336–1348.

Ehrhardt, C., Wolff, T., Pleschka, S., Planz, O., Beermann, W., Bode, J.G., Schmolke, M., and Ludwig, S. (2007). Influenza A virus NS1 protein activates the PI3K/Akt pathway to mediate antiapoptotic signaling responses. *J. Virol.* 81, 3058–3067.

Eisfeld, A.J., Neumann, G., and Kawaoka, Y. (2014). Influenza A virus isolation, culture and identification. *Nat. Protoc.* 9, 2663–2681.

Ferguson, B.J., Mansur, D.S., Peters, N.E., Ren, H., and Smith, G.L. (2012). DNA-PK is a DNA sensor for IRF-3-dependent innate immunity. *Elife* 1, e00047.

Finberg, R.W., Lanno, R., Anderson, D., Fleischhackl, R., van Duijnhoven, W., Kauffman, R.S., Kosoglou, T., Vingerhoets, J., and Leopold, L. (2019). Phase 2b Study of Pimodivir (JNJ-63623872) as Monotherapy or in Combination With Oseltamivir for Treatment of Acute Uncomplicated Seasonal Influenza A: TOPAZ Trial. *J. Infect. Dis.* 219, 1026–1034.

Garten, R.J., Davis, C.T., Russell, C.A., Shu, B., Lindstrom, S., Balish, A., Sessions, W.M., Xu, X., Skepner, E., Deyde, V., et al. (2009). Antigenic and genetic characteristics of swine-origin 2009 A(H1N1) influenza viruses circulating in humans. *Science* 325, 197–201.

Gerlt, V., Mayr, J., Del Sarto, J., Ludwig, S., and Boergeling, Y. (2021). Cellular Protein Phosphatase 2A Regulates Cell Survival Mechanisms in Influenza A Virus Infection. *Int. J. Mol. Sci.* 22.

Gibson, D.G., Young, L., Chuang, R.-Y., Venter, J.C., Hutchison, C.A., 3rd, and Smith, H.O. (2009). Enzymatic assembly of DNA molecules up to several hundred kilobases. *Nat. Methods* 6, 343–345.

Giurgiu, M., Reinhard, J., Brauner, B., Dunger-Kaltenbach, I., Fobo, G., Frishman, G., Montrone, C., and Ruepp, A. (2019). CORUM: the comprehensive resource of mammalian protein complexes-2019. *Nucleic Acids Res.* 47, D559–D563.

Goldhill, D.H., Te Velthuis, A.J.W., Fletcher, R.A., Langat, P., Zambon, M., Lackenby, A., and Barclay, W.S. (2018). The mechanism of resistance to favipiravir in influenza. *Proc. Natl. Acad. Sci. U. S. A.* 115, 11613–11618.

Gorai, T., Goto, H., Noda, T., Watanabe, T., Kozuka-Hata, H., Oyama, M., Takano, R., Neumann, G., Watanabe, S., and Kawaoka, Y. (2012). F1Fo-ATPase, F-type proton-translocating ATPase, at the plasma membrane is critical for efficient influenza virus budding. *Proc. Natl. Acad. Sci. U. S. A.* 109, 4615–4620.

Gordon, D.E., Hiatt, J., Bouhaddou, M., Rezelj, V.V., Ulferts, S., Braberg, H., Jureka, A.S., Obernier, K., Guo, J.Z., Batra, J., et al. (2020a). Comparative host-coronavirus protein interaction networks reveal pan-viral disease mechanisms. *Science* 370.

Gordon, D.E., Jang, G.M., Bouhaddou, M., Xu, J., Obernier, K., White, K.M., O'Meara, M.J., Rezelj, V.V., Guo, J.Z., Swaney, D.L., et al. (2020b). A SARS-CoV-2 protein interaction map reveals targets for drug repurposing. *Nature* 583, 459–468.

Gubareva, L.V., Mishin, V.P., Patel, M.C., Chesnokov, A., Nguyen, H.T., De La Cruz, J., Spencer, S., Campbell, A.P., Sinner, M., Reid, H., et al. (2019). Assessing baloxavir susceptibility of influenza viruses circulating in the United States during the 2016/17 and 2017/18 seasons. *Euro Surveill.* 24.

Hale, B.G., Steel, J., Medina, R.A., Manicassamy, B., Ye, J., Hickman, D., Hai, R., Schmolke, M., Lowen, A.C., Perez, D.R., et al. (2010). Inefficient control of host gene expression by the 2009 pandemic H1N1 influenza A virus NS1 protein. *J. Virol.* 84, 6909–6922.

Han, W.-Q., Xia, M., Xu, M., Boini, K.M., Ritter, J.K., Li, N.-J., and Li, P.-L. (2012). Lysosome fusion to the cell membrane is mediated by the dysferlin C2A domain in coronary arterial endothelial cells. *J. Cell Sci.* 125, 1225–1234.

Hara, K., Schmidt, F.I., Crow, M., and Brownlee, G.G. (2006). Amino acid residues in the N-terminal region of the PA subunit of influenza A virus RNA polymerase play a critical role in protein stability, endonuclease activity, cap binding, and virion RNA promoter binding. *J. Virol.* 80, 7789–7798.

Hayden, F.G., and Hay, A.J. (1992). Emergence and transmission of influenza A viruses resistant to amantadine and rimantadine. *Curr. Top. Microbiol. Immunol.* 176, 119–130.

Heaton, N.S., Moshkina, N., Fenouil, R., Gardner, T.J., Aguirre, S., Shah, P.S., Zhao, N., Manganaro, L., Hultquist, J.F., Noel, J., et al. (2016). Targeting Viral Proteostasis Limits Influenza Virus, HIV, and Dengue Virus Infection. *Immunity* 44, 46–58.

Heiny, A.T., Miotto, O., Srinivasan, K.N., Khan, A.M., Zhang, G.L., Brusica, V., Tan, T.W., and August, J.T. (2007). Evolutionarily conserved protein sequences of influenza A viruses, avian and human, as vaccine targets. *PLoS One* 2, e1190.

Hekman, R.M., Hume, A.J., Goel, R.K., Abo, K.M., Huang, J., Blum, B.C., Werder, R.B., Suder, E.L., Paul, I., Phanse, S., et al. (2020). Actionable Cytopathogenic Host Responses of Human Alveolar Type 2 Cells to SARS-CoV-2. *Mol. Cell* 80, 1104–1122.e9.

Herfst, S., Schrauwen, E.J.A., Linster, M., Chutinimitkul, S., de Wit, E., Munster, V.J., Sorrell, E.M., Bestebroer, T.M., Burke, D.F., Smith, D.J., et al. (2012). Airborne transmission of influenza A/H5N1 virus between ferrets. *Science* 336, 1534–1541.

Hernandez-Armenta, C., Ochoa, D., Gonçalves, E., Saez-Rodriguez, J., and Beltrao, P. (2017). Benchmarking substrate-based kinase activity inference using phosphoproteomic data. *Bioinformatics* 33, 1845–1851.

Hornbeck, P.V., Zhang, B., Murray, B., Kornhauser, J.M., Latham, V., and Skrzypek, E. (2015). PhosphoSitePlus, 2014: mutations, PTMs and recalibrations. *Nucleic Acids Res.* 43, D512–D520.

Hu, Y., Sneyd, H., Dekant, R., and Wang, J. (2017). Influenza A Virus Nucleoprotein: A Highly Conserved Multi-Functional Viral Protein as a Hot Antiviral Drug Target. *Curr. Top. Med. Chem.* 17, 2271–2285.

Huang, X., Liu, T., Muller, J., Levandowski, R.A., and Ye, Z. (2001). Effect of influenza virus matrix protein and viral RNA on ribonucleoprotein formation and nuclear export. *Virology* 287, 405–416.

Hussain, M., Galvin, H.D., Haw, T.Y., Nutsford, A.N., and Husain, M. (2017). Drug resistance in influenza A virus: the epidemiology and management. *Infect. Drug Resist.* 10, 121–134.

Imai, M., Watanabe, T., Hatta, M., Das, S.C., Ozawa, M., Shinya, K., Zhong, G., Hanson, A., Katsura, H., Watanabe, S., et al. (2012). Experimental adaptation of an influenza H5 HA confers

respiratory droplet transmission to a reassortant H5 HA/H1N1 virus in ferrets. *Nature* 486, 420–428.

Izumiya, Y., Lin, S.-F., Ellison, T.J., Levy, A.M., Mayeur, G.L., Izumiya, C., and Kung, H.-J. (2003). Cell cycle regulation by Kaposi's sarcoma-associated herpesvirus K-bZIP: direct interaction with cyclin-CDK2 and induction of G1 growth arrest. *J. Virol.* 77, 9652–9661.

Jäger, S., Cimermancic, P., Gulbahce, N., Johnson, J.R., McGovern, K.E., Clarke, S.C., Shales, M., Mercenne, G., Pache, L., Li, K., et al. (2011). Global landscape of HIV-human protein complexes. *Nature* 481, 365–370.

Jagger, B.W., Wise, H.M., Kash, J.C., Walters, K.-A., Wills, N.M., Xiao, Y.-L., Dunfee, R.L., Schwartzman, L.M., Ozinsky, A., Bell, G.L., et al. (2012). An overlapping protein-coding region in influenza A virus segment 3 modulates the host response. *Science* 337, 199–204.

Johnson, N.P.A.S., and Mueller, J. (2002). Updating the accounts: global mortality of the 1918–1920 “Spanish” influenza pandemic. *Bull. Hist. Med.* 76, 105–115.

Jolly, C., Winfree, S., Hansen, B., and Steele-Mortimer, O. (2014). The Annexin A2/p11 complex is required for efficient invasion of *Salmonella Typhimurium* in epithelial cells. *Cell. Microbiol.* 16, 64–77.

Kainov, D.E., Müller, K.H., Theisen, L.L., Anastasina, M., Kaloinen, M., and Muller, C.P. (2011). Differential effects of NS1 proteins of human pandemic H1N1/2009, avian highly pathogenic H5N1, and low pathogenic H5N2 influenza A viruses on cellular pre-mRNA polyadenylation and mRNA translation. *J. Biol. Chem.* 286, 7239–7247.

Kamel, W., Noerenberg, M., Cerikan, B., Chen, H., Järvelin, A.I., Kammoun, M., Lee, J.Y., Shuai, N., Garcia-Moreno, M., Andrejeva, A., et al. (2021). Global analysis of protein-RNA interactions in SARS-CoV-2-infected cells reveals key regulators of infection. *Mol. Cell* 81, 2851–2867.e7.

Karlas, A., Machuy, N., Shin, Y., Pleissner, K.-P., Artarini, A., Heuer, D., Becker, D., Khalil, H., Ogilvie, L.A., Hess, S., et al. (2010). Genome-wide RNAi screen identifies human host factors crucial for influenza virus replication. *Nature* 463, 818–822.

Kaufmann, S.H.E., Dorhoi, A., Hotchkiss, R.S., and Bartenschlager, R. (2018). Host-directed therapies for bacterial and viral infections. *Nat. Rev. Drug Discov.* 17, 35–56.

Kelly, H., Peck, H.A., Laurie, K.L., Wu, P., Nishiura, H., and Cowling, B.J. (2011). The age-specific cumulative incidence of infection with pandemic influenza H1N1 2009 was similar in various countries prior to vaccination. *PLoS One* 6, e21828.

Klemm, C., Boergeling, Y., Ludwig, S., and Ehrhardt, C. (2018). Immunomodulatory Nonstructural Proteins of Influenza A Viruses. *Trends Microbiol.* 26, 624–636.

Knoops, K., Swett-Tapia, C., van den Worm, S.H.E., Te Velthuis, A.J.W., Koster, A.J., Mommaas, A.M., Snijder, E.J., and Kikkert, M. (2010). Integrity of the early secretory pathway promotes, but is not required for, severe acute respiratory syndrome coronavirus RNA synthesis and virus-induced remodeling of endoplasmic reticulum membranes. *J. Virol.* 84, 833–846.

Koel, B.F., Burke, D.F., Bestebroer, T.M., van der Vliet, S., Zondag, G.C.M., Vervaet, G., Skepner, E., Lewis, N.S., Spronken, M.I.J., Russell, C.A., et al. (2013). Substitutions near the receptor binding site determine major antigenic change during influenza virus evolution. *Science* 342, 976–979.

König, R., Stertz, S., Zhou, Y., Inoue, A., Hoffmann, H.-H., Bhattacharyya, S., Alamares, J.G., Tscherne, D.M., Ortigoza, M.B., Liang, Y., et al. (2010). Human host factors required for influenza virus replication. *Nature* 463, 813–817.

Kravic, B., Harbauer, A.B., Romanello, V., Simeone, L., Vögtle, F.-N., Kaiser, T., Straubinger, M., Huraskin, D., Böttcher, M., Cerqua, C., et al. (2018). In mammalian skeletal muscle, phosphorylation of TOMM22 by protein kinase CSNK2/CK2 controls mitophagy. *Autophagy* 14, 311–335.

Kukol, A., and Hughes, D.J. (2014). Large-scale analysis of influenza A virus nucleoprotein sequence conservation reveals potential drug-target sites. *Virology* 454-455, 40–47.

Kumar, N., Sharma, S., Kumar, R., Tripathi, B.N., Barua, S., Ly, H., and Rouse, B.T. (2020). Host-Directed Antiviral Therapy. *Clin. Microbiol. Rev.* 33.

Law, G.L., Korth, M.J., Benecke, A.G., and Katze, M.G. (2013). Systems virology: host-directed approaches to viral pathogenesis and drug targeting. *Nat. Rev. Microbiol.* 11, 455–466.

Lee, S., Emond, M.J., Bamshad, M.J., Barnes, K.C., Rieder, M.J., Nickerson, D.A., NHLBI GO Exome Sequencing Project—ESP Lung Project Team, Christiani, D.C., Wurfel, M.M., and Lin, X. (2012). Optimal unified approach for rare-variant association testing with application to small-sample case-control whole-exome sequencing studies. *Am. J. Hum. Genet.* 91, 224–237.

Lester, S.N., and Li, K. (2014). Toll-like receptors in antiviral innate immunity. *J. Mol. Biol.* 426, 1246–1264.

Lewis, N.S., Russell, C.A., Langat, P., Anderson, T.K., Berger, K., Bielejec, F., Burke, D.F., Dudas, G., Fonville, J.M., Fouchier, R.A., et al. (2016). The global antigenic diversity of swine influenza A viruses. *Elife* 5, e12217.

Li, H., and Durbin, R. (2009). Fast and accurate short read alignment with Burrows-Wheeler transform. *Bioinformatics* 25, 1754–1760.

Li, M., Johnson, J.R., Truong, B., Kim, G., Weinbren, N., Dittmar, M., Shah, P.S., Von Dollen, J., Newton, B.W., Jang, G.M., et al. (2019). Identification of antiviral roles for the exon-junction complex and nonsense-mediated decay in flaviviral infection. *Nat Microbiol* 4, 985–995.

Lim, H.K., Huang, S.X.L., Chen, J., Kerner, G., Gilliaux, O., Bastard, P., Dobbs, K., Hernandez, N., Goudin, N., Hasek, M.L., et al. (2019). Severe influenza pneumonitis in children with inherited TLR3 deficiency. *J. Exp. Med.* 216, 2038–2056.

Lin, A.E., Greco, T.M., Döhner, K., Sodeik, B., and Cristea, I.M. (2013). A proteomic perspective of inbuilt viral protein regulation: pUL46 tegument protein is targeted for degradation by ICP0 during herpes simplex virus type 1 infection. *Mol. Cell. Proteomics* 12, 3237–3252.

Liu, S., Liao, Y., Chen, B., Chen, Y., Yu, Z., Wei, H., Zhang, L., Huang, S., Rothman, P.B., Gao, G.F., et al. (2021). Critical role of Syk-dependent STAT1 activation in innate antiviral immunity. *Cell Rep.* 34, 108627.

Liu, Y., Myrvang, H.K., and Dekker, L.V. (2015). Annexin A2 complexes with S100 proteins: structure, function and pharmacological manipulation. *Br. J. Pharmacol.* 172, 1664–1676.

Lu, Y., Wambach, M., Katze, M.G., and Krug, R.M. (1995). Binding of the influenza virus NS1 protein to double-stranded RNA inhibits the activation of the protein kinase that phosphorylates the eIF-2 translation initiation factor. *Virology* 214, 222–228.

Lum, K.K., and Cristea, I.M. (2016). Proteomic approaches to uncovering virus-host protein interactions during the progression of viral infection. *Expert Rev. Proteomics* 13, 325–340.

Malakhov, M.P., Aschenbrenner, L.M., Smee, D.F., Wandersee, M.K., Sidwell, R.W., Gubareva, L.V., Mishin, V.P., Hayden, F.G., Kim, D.H., Ing, A., et al. (2006). Sialidase fusion protein as a novel broad-spectrum inhibitor of influenza virus infection. *Antimicrob. Agents Chemother.* 50, 1470–1479.

Martin, K., and Helenius, A. (1991). Nuclear transport of influenza virus ribonucleoproteins: the viral matrix protein (M1) promotes export and inhibits import. *Cell* 67, 117–130.

Martin-Sancho, L., Tripathi, S., Rodriguez-Frandsen, A., Pache, L., Sanchez-Aparicio, M., McGregor, M.J., Haas, K.M., Swaney, D.L., Nguyen, T.T., Mamede, J.I., et al. (2021). Restriction factor compendium for influenza A virus reveals a mechanism for evasion of autophagy. *Nat Microbiol* 6, 1319–1333.

Mathieu, E., Ritchie, H., Ortiz-Ospina, E., Roser, M., Hasell, J., Appel, C., Giattino, C., and Rodés-Guirao, L. (2021). A global database of COVID-19 vaccinations. *Nat Hum Behav* 5, 947–953.

Matza, D., Badou, A., Kobayashi, K.S., Goldsmith-Pestana, K., Masuda, Y., Komuro, A., McMahon-Pratt, D., Marchesi, V.T., and Flavell, R.A. (2008). A scaffold protein, AHNAK1, is required for calcium signaling during T cell activation. *Immunity* 28, 64–74.

Matza, D., Badou, A., Jha, M.K., Willinger, T., Antov, A., Sanjabi, S., Kobayashi, K.S., Marchesi, V.T., and Flavell, R.A. (2009). Requirement for AHNAK1-mediated calcium signaling during T lymphocyte cytolysis. *Proc. Natl. Acad. Sci. U. S. A.* *106*, 9785–9790.

McGee, M.C., and Huang, W. (2022). Evolutionary conservation and positive selection of influenza A nucleoprotein CTL epitopes for universal vaccination. *J. Med. Virol.*

McLaren, W., Gil, L., Hunt, S.E., Riat, H.S., Ritchie, G.R.S., Thormann, A., Flicek, P., and Cunningham, F. (2016). The Ensembl Variant Effect Predictor. *Genome Biol.* *17*, 122.

Medina, R.A., and García-Sastre, A. (2011). Influenza A viruses: new research developments. *Nat. Rev. Microbiol.* *9*, 590–603.

Min, J.-Y., and Krug, R.M. (2006). The primary function of RNA binding by the influenza A virus NS1 protein in infected cells: Inhibiting the 2'-5' oligo (A) synthetase/RNase L pathway. *Proc. Natl. Acad. Sci. U. S. A.* *103*, 7100–7105.

Mlcochova, P., Kemp, S.A., Dhar, M.S., Papa, G., Meng, B., Ferreira, I.A.T.M., Datir, R., Collier, D.A., Albecka, A., Singh, S., et al. (2021). SARS-CoV-2 B.1.617.2 Delta variant replication and immune evasion. *Nature* *599*, 114–119.

Morchikh, M., Cribier, A., Raffel, R., Amraoui, S., Cau, J., Severac, D., Dubois, E., Schwartz, O., Bennasser, Y., and Benkirane, M. (2017). HEXIM1 and NEAT1 Long Non-coding RNA Form a Multi-subunit Complex that Regulates DNA-Mediated Innate Immune Response. *Mol. Cell* *67*, 387–399.e5.

Moriyama, M., Koshihara, T., and Ichinohe, T. (2019). Influenza A virus M2 protein triggers mitochondrial DNA-mediated antiviral immune responses. *Nat. Commun.* *10*, 4624.

Nemeroff, M.E., Barabino, S.M., Li, Y., Keller, W., and Krug, R.M. (1998). Influenza virus NS1 protein interacts with the cellular 30 kDa subunit of CPSF and inhibits 3' end formation of cellular pre-mRNAs. *Mol. Cell* *1*, 991–1000.

Neumann, G., Hughes, M.T., and Kawaoka, Y. (2000). Influenza A virus NS2 protein mediates vRNP nuclear export through NES-independent interaction with hCRM1. *EMBO J.* 19, 6751–6758.

Noah, D.L., Twu, K.Y., and Krug, R.M. (2003). Cellular antiviral responses against influenza A virus are countered at the posttranscriptional level by the viral NS1A protein via its binding to a cellular protein required for the 3' end processing of cellular pre-mRNAs. *Virology* 307, 386–395.

Olsen, S.J., Azziz-Baumgartner, E., Budd, A.P., Brammer, L., Sullivan, S., Pineda, R.F., Cohen, C., and Fry, A.M. (2020). Decreased Influenza Activity During the COVID-19 Pandemic - United States, Australia, Chile, and South Africa, 2020. *MMWR Morb. Mortal. Wkly. Rep.* 69, 1305–1309.

Omoto, S., Speranzini, V., Hashimoto, T., Noshi, T., Yamaguchi, H., Kawai, M., Kawaguchi, K., Uehara, T., Shishido, T., Naito, A., et al. (2018). Characterization of influenza virus variants induced by treatment with the endonuclease inhibitor baloxavir marboxil. *Sci. Rep.* 8, 9633.

O'Neill, R.E., Talon, J., and Palese, P. (1998). The influenza virus NEP (NS2 protein) mediates the nuclear export of viral ribonucleoproteins. *EMBO J.* 17, 288–296.

Panda, D., Das, A., Dinh, P.X., Subramaniam, S., Nayak, D., Barrows, N.J., Pearson, J.L., Thompson, J., Kelly, D.L., Ladunga, I., et al. (2011). RNAi screening reveals requirement for host cell secretory pathway in infection by diverse families of negative-strand RNA viruses. *Proc. Natl. Acad. Sci. U. S. A.* 108, 19036–19041.

Park, M.-S., Steel, J., García-Sastre, A., Swayne, D., and Palese, P. (2006). Engineered viral vaccine constructs with dual specificity: avian influenza and Newcastle disease. *Proc. Natl. Acad. Sci. U. S. A.* 103, 8203–8208.

Perez-Riverol, Y., Csordas, A., Bai, J., Bernal-Llinares, M., Hewapathirana, S., Kundu, D.J., Inuganti, A., Griss, J., Mayer, G., Eisenacher, M., et al. (2019). The PRIDE database and

related tools and resources in 2019: improving support for quantification data. *Nucleic Acids Res.* 47, D442–D450.

Perwitasari, O., Yan, X., O'Donnell, J., Johnson, S., and Tripp, R.A. (2015). Repurposing Kinase Inhibitors as Antiviral Agents to Control Influenza A Virus Replication. *Assay Drug Dev. Technol.* 13, 638–649.

Petherick, K.J., Conway, O.J.L., Mpamhanga, C., Osborne, S.A., Kamal, A., Saxty, B., and Ganley, I.G. (2015). Pharmacological inhibition of ULK1 kinase blocks mammalian target of rapamycin (mTOR)-dependent autophagy. *J. Biol. Chem.* 290, 11376–11383.

Phillips, N. (2021). The coronavirus is here to stay - here's what that means. *Nature* 590, 382–384.

Planz, O. (2013). Development of cellular signaling pathway inhibitors as new antivirals against influenza. *Antiviral Res.* 98, 457–468.

Putri, W.C.W.S., Muscatello, D.J., Stockwell, M.S., and Newall, A.T. (2018). Economic burden of seasonal influenza in the United States. *Vaccine* 36, 3960–3966.

Ramage, H.R., Kumar, G.R., Verschueren, E., Johnson, J.R., Von Dollen, J., Johnson, T., Newton, B., Shah, P., Horner, J., Krogan, N.J., et al. (2015). A combined proteomics/genomics approach links hepatitis C virus infection with nonsense-mediated mRNA decay. *Mol. Cell* 57, 329–340.

Resende, P.C., Bezerra, J.F., Teixeira Vasconcelos, R.H., Arantes, I., Appolinario, L., Mendonça, A.C., Paixao, A.C., Duarte, A.C., Silva, T., Rocha, A.S., et al. (2021). Severe Acute Respiratory Syndrome Coronavirus 2 P.2 Lineage Associated with Reinfection Case, Brazil, June-October 2020. *Emerg. Infect. Dis.* 27, 1789–1794.

Saha, B., and Parks, R.J. (2021). Identification of human adenovirus replication inhibitors from a library of small molecules targeting cellular epigenetic regulators. *Virology* 555, 102–110.

Schwarz, J.M., Cooper, D.N., Schuelke, M., and Seelow, D. (2014). MutationTaster2: mutation prediction for the deep-sequencing age. *Nat. Methods* 11, 361–362.

Shah, P.S., Link, N., Jang, G.M., Sharp, P.P., Zhu, T., Swaney, D.L., Johnson, J.R., Von Dollen, J., Ramage, H.R., Satkamp, L., et al. (2018). Comparative Flavivirus-Host Protein Interaction Mapping Reveals Mechanisms of Dengue and Zika Virus Pathogenesis. *Cell* 175, 1931–1945.e18.

Shannon, P., Markiel, A., Ozier, O., Baliga, N.S., Wang, J.T., Ramage, D., Amin, N., Schwikowski, B., and Ideker, T. (2003). Cytoscape: a software environment for integrated models of biomolecular interaction networks. *Genome Res.* 13, 2498–2504.

Shapira, S.D., Gat-Viks, I., Shum, B.O.V., Dricot, A., de Grace, M.M., Wu, L., Gupta, P.B., Hao, T., Silver, S.J., Root, D.E., et al. (2009). A physical and regulatory map of host-influenza interactions reveals pathways in H1N1 infection. *Cell* 139, 1255–1267.

Shin, Y.-K., Liu, Q., Tikoo, S.K., Babiuk, L.A., and Zhou, Y. (2007). Influenza A virus NS1 protein activates the phosphatidylinositol 3-kinase (PI3K)/Akt pathway by direct interaction with the p85 subunit of PI3K. *J. Gen. Virol.* 88, 13–18.

Simon, P.F., McCorrister, S., Hu, P., Chong, P., Silaghi, A., Westmacott, G., Coombs, K.M., and Kobasa, D. (2015). Highly Pathogenic H5N1 and Novel H7N9 Influenza A Viruses Induce More Profound Proteomic Host Responses than Seasonal and Pandemic H1N1 Strains. *J. Proteome Res.* 14, 4511–4523.

Söderholm, S., Kainov, D.E., Öhman, T., Denisova, O.V., Schepens, B., Kuleskiy, E., Imanishi, S.Y., Corthals, G., Hintsanen, P., Aittokallio, T., et al. (2016). Phosphoproteomics to Characterize Host Response During Influenza A Virus Infection of Human Macrophages. *Mol. Cell. Proteomics* 15, 3203–3219.

Suhre, K., McCarthy, M.I., and Schwenk, J.M. (2021). Genetics meets proteomics: perspectives for large population-based studies. *Nat. Rev. Genet.* 22, 19–37.

Surjit, M., Liu, B., Chow, V.T.K., and Lal, S.K. (2006). The nucleocapsid protein of severe acute respiratory syndrome-coronavirus inhibits the activity of cyclin-cyclin-dependent kinase complex and blocks S phase progression in mammalian cells. *J. Biol. Chem.* 281, 10669–10681.

Sussman, J., Stokoe, D., Ossina, N., and Shtivelman, E. (2001). Protein kinase B phosphorylates AHNAK and regulates its subcellular localization. *J. Cell Biol.* 154, 1019–1030.

Swaney, D.L., Ramms, D.J., Wang, Z., Park, J., Goto, Y., Soucheray, M., Bholra, N., Kim, K., Zheng, F., Zeng, Y., et al. (2021). A protein network map of head and neck cancer reveals PIK3CA mutant drug sensitivity. *Science* 374, eabf2911.

Takashita, E., Kawakami, C., Morita, H., Ogawa, R., Fujisaki, S., Shirakura, M., Miura, H., Nakamura, K., Kishida, N., Kuwahara, T., et al. (2019). Detection of influenza A(H3N2) viruses exhibiting reduced susceptibility to the novel cap-dependent endonuclease inhibitor baloxavir in Japan, December 2018. *Euro Surveill.* 24.

Taubenberger, J.K., and Kash, J.C. (2010). Influenza virus evolution, host adaptation, and pandemic formation. *Cell Host Microbe* 7, 440–451.

Taubenberger, J.K., and Morens, D.M. (2006). 1918 Influenza: the mother of all pandemics. *Emerg. Infect. Dis.* 12, 15–22.

Tegally, H., Wilkinson, E., Giovanetti, M., Iranzadeh, A., Fonseca, V., Giandhari, J., Doolabh, D., Pillay, S., San, E.J., Msomi, N., et al. (2021). Detection of a SARS-CoV-2 variant of concern in South Africa. *Nature* 592, 438–443.

Thorne, L.G., Bouhaddou, M., Reuschl, A.-K., Zuliani-Alvarez, L., Polacco, B., Pelin, A., Batra, J., Whelan, M.V.X., Ummadi, M., Rojic, A., et al. (2021). Evolution of enhanced innate immune evasion by the SARS-CoV-2 B.1.1.7 UK variant. *bioRxiv*.

Tiensin, T., Chaitaweesub, P., Songserm, T., Chaisingh, A., Hoonsuwan, W., Buranathai, C., Parakamawongsa, T., Premasathira, S., Amonsin, A., Gilbert, M., et al. (2005). Highly pathogenic avian influenza H5N1, Thailand, 2004. *Emerg. Infect. Dis.* 11, 1664–1672.

Tokars, J.I., Olsen, S.J., and Reed, C. (2018). Seasonal Incidence of Symptomatic Influenza in the United States. *Clin. Infect. Dis.* 66, 1511–1518.

Trevejo, J.M., Asmal, M., Vingerhoets, J., Polo, R., Robertson, S., Jiang, Y., Kieffer, T.L., and Leopold, L. (2018). Pimodivir treatment in adult volunteers experimentally inoculated with live

influenza virus: a Phase IIa, randomized, double-blind, placebo-controlled study. *Antivir. Ther.* **23**, 335–344.

Tripathi, S., Pohl, M.O., Zhou, Y., Rodriguez-Frandsen, A., Wang, G., Stein, D.A., Moulton, H.M., DeJesus, P., Che, J., Mulder, L.C.F., et al. (2015). Meta- and Orthogonal Integration of Influenza “OMICs” Data Defines a Role for UBR4 in Virus Budding. *Cell Host Microbe* **18**, 723–735.

Tsai, T.-H., Choi, M., Banfai, B., Liu, Y., MacLean, B.X., Dunkley, T., and Vitek, O. (2020). Selection of Features with Consistent Profiles Improves Relative Protein Quantification in Mass Spectrometry Experiments. *Mol. Cell. Proteomics* **19**, 944–959.

Türei, D., Valdeolivas, A., Gul, L., Palacio-Escat, N., Klein, M., Ivanova, O., Ölbei, M., Gábor, A., Theis, F., Módos, D., et al. (2021). Integrated intra- and intercellular signaling knowledge for multicellular omics analysis. *Mol. Syst. Biol.* **17**, e9923.

Varga, Z.T., Ramos, I., Hai, R., Schmolke, M., García-Sastre, A., Fernandez-Sesma, A., and Palese, P. (2011). The influenza virus protein PB1-F2 inhibits the induction of type I interferon at the level of the MAVS adaptor protein. *PLoS Pathog.* **7**, e1002067.

Vaser, R., Adusumalli, S., Leng, S.N., Sikic, M., and Ng, P.C. (2016). SIFT missense predictions for genomes. *Nat. Protoc.* **11**, 1–9.

Verschueren, E., Von Dollen, J., Cimermancic, P., Gulbahce, N., Sali, A., and Krogan, N.J. (2015). Scoring Large-Scale Affinity Purification Mass Spectrometry Datasets with MiST. *Curr. Protoc. Bioinformatics* **49**, 8.19.1–8.19.16.

Vidy, A., Maisonnasse, P., Da Costa, B., Delmas, B., Chevalier, C., and Le Goffic, R. (2016). The Influenza Virus Protein PB1-F2 Increases Viral Pathogenesis through Neutrophil Recruitment and NK Cells Inhibition. *PLoS One* **11**, e0165361.

Wang, T.T., and Palese, P. (2009). Unraveling the mystery of swine influenza virus. *Cell* **137**, 983–985.

Wang, K., Li, M., and Hakonarson, H. (2010). ANNOVAR: functional annotation of genetic variants from high-throughput sequencing data. *Nucleic Acids Res.* 38, e164.

Wang, L., Fu, B., Li, W., Patil, G., Liu, L., Dorf, M.E., and Li, S. (2017). Comparative influenza protein interactomes identify the role of plakophilin 2 in virus restriction. *Nat. Commun.* 8, 13876.

Wang, R., Zhu, Y., Zhao, J., Ren, C., Li, P., Chen, H., Jin, M., and Zhou, H. (2019). Autophagy Promotes Replication of Influenza A Virus In Vitro. *J. Virol.* 93.

Ward, S.E., Kim, H.S., Komurov, K., Mendiratta, S., Tsai, P.-L., Schmolke, M., Satterly, N., Manicassamy, B., Forst, C.V., Roth, M.G., et al. (2012). Host modulators of H1N1 cytopathogenicity. *PLoS One* 7, e39284.

Watanabe, T., Kawakami, E., Shoemaker, J.E., Lopes, T.J.S., Matsuoka, Y., Tomita, Y., Kozuka-Hata, H., Gorai, T., Kuwahara, T., Takeda, E., et al. (2014). Influenza virus-host interactome screen as a platform for antiviral drug development. *Cell Host Microbe* 16, 795–805.

Webb, L.G., and Fernandez-Sesma, A. (2022). RNA viruses and the cGAS-STING pathway: reframing our understanding of innate immune sensing. *Curr. Opin. Virol.* 53, 101206.

Webster, R.G., Guan, Y., Poon, L., Krauss, S., Webby, R., Govorkov, E., and Peiris, M. (2005). The spread of the H5N1 bird flu epidemic in Asia in 2004. *Arch. Virol. Suppl.* 117–129.

Wise, H.M., Foeglein, A., Sun, J., Dalton, R.M., Patel, S., Howard, W., Anderson, E.C., Barclay, W.S., and Digard, P. (2009). A complicated message: Identification of a novel PB1-related protein translated from influenza A virus segment 2 mRNA. *J. Virol.* 83, 8021–8031.

Xu, J., Christman, M.C., Donis, R.O., and Lu, G. (2011). Evolutionary dynamics of influenza A nucleoprotein (NP) lineages revealed by large-scale sequence analyses. *Infect. Genet. Evol.* 11, 2125–2132.

Yeganeh, B., Ghavami, S., Kroeker, A.L., Mahood, T.H., Stelmack, G.L., Klonisch, T., Coombs, K.M., and Halayko, A.J. (2015). Suppression of influenza A virus replication in human lung

epithelial cells by noncytotoxic concentrations bafilomycin A1. *Am. J. Physiol. Lung Cell. Mol. Physiol.* 308, L270–L286.

Yue, H., Zhang, M., Xing, L., Wang, K., Rao, X., Liu, H., Tian, J., Zhou, P., Deng, Y., and Shang, J. (2020). The epidemiology and clinical characteristics of co-infection of SARS-CoV-2 and influenza viruses in patients during COVID-19 outbreak. *J. Med. Virol.* 92, 2870–2873.

Zhang, Q., Bastard, P., Liu, Z., Le Pen, J., Moncada-Velez, M., Chen, J., Ogishi, M., Sabli, I.K.D., Hodeib, S., Korol, C., et al. (2020). Inborn errors of type I IFN immunity in patients with life-threatening COVID-19. *Science* 370.

Zhang, S.-Y., Jouanguy, E., Ugolini, S., Smahi, A., Elain, G., Romero, P., Segal, D., Sancho-Shimizu, V., Lorenzo, L., Puel, A., et al. (2007). TLR3 deficiency in patients with herpes simplex encephalitis. *Science* 317, 1522–1527.

Zumla, A., Rao, M., Wallis, R.S., Kaufmann, S.H.E., Rustomjee, R., Mwaba, P., Vilaplana, C., Yeboah-Manu, D., Chakaya, J., Ippolito, G., et al. (2016). Host-directed therapies for infectious diseases: current status, recent progress, and future prospects. *Lancet Infect. Dis.* 16, e47–e63.

Publishing Agreement

It is the policy of the University to encourage open access and broad distribution of all theses, dissertations, and manuscripts. The Graduate Division will facilitate the distribution of UCSF theses, dissertations, and manuscripts to the UCSF Library for open access and distribution. UCSF will make such theses, dissertations, and manuscripts accessible to the public and will take reasonable steps to preserve these works in perpetuity.

I hereby grant the non-exclusive, perpetual right to The Regents of the University of California to reproduce, publicly display, distribute, preserve, and publish copies of my thesis, dissertation, or manuscript in any form or media, now existing or later derived, including access online for teaching, research, and public service purposes.

DocuSigned by:

Kelsey Haas

771F6C68A143490...

Author Signature

3/14/2022

Date